Hybrid Molecular and Continuum Fluid Dynamics Models for Micro and Nanofluidic Flows

Nikolaos Asproulis

Submitted for the Degree of Ph.D.

Department of Aerospace Sciences
Cranfield University
Cranfield, UK

2009

Cranfield University

School of Engineering

PhD

Nikolaos Asproulis

Hybrid Molecular and Continuum Fluid Dynamics Models for Micro and Nanofluidic Flows

Supervisor: Prof. Dimitris Drikakis

December, 2009

Abstract

From molecules to living organisms and from atoms to planets a variety of physical phenomena operate at different temporal and spatial scales. Understanding the nature of those phenomena is crucial for advancing new technologies in many disciplines. In micro and nanofluidics as the operational dimensions are downsized to smaller scales the surface-to-volume ratio increases and the surface phenomena become dominant. Numerical modelling is the key for obtaining a better insight into the processes involved. The Achilles heel of fine grain microscopic numerical simulations is their computational cost. Simulating a multiscale phenomenon with an accurate microscopic description is extremely demanding computationally. On the contrary, simulations of multiscale phenomena based only on macroscopic descriptions cannot fully capture the physics of the multiscale systems. In order to confront this dilemma multiscale frameworks, called hybrid codes, have been developed to couple the microscopic and macroscopic description of a system and to facilitate the exchange of information.

The aim of this research project is to establish and implement a robust hybrid molecular-continuum method for micro- and nano-scale fluid flows. Towards that direction a hybrid multiscale method named as Point Wise Coupling (PWC) has been developed. PWC aims to circumvent the limitations of the existing hybrid continuum/atomistic approaches and deliver a modular and applicable methodology. In the PWC, the whole domain is covered with the macroscopic solver and the microscale model enters as a local refinement. Additionally, numerical techniques based on neural networks are employed to minimise the cost of the molecular solver and reduce the outcomes' variability induced by the fluctuating nature of the atomistic data.

Molecular studies have been performed (i) to obtain a better insight of the interfacial phenomena in the solid/liquid interfaces, and (ii) to study the parametrisation of the molecular models and mapping of atomistic information to hybrid frameworks. Specifically, the impact of parameters, such as surface roughness and stiffness, to slip process is studied.

PWC framework has been employed to study a number of fundamental test cases including Poiseuille flow of polymeric fluids, isothermal slip Couette flow and slip Couette flow with heat transfer. Attention is drawn to the boundary condition transfer from the continuum solver to the atomistic description. In the performed hybrid studies the effects of the numerical optimisation techniques (linear interpolation, neural networks) to simulations' accuracy, stability and efficiency are studied. The outcomes of the simulations suggest that the neural networks scheme enhance the simulation's efficiency by minimising the number of atomistic simulations and at the same time act as a smoothing operator for reducing the oscillations' strength of the atomistic outputs.

Acknowledgements

I would like to take this opportunity to thank and express my sincere gratitude to my supervisor Professor Dimitris Drikakis for giving me the opportunity to do a research degree in a project where I feel very lucky to be a part of, and for his expert guidance and support.

I would also like to extend my gratitude to Dr. Kalweit and Dr. Shapiro for their technical advice and intellectual stimuli during the last three year of this research project.

I am grateful to all the members of FMaCS group, especially to Christos Vamvakoulas, Nicholas Epiphaniou, Kostas Karantonis and Yiannis Kokkinakis. Many thanks to my housemates over the last years Takis Tsoutsanis, Elias Tsoutsanis and Antony Mylonas for their invaluable friendship and help.

Special thanks to my parents Giorgos and Kalliopi, my brothers Christos and Anna, and my girlfriend Christina for their love and encouragement.

Στους γονείς μου Γιώργο και Καλλιόπη

για τη συνεχή και αταλάντευτη στήριξη τους

Contents

List of Figures

List of Tables

Nomenclature

Symbols

$\boldsymbol{F}^{ext}$	External force
$\boldsymbol{u}_{con}$	Continuum velocity
$\boldsymbol{u}$	Fluid velocity
$\mathcal{A}$	Physical substance
χ	Thermal diffusivity
Δt_{AV}	Hybrid information exchange interval
Δt_C	Continuum time step
Δt_{MD}	Molecular time step
η	Gaussian distributed random force
$\hbar$	Planck constant
κ	Spring stiffness
Λ	Thermal DeBroglie wavelength
λ	Mean free path
$\mathbf{\Pi}$	Tensor of surface forces
$\mathbf{n}$	Normal to a surface vector
ν	Kinematic viscosity
$\phi(\mathcal{A}, \tau_c)$	Autocorrelation function
ρ	Fluid density
ρ_w	Wall density
$\sigma(\langle\mathcal{A}\rangle_t)$	Standard deviation
σ_u	Tangential momentum accommodation coefficient
τ_c	Time lag

e	Internal energy
$f(\boldsymbol{C})$	Probability distribution function
k	Thermal conductivity
k_B	Boltzmann constant
Kn	Knudsen number
L_s	Slip length
l_s	Dimensionless slip length
M	Total particle mass in the overlapping region
m_i	Particle's mass
Ma	Mach number
N_B	Number of particles in the overlapping region
p	Pressure
P_{con}	Continuum pressure
q	Heat flux
Re	Reynolds number
S	Surface area
T	Temperature
T_{con}	Continuum temperature
u_{slip}	Slip velocity
V	Control volume
V_i	Potential of a single particle

Acronyms

ANN	Artificial Neural Network
BCT	Boundary Conditions Transfer
CFD	Computational Fluid Dynamics
CPU	Central Processing Unit
DSMC	Direct Simulation Monte Carlo

FCC	Face Centred Cubic
FD	Finite Difference
FMaCS	Fluid Mechanics and Computational Science
FV	Finite Volume
GA	Genetic Algorithm
HSI	Hybrid Solution Interface
LAMMPS	Large-scale Atomic/Molecular Massively Parallel Simulator
LEBC	Lees-Edwards Boundary Conditions
LJ	Lennard-Jones
MD	Molecular Dynamics
MEMS	Micro Electrical Mechanical Systems
NEMS	Nano Electrical Mechanical Systems
NN	Neural Networks
PBC	Periodic Boundary Conditions
PWC	Point Wise Coupling
RMSD	Root Mean Square Differnce
RMS	Root Mean Square
RNEMD	Reverse Non Equilibrium Molecular Dynamics
TMAC	Tangential Momentum Accommodation Coefficient

CHAPTER 1

Introduction

1.1 Micro and Nano flows

The study of fluids in channels with dimensions in the micro- and nano-scale range, known as micro and nanofluidics, have emerged as an effective and promising new field over the last decade [1]. Devices developed at these scales have been utilised for various applications including bioengineering and chemistry [2–5]. The study of flows in micro and nanoscales is anticipated in the near future to have great impact in the design of high through-put devices [2, 3].

Due to the small scales involved and the high surface-to-volume ratio, the phenomena observed inside micro and nanoscale devices present unique characteristics and major differences compared to large scale ones. Thence, the understanding of the phenomena in micro and nanoscale flows, as well as efficient and realistic modelling of those, is of paramount importance for optimal designs of devices operating at these scales [6]. Numerical experiments can be directly utilised to guide functionality-oriented designs and therefore optimise the overall design process [1, 7, 8]. The flow in a variety of micromechanical (MEMS) systems, like combustors, valves, nozzles, turbomachines, etc, cannot be fully predicted by continuum flow models, like the Navier-Stokes equations with no-slip boundary conditions at the solid-liquid interface [6]. As the dimensions of one system shrink to smaller scales, the assumptions of the continuum approximations break down and highly sophisticated numerical approaches have to be adopted.

1.2 Modelling Approaches

From molecules to living organisms and from atoms to planets a variety of physical phenomena operate at different temporal and spatial scales. Understanding the nature of these

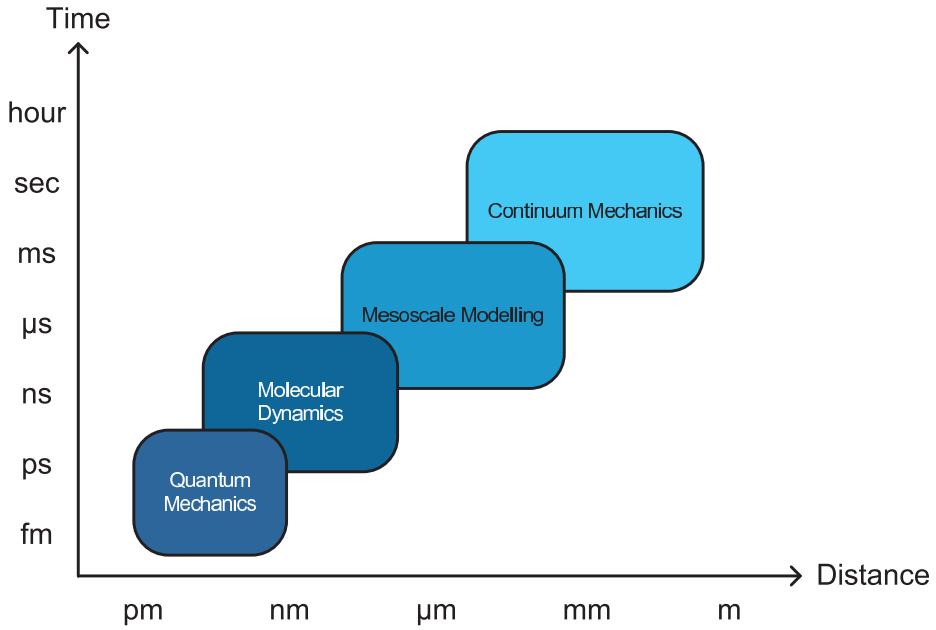

Figure 1.1: Modelling approaches at various spatial and temporal scales

phenomena is crucial for advancing new technologies in many disciplines. Even from the ancient years several theories, to explain the initiative processes of the multiscale phenomena, existed. In ancient Greek philosophy there were two opposite views about the nature of these phenomena, the discrete, and the continuum. Aristotle was the representative of the continuous theory and Democritus of the atomistic one. In modern physics both views have been reconciled by considering the continuum approach as average of discrete quantities as atoms or molecules.

It is possible to identify two main modelling strategies for transport processes inside micro and nanofluidic devices. The first one is the *continuum level modelling* based on equations of continuum mechanics and the second one is the *molecular level modelling* based on the equations of motion for individual particles (see Figure 1.1). The two approaches are separated in length and time scales and the choice of the most suitable one depends on the flow characteristics and the level of detail required [8, 9].

While both the continuum and molecular level modelling is understood quite well, a significant modelling challenge is associated with physical phenomena, such as dynamic melting or strong shear localisation [10], which cannot be entirely addressed within the scope of either continuum or molecular approach. In the biomedical area, additional challenges are associated with applications involving complex macromolecules. The similarity in dimensions between micro and nanofluidic devices and biomolecules, such as DNA or RNA, opens new perspectives in disciplines such as genomics or proteomics [3]. However the transport of complex macromolecules with low number densities [11, 12] occur in a transitional regime which cannot be addressed with either the continuum or the molecular description. In this case the continuum description fails due to the small scales involved

while purely molecular description cannot be applied due to the excessive computational requirements associated with the complexity of the molecules in question.

To circumvent these issues a number of hybrid *multiscale modelling* approaches has been developed [13–15]. These approaches allow selective or blended application of both molecular and continuum descriptions simultaneously [9, 13]. These methods include, in general, continuous two-way exchange of information between continuum level and molecular level models.

1.3 Hybrid atomistic/continuum methods

Modelling micro and nanofluidic devices presents significant difficulties due to the inaccuracy of the continuum models and inefficiency of the molecular ones. In order to address this challenge multiscale hybrid frameworks have been developed to couple the microscopic and macroscopic descriptions of a system and facilitate the exchange of information. Hybrid methods aim to bridge the gap between the macroscopic and microscopic length scales and provide a unifying description of fluid flows from nanoscale to larger scales.

Multiscale modelling techniques can be broadly classified into the following groups:

- Geometrical Coupling [13, 14, 16–24]
- Embedded Coupling [10, 25–31]

Geometrical coupling is a spatial multiscale approach. It exploits the fact that the continuum equations are valid in large regions of the system, but fail to fully describe the phenomena in a particular area. The domain can then be decomposed into two distinct regions, with one region described by a continuum model and another, by a molecular model. The main challenge is associated with the development of algorithms aiming to facilitate the information exchange between the molecular and continuum regions [9, 13, 16]. The solution in each domain is computed independently by the corresponding method and each method will provide an appropriate boundary condition for the other through a hybrid solution interface (HSI). The role of the HSI is to establish and maintain the communication between the two regions and to unify the domains into one single physical space. The advantage of geometrical coupling is that the computationally expensive molecular model is applied within a small region of the overall computational domain, whereas the majority of the domain is treated by a continuum solver, which is several orders of magnitude faster.

The embedded methods present an alternative approach to spatial and temporal decoupling [32]. In the embedded schemes the whole domain is resolved with the macroscopic solver and the microscopic model enters as a refinement to obtain macroscopic properties.

The continuum solver advances the solution in the entire domain and the molecular simulations are used to provide data required by the continuum solver. The development of embedded schemes has been motivated by the time scale barriers that are introduced in the geometrical coupling.

1.4 Aim and Objectives

The aim of this research project is to establish and implement a robust hybrid molecular-continuum method for micro- and nano-scale fluid flows. The main objectives are:

- Provide an overview of the existing hybrid frameworks and acknowledge their limitations
- Develop a hybrid molecular/continuum framework to overcome the deficiencies of the existing schemes
  - Develop a framework to circumvent the time scale constraints
  - Develop a numerical optimisation procedure to further reduce the cost of the molecular solver
  - Verify the new framework in standard flow problems and assess its performance in terms of stability, accuracy, physical consistency and efficiency
- Enhance our physical understanding regarding solid-fluid interactions
  - Study transfer phenomena in solid-liquid interfaces through molecular and hybrid numerical modelling

1.5 Publications

During the period of the PhD project a book chapter and several journal and conference papers have been written.At this point it has to be mentioned that this work has been supported in part by the European Commission under the 6th Framework Program (Project: DINAMICS, NMP4-CT-2007-026804), which is greatly acknowledge.

- Book chapters
  - D. Drikakis, N. Asproulis, E. Shapiro and M. Benke, *Computational Strategies for Micro and Nanofluid Dynamics*, Book on "Microfluidic Devices in Nanotechnology: Current Status and a Future Perspective" (Ed. C. Kumar), John Wiley, 2009.

- Journal papers
  - N. Asproulis and D. Drikakis, *Materials Modelling using Neural Networks*, Journal of Computational and Theoretical Nanoscience 6(3), 514-518, 2009.
  - N. Asproulis, M. Kalweit, E. Shapiro and D. Drikakis, *Mesoscale flow and heat transfer modelling and its application to liquid and gas flows*, Journal of Nanophotonics 1(3),031960-031975, 2009.
  - N. Asproulis and D. Drikakis, *Surface roughness effects in micro and nanofluidic devices*, Journal of Computational and Theoretical Nanoscience, 2009 (in print).
  - D. Drikakis and N. Asproulis, *Multiscale Computational Modelling of Flow and Heat Transfer*, International Journal for Numerical Methods for Heat and Fluid Flow, 2009 (in print).
- Conference papers
  - N. Asproulis, E. Shapiro , M. Kalweit and D. Drikakis, *Multiscale modelling for flows and materials*, in Cranfield Multi-Strand Conference, Cranfield, 2008.
  - N. Asproulis, M. Kalweit and D. Drikakis, *A hybrid molecular continuum method using point wise coupling*, in Sixth International Conference on Engineering Computational Technology, (Eds. B. Topping and M. Papadrakakis), Civil-Comp Press, Athens, September 2008.
  - M. Kalweit, N. Asproulis, and D. Drikakis, *Nanofluidic applications of hybrid molecular-continuum methods*, in 1st International Nanotechnology Conference, Albany, New York, September 2008.
  - N. Asproulis, M. Benke, M. Lai, E. Shapiro, D. Drikakis, et al. *Modelling approaches for micro- and nanoscale diffusion phenomena*, in 1st International Nanotechnology Conference, Albany, New York, September 2008.
  - N. Asproulis, M. Kalweit, E. Shapiro and D. Drikakis, *Mesoscale flow and heat transfer modelling and application to liquid and gas flows*, in Nanoscience and Nanotechnology Conference, Rome, October 2008.
  - N. Asproulis, M. Kalweit and D. Drikakis, *Hybrid molecular-continuum methods for micro- and nanoscale liquid flows*, submitted to 2nd Micro and Nano Flows Conference, Uxbridge, UK, September 2009.
  - N. Asproulis and D. Drikakis, *Thermal interaction effects in micro and nanofluid flows*, in 1^{st} International Conference on Computational Methods for Thermal Problems, Naples, September 2009.
  - D. Drikakis and N. Asproulis, *Multiscale Computational Modelling of Flow and Heat Transfer*, in 1^{st} International Conference on Computational Methods for Thermal Problems, Naples, September 2009.

1.6 Thesis Overview

Chapter 2 provides a description of the continuum level modelling along with the underlying equations and family of methods. It is followed by a description of molecular dynamics and its main interaction potentials and boundary conditions. Furthermore, this chapter includes a review of the current status of the hybrid molecular-continuum frameworks and it concludes with a description of neural networks and genetic algorithms.

Chapter 3 describes the developed multiscale framework named as Point Wise Coupling (PWC). The basic idea of the PWC is to perform MD simulations on the fly to estimate parameters needed for the continuum solver. PWC can be employed to study problems were the boundary conditions and/or constitutive relations are not explicitly known. A numerical optimisation procedure that has been developed to minimise the cost of the atomistic solver is also presented. Two different implementations of the optimisation procedure are discussed (i) the Linear optimisation and (ii) the Neural Netowrk optimisation.

Chapter 4 includes the molecular studies performed to obtained a better insight of (i) the interfacial phenomena in the solid/liquid interfaces, (ii) the applicability of techniques like Neural Networks in the context of molecular dynamics and (iii) the parametrisation of molecular models and mapping of atomistic information in the hybrid frameworks.

Chapter 5 includes the performed hybrid studies. The first test case studies the application of the various techniques for the transfer of boundary conditions from the continuum description to the atomistic model. The next cases include coupled simulations aiming to study the applicability and efficiency of PWC along the developed numerical procedures.

Chapter 6 presents the conclusions drawn from this research project and possible future research directions

CHAPTER 2

Modelling at multiple scales

2.1 Introduction

The first section of this chapter introduces the continuum level modelling which is based in the numerical solution of the Navier-Stoke equations. The underlying equation of motion and the basic family of methods applied are described. In the next section a description of the molecular models and particularly of molecular dynamics (MD) is provided. The main interaction potential, boundary conditions and integration algorithms are presented. After the description of the atomistic models a detailed review of the current status-of-the-art regarding the hybrid molecular-continuum frameworks is given. The two main approaches (i) geometrical coupling and (ii) embedded coupling are discussed. The chapter concludes with a description of the numerical tools, neural networks and genetic algorithms, that have been employed in the context of the current study.

2.2 Continuum modelling

Continuum level modelling has been historically the dominant approach in fluid flow studies. Continuum level modelling has been successfully applied to an overwhelming number of engineering problems including problems related to micro flows (e.g. [33, 34]). The main component of continuum level fluid flow modelling is the numerical solution of the Navier-Stokes equations, however additional sets of equations may be required in order to address various phenomena in microfluidics. For example Navier-Stokes can be coupled with heat transfer or Poisson-Boltzmann equations to study thermal transport and electrokinetic flows respectively [8, 11]. However, as the dimensions of a system become smaller, the continuity assumption breaks down and the continuum models fail to fully capture the physics of the fluid flow [35, 36].

The scope of the current section is to provide an introduction to the continuum level modelling. The main aim is to assist the following description of the multiscale models, rather than to present a detailed review of the continuum level numerical tools and methods. Further information about continuum level modelling can be found in a number of reviews and books published over the last decade, for example [37–41].

Governing Equations

The Navier-Stokes equations governing the fluid flow from the continuum perspective comprise conservation laws for mass, momentum and energy. The conservation of mass for each component/specie of the flow is expressed through the continuity equation, which can be written for a control volume V with the surface S characterised by the normal vector $\mathbf{n}$ as

$$\frac{\partial}{\partial t}\int\int\int_V \rho dV = -\int\int_S \rho\left(\boldsymbol{u}\cdot\boldsymbol{n}\right)dS + R_m, \tag{2.2.1}$$

$\boldsymbol{u}$ where ρ and $\boldsymbol{u}$ denote the density and the velocity of the fluid respectively. The first term on the right hand side represents the flux of mass through the surface of the control volume and R_m is the source term corresponding to production/destruction of mass. While in a single component flow the source term is zero, it can be used to describe the mass production due to chemical reactions and phase transfer in multispecies and multiphase flows (see, for example, [42, 43]). The conservation law for the momentum relates the change of the momentum to the total force acting on the control volume

$$\frac{\partial}{\partial t}\int\int\int_V \rho\boldsymbol{u}dV = -\int\int_S \rho\boldsymbol{u}\left(\boldsymbol{u}\cdot\boldsymbol{n}\right)dS + \int\int\int_V \boldsymbol{F}_V dV + \int\int \boldsymbol{\Pi} d\mathbf{S}, \tag{2.2.2}$$

where the first term on the right hand side represents the flux of momentum through the control surface S, $\boldsymbol{F}_V$ is the vector of volume forces and $\boldsymbol{\Pi}$ is the tensor of surface forces. In the absence of external surface forces, $\boldsymbol{\Pi}$ can be decomposed into the normal force - pressure p, which can be either thermodynamic or mechanical, depending on the approximation, and the viscous stresses represented by a symmetric tensor $\tau = \left\{\tau_{ij}\right\}$, $\tau_{ij} = \tau_{ji}$. This decomposition leads to the total stress tensor of the form $\boldsymbol{\Pi} = -p\mathbf{I} + \tau$, where $\mathbf{I}$ is the identity tensor. Finally the last equation describes the conservation of total energy

$$\begin{aligned}\frac{\partial}{\partial t}\int\int\int_V \rho E dV \;=\; &-\int\int_S \rho E\left(\boldsymbol{u}\cdot\boldsymbol{n}\right)dS - \int\int_S \left(\boldsymbol{q}\cdot\boldsymbol{n}\right)dS + \\ &\int\int\int_V \left(\boldsymbol{u}\cdot\boldsymbol{F}_V\right)dV + \int\int_S \boldsymbol{\Pi}\boldsymbol{u}d\mathbf{S},\end{aligned} \tag{2.2.3}$$

relating the change of energy in the control volume to the convective flux through the surface, heat flux $\boldsymbol{q}$ through the surface, the work of volume forces and the work of surface forces.

The system of Equations (2.2.1)-(2.2.3) represents fundamental conservation laws which

should be obeyed by any continuum fluid system. Note that the notion of the system being at the continuum level has been implicitly introduced through the definition of macroscopic flow variables, such as density. However the system is not closed with respect to the number of variables. The closure is obtained through additional assumptions regarding the nature of the fluid.

The closure for the heat flux can be obtained by using Fourier's law linking the heat flux to temperature T

$$\boldsymbol{q} = -k\nabla T \tag{2.2.4}$$

where k is the thermal conductivity. The stresses for an isotropic Newtonian fluid can be expressed through the velocity and dynamic viscosity as follows:

$$\tau_{xx} = -\frac{2}{3}\mu\nabla\cdot\boldsymbol{u} + 2\mu\frac{\partial u}{\partial x} \tag{2.2.5}$$

$$\tau_{yy} = -\frac{2}{3}\mu\nabla\cdot\boldsymbol{u} + 2\mu\frac{\partial u}{\partial y} \tag{2.2.6}$$

$$\tau_{zz} = -\frac{2}{3}\mu\nabla\cdot\boldsymbol{u} + 2\mu\frac{\partial u}{\partial z} \tag{2.2.7}$$

$$\tau_{xy} = \tau_{yx} = \mu\left(\frac{\partial v}{\partial x} + \frac{\partial u}{\partial y}\right) \tag{2.2.8}$$

$$\tau_{xz} = \tau_{zx} = \mu\left(\frac{\partial u}{\partial z} + \frac{\partial w}{\partial x}\right) \tag{2.2.9}$$

$$\tau_{yz} = \tau_{zy} = \mu\left(\frac{\partial w}{\partial y} + \frac{\partial v}{\partial z}\right) \tag{2.2.10}$$

Other forms of stress tensor can be more appropriate for liquids such as blood, paints, emulsions, etc, which do not follow Newton's hypothesis of stress being proportional to the rate of strain (e.g. [44]).

Finally pressure, density, temperature and internal energy are linked by caloric and thermal equations of state which depend on the physical properties of the fluid. The total energy is then split into internal and kinetic components:

$$E = e + \frac{\boldsymbol{u}\cdot\boldsymbol{u}}{2}, \tag{2.2.11}$$

with the internal energy expressed for gases through the variables of state as follows:

$$e = \frac{p}{\rho\,(\gamma - 1)} = c_v \cdot T, \tag{2.2.12}$$

where γ is the adiabatic index equal to ratio of specific heat capacity at constant pressure c_p to specific heat capacity at constant volume c_v. The system is closed by the thermal

equation of state, for example, the ideal gas equation of state

$$p = \rho RT, \tag{2.2.13}$$

where R is the gas constant.

The closed system of continuum level equations can be applied to micro and nanoscale fluid systems, up to a certain dimension. In general, under normal conditions, liquid flows can be addressed up to $\sim 10nm$ scale and gas flows - up to $\sim 100nm$ scale (e.g. [39, 45]). Continuum level modelling has been applied successfully at microscale in numerous problems, such as multiphase heat exchangers [46], microbubble generation for biomedical applications [47] and electrokinetic micromixers [48, 49].

At the Boundaries of Continuum

The degree of importance of non-continuum effects, or rarefaction, can be expressed through the Knudsen number

$$Kn = \frac{\lambda}{L} \tag{2.2.14}$$

relating the mean free path λ to the characteristic size of the system of interest L.

Non-continuum effects become more important with the increase of Knudsen number. Note that for air at atmospheric conditions $\lambda \sim 65nm$, which will lead to $Kn \sim 1$ for nanoscale devices. The system of Navier-Stokes equations as formulated above is of the 1st order in Knudsen number. Several corrections extending applicability of the continuum level modelling to higher Knudsen numbers have been developed in the past including quasi hydro-dynamics, quasi gas dynamics, Burnett and super-Burnett systems (e.g. [45, 50, 51]).

Apart from the form of the governing equations, boundary conditions in micro and nanofluidic systems exhibit dependence on the Knudsen number. For example the no-slip condition for velocity at a solid stationary wall becomes inappropriate when Kn>0.001 (see, for example, [39] for more details). In general, continuum models applicability can be summarised as follows:

- For $Kn \leq 10^{-3}$ the flow is considered to be in continuum regime and Navier-Stokes equations with no slip boundary conditions can be employed.
- For $10^{-3} < Kn \leq 0.1$ - slip flow and the fluid models employed are either Navier-Stokes equations or Burnett equations with first order slip boundary conditions.
- For $10^{-1} < Kn \leq 1$ - it is possible to extend the applicability of Navier-Stokes and Burnett equations using higher order slip conditions, quasi hydrodynamic and quasi gas dynamic description.

- For $Kn > 1$ - continuum approach becomes invalid.

Significant number of applications in micro and nanofluidics deal with liquids or gases at speeds which are much smaller than the speed of sound a in the media. When the Mach number $M = \frac{U}{a}$, where U is the characteristic flow velocity, is sufficiently small - the governing system of equations can be simplified using the incompressibility assumption. For a single specie flow, this leads to density becoming constant. Then the mass conservation Equation (2.2.1) reduces to:

$$\nabla \cdot \boldsymbol{u} = 0. \tag{2.2.15}$$

The momentum equation becomes

$$\frac{\partial \boldsymbol{u}}{\partial t} + \boldsymbol{u}\nabla\boldsymbol{u} = -\frac{1}{\rho}\nabla p + \nu\nabla^2\boldsymbol{u}, \tag{2.2.16}$$

where ν is the kinematic viscosity. The energy equation for incompressible flows usually reduces to an advection-diffusion equation for the temperature field. If we neglect viscous dissipation this leads to

$$\frac{\partial T}{\partial t} + \boldsymbol{u}\nabla T = \nabla\left(\chi\nabla T\right), \tag{2.2.17}$$

where χ denotes thermal diffusivity. The temperature field is then decoupled from the velocity field.

The relative importance of viscous effects is determined by the Reynolds number - $Re = \frac{\rho UL}{\mu}$, where L denotes the characteristic length of the device (for example hydraulic diameter of the microchannel). Typical applications in micro and nanofluidics, for example lab-on-a-chip and bioanalysis systems, deal with relatively low speed liquid flows which correspond to relatively low Reynolds numbers $\left(10^{-5} - 100\right)$. For Reynolds numbers smaller than 10^{-1}, convection effects become negligible and the governing model can be further simplified. The resulting Stokes flow is described by the following momentum equation:

$$\frac{\partial \boldsymbol{u}}{\partial t} = -\frac{1}{\rho}\nabla p + \nu\nabla^2\boldsymbol{u} \tag{2.2.18}$$

The above equation is linear which significantly simplifies the numerical solution.

It should be mentioned that Knudsen number is linked to Mach and Reynolds numbers by

$$Kn = C\frac{Ma}{Re}, \tag{2.2.19}$$

where the constant C depends on the properties of gas and is typically of order 1 (see, for example, [45] for more details).

Numerical Approaches

Most micro and nanofluidic applications feature either liquids as main media or low Mach numbers in gas flows, which prompts the selection of the incompressible model. The simplification introduced by flow incompressibility leads to the main numerical challenge in modelling fluid flows at low speeds and small scales. Pressure becomes mechanical and is no longer linked to the rest of the flow properties by an equation of state. Instead the correct pressure field is determined by the incompressibility constraint (2.2.15). Given the pressure field we can solve the momentum equation (2.2.18), however the resulting velocity field does not necessarily obey the incompressibility constraint. When the correct pressure is found, the incompressibility constraint is satisfied by the resulting velocity field.

This link between the pressure field and the velocity field prompted the development of the pressure-correction family of methods based on iterative procedure where guessed value of pressure is used to calculate the velocity field, and then the Poisson equation for pressure is constructed to obtain a correction for pressure. The procedure is repeated until the compressibility constraint is satisfied (see, for example, [52]). Pressure correction methods enjoy wide popularity within both academic community and commercial modelling package developers.

Pressure-projection family of methods is frequently used to couple the pressure and momentum fields in both constant and variable density problems (e.g. [37]). The key idea of the projection method is to advance the velocity field in time somehow, disregarding the solenoidal nature of the velocity field and then recover the desired solenoidal velocity vector. The procedure leads to a Poisson equation for pressure which is the most computationally demanding part of the algorithm. Bell and Marcus [53], and later Almgren *et al.* [54, 55], have developed second-order projection algorithms for variable-density incompressible flows. An extensive discussion of robust fractional-step projection methods for variable density flows can be found in [56]. A recent review of approximate and exact projection methods can also be found in [37]. Pressure-projection based methods have also been used in conjunction with finite-element schemes, see e.g. [57] and [58]; in the latter an unconditionally stable method was developed based on two projections per time step and its performance was investigated both in finite volume and finite-element implementations.

Another family of methods applicable to low-speed flows in micro and nanofluidics stems from the work of Chorin [59] who developed an approach based on artificial compressibility formulation. In this approach pseudo-time derivatives are added to the continuity equation and, for unsteady flows, momentum equations to link numerically pressure and velocity fields. The new system of equations can then be iterated in pseudo-time until the steady state corresponding to the divergence-free flow is found. During this transient process, the system behaves essentially as a compressible system with an artificial speed of sound chosen to speed up the convergence process [60]. The method can be used in conjunction with a number of implicit and explicit numerical schemes. A review of numerical schemes for artificial compressibility formulation can be found in [37]. The artificial

compressibility method leads to hyperbolic and hyperbolic-parabolic equations for inviscid and viscous incompressible flows, respectively. The numerical schemes developed for the artificial compressibility formulation are largely similar to methods developed for compressible flows. Therefore, numerical developments for compressible flows can be directly transferred to incompressible flows [37] which allows the application of higher-order high resolution schemes in the context of constant and variable density flows [37, 61, 62]. Examples of application of the artificial compressibility schemes to microfluidic problems include DNA transport simulations [63]. The high-resolution methods applied in the context of the artificial compressibility approach have been shown to provide better capturing of discontinuities in multi-component microfluidic flows (e.g. [64]).

The continuum level solution for flow in micro and nanofluidic devices can be obtained using in-house or open-source codes (e.g. OpenFOAM) based on methods listed above. Whenever feasible, this approach provides great advantages, out of which extensibility is probably the most important one. With the access to the code, models for additional complex phenomena can be easily incorporated and coupling of continuum flow solution with molecular or meta-models can be implemented. Alternatively a number of commercial packages can be used for continuum level modelling. These can be broadly classified into:

- General-purpose modelling and CFD packages, such as Ansys FLUENT or CFX, STAR-CD, CFD-ACE+ (see, for example, [41]), etc. These can provide some of the capabilities specific to micro and nano-flow applications. For example, slip boundary conditions available in FLUENT and additional MEMS (Micro-Electro-Mechanical Systems) package in CFD-ACE+.
- Multi-physics packages, for example COMSOL Multiphysics (FEMLAB) with dedicated modules for microfluidics and MEMS
- MEMS-specific modelling software, such as, for example Coventor and IntelliSuite.

Despite the wealth of methods and packages capable of dealing with the continuum level modelling at low and, to a degree, medium Knudsen numbers, there are no readily available packages for problems involving transitional Knudsen numbers and coupled molecular-continuum scales.

2.3 Molecular modelling

Classical molecular models have been applied to study an overwhelming number of problems related to flows at the micro and especially nano scales. For example, MD simulations have been carried out to obtain both qualitative and quantitative characterisation of surface roughness phenomena inside nanofluidic devices [65–69]. A number of parameters that

affect the fluid behaviour, and consequently the performance of nanofluidics, can be determined using MD such as, the wall-fluid interactions and the wetting properties of the surface [70, 71]. Classical molecular modelling is also widely applied in bio-flows [72–76]. In a recent study [73] molecular simulations were employed to exploit the effects of shock waves on biological tissues and the numerical studies revealed that the shock wave leads to an increased diffusion coefficient and therefore makes the membrane transiently more permeable, which can assist drug delivery. Other application areas include nanosensors [33, 77], nanofilters and nanovalves [78, 79], nanoparticle collisions and flows [80] and lubrication [81–86].

Although MD is a very poweful tool it experiences limitations primarily related with the computational time and computing power required, especially for fine grain simulations. Specifically, the major shortcoming of MD are:

- Quantum effects: MD experiences limitations when quantum effects become important to the system. A criterion for evaluating the validity of the Newtonian approximation is the thermal DeBroglie wavelength of the particles involved which is defined as [87]

$$\Lambda = \sqrt{\frac{2\pi\hbar^2}{mk_BT}}, \tag{2.3.1}$$

  where $\hbar$ denotes the Planck constant, k_B is the Boltzmann constant, T is the temperature and m is the pass of the particle. The Newtonian approximation is considered legitimate when $\Lambda \ll a$, where a is the mean nearest neighbour distance of the system. Quantum effects become important in any system when T is sufficiently low. The drop of specific heat of crystals below the Debye temperature or the anomalous behaviour of the thermal expansion coefficient, are well known examples of measurable quantum effects in solid systems.

- Forces realism: In MD dynamics empirical interaction potentials are employed to mimic the behaviour of the real system. As the particles move, the relative positions change and the consequently inter-atomic forces change as well. The realism of the molecular simulations is related to the interaction potentials employed and their ability to mimic the behaviour of the real system under similar to the simulations conditions.

- Computational time and computing power: To illustrate the computational limitations consider an MD simulation of pure water with fixed $O-H$ bonds and fixed $O-H-O$ angles. The time step in the MD is dictated by the highest frequency one needs to resolve and therefore for the aforementioned example a typical time step is $\delta t = 2\ fs$. In order to simulate a period of $1\mu s$ a total number of $5 \cdot 10^8$ time steps is required. Assuming that each single time step requires at least $0.1\ s$ in a personal computer with 3 GHz CPU power, a total number of 19 months is required [30, 88]. This shortcoming prompts the development of multiscale models, aiming to combine the molecular and continuum level modelling in order to make simulation of multiscale physical problems computationally feasible.

2.3.1 Equation of motion

In the classical molecular models, like molecular dynamics or Monte Carlo, the atoms are considered to be the smallest elements and are used to form bigger structures such as crystals or molecules. These modelling approaches are based on the following approximations:

- The atoms are modelled as point masses at positions $\boldsymbol{r}_i$ with mass m_i. 99.9 percent of their mass is concentrated in the position $\boldsymbol{r}_i$, since the motion of the electrons is averaged out.
- The interaction between the atoms i and j is given by a potential $V(\boldsymbol{r}_{ij})$ that is designed to model all forces acting between these two atoms. The interaction potential is approximated by a sum of analytic functions that represent the characteristics of the real world forces.
- In the classical molecular modelling a molecule is represented by a collection of atoms kept together by rigid or semi-rigid bonds. The intra-molecular forces due to bond forming are at least one order of magnitude greater than the inter-molecular forces. Different approximations can be applied for bond modelling based on the physical properties of the simulated molecule. For example, very small compact molecules are usually modelled as rigid structures where on the other hand for large molecules like proteins parametrised potential functions have to be employed.
- In classical molecular modelling the Heisenberg's uncertainty principle is disregarded. The position and the momentum of every particle are precisely known at every point in time and therefore their motion can be described by the classical equations of motion - Newton's laws.

Molecular dynamics, is a deterministic method, where the evolution of the molecular system is calculated by computing the particles' trajectories based on the classical molecular model. The governing system of equations for MD is a system of Newton's equation of motion in the form

$$m_i \ddot{\boldsymbol{r}}_i = -\frac{\partial V_i}{\partial \boldsymbol{r}_i} \tag{2.3.2}$$

written for each atom i modelled as a point mass. In MD the equations of motion are solved numerically via algebraic approximations. A numerical integration method is used to advance the system from time t to $t + \Delta t$.

2.3.2 Interatomic potentials

The potential energy V_i for the atom i is the sum of semi-empirical analytical functions that model the real inter-atomic forces. For example, in the majority of examples discussed in

the current study, a simple Lennard- Jones pair potential is used to model van der Waals attraction and Paulis repulsion forces. The potential is given by

$$V_{ij} = 4 \cdot \epsilon \cdot \left[\left(\frac{\sigma}{r_{ij}} \right)^{12} - \left(\frac{\sigma}{r_{ij}} \right)^{6} \right], \tag{2.3.3}$$

where r_{ij} is the distance between the *ith* and the *jth* particle, ϵ is the characteristic energy level and σ is the molecular length scale defining the position of zero potential energy. The total potential energy of the system can be calculated through summation of all individual pairs:

$$V = \sum_{i}^{N} \sum_{j>i}^{N} V(r_{ij}), \tag{2.3.4}$$

where N is the total number of atoms. The potential of a single atom i is the sum of all potential interactions in which this atom is involved:

$$V_i = \sum_{i \neq j}^{N} V(r_{ij}). \tag{2.3.5}$$

The force acting on each particle is the gradient of the potential with respect to the spatial position of the particle and is computed as follows

$$\boldsymbol{f}_i = \nabla_{\boldsymbol{r}_i} V_i. \tag{2.3.6}$$

The atomic trajectories are calculated by integration of Equation (2.3.2) in time for all atoms. The time integration is performed by a finite difference method such as the predictor-corrector method or the Verlet algorithm [89, 90]. Despite the apparent simplicity, the simulations are extremely demanding computationally due to the huge number of atoms involved, even in the smallest systems. Modern parallel computers allow MD simulations of up to several millions of atoms [91].

2.3.3 Integration algorithms

The time integrator is responsible for moving the particles as the simulation evolves. For integrating the equation of motion forward in time various numerical approaches exist that mainly utilise the finite difference scheme. The time integrator calculates the velocities and the positions of the particles for the next time step based on the velocities and positions on previous ones. A numerical model employed for MD simulations should fulfil the following criteria:

- Efficiency: The efficiency is crucial in molecular dynamics simulations. The molecular dynamics simulations are computational demanding and the computing time is extremely important.

- Stability: The integration algorithm should be stable in the sense that conserves the energy. In many cases stability is a function of various parameters such as the time step size.
- Accuracy: The integrating algorithms should create trajectories that resemble the realistic ones; this can be validated in case where analytical solution is available.

Verlet Algorithm

The Verlet algorithm calculates the atomic trajectories of the next time step based on the positions at both current and previous time steps, without using the velocity. It is a second order approximation of the Newton's equation of motion and is derived through Taylor expansions of the position vector r_i [90]:

$$\boldsymbol{r}(t+\delta t) = \boldsymbol{r}(t) + \boldsymbol{u}(t)\cdot\delta t + \boldsymbol{a}(t)\frac{\delta t^2}{2} + \boldsymbol{b}(t)\frac{\delta t^3}{6} + O(\delta t^4), \tag{2.3.7}$$

$$\boldsymbol{r}(t-\delta t) = \boldsymbol{r}(t) - \boldsymbol{u}(t)\cdot\delta t + \boldsymbol{a}(t)\frac{\delta t^2}{2} - \boldsymbol{b}(t)\frac{\delta t^3}{6} + O(\delta t^4), \tag{2.3.8}$$

where δt is the time step of the simulation, $\boldsymbol{a}_i(t)$ is the acceleration and, $\boldsymbol{b}(t)$ is the third order derivative of the position vector with respect to the time. By adding Equations (2.3.7),(2.3.8) the following expression is obtained

$$\boldsymbol{r}(t+\delta t) = 2\boldsymbol{r}(t) - \boldsymbol{r}(t-\delta t) + \boldsymbol{a}(t)\cdot\delta t^2 + O(\delta t)^4. \tag{2.3.9}$$

From Equation (2.3.9) it is clear that the calculation of the particles' position at the next time level $t+\delta t$ does not require the calculation of the current velocity $\boldsymbol{u}(t)$, which is obtained by a central difference method

$$\boldsymbol{u}(t) = \frac{\boldsymbol{r}(t+\delta t) - \boldsymbol{r}(t-\delta t)}{2\delta t}. \tag{2.3.10}$$

Equation (2.3.9) is fourth order accurate whereas the velocities obtained from Equation (2.3.10) are of second order.

Leap Frog Algorithm

The Leap-Frog algorithm is a modified version of the basic Verlet algorithm. It is a half-step scheme and is based on the calculation of velocities at time $t+\frac{\delta t}{2}$. The calculation sequence for the Leap-Frog algorithm is

1. The acceleration $\boldsymbol{a}(t)$ is calculated by the derivative of the potential function

$$\boldsymbol{a}_i(t) = \frac{1}{m_i}\nabla V_i \tag{2.3.11}$$

2. Based on the acceleration $\boldsymbol{a}(t)$ the velocities $\boldsymbol{u}\left(t + \frac{\delta t}{2}\right)$ is calculated as

$$\boldsymbol{u}\left(t + \frac{\delta t}{2}\right) = \boldsymbol{u}\left(t - \frac{\delta t}{2}\right) + \boldsymbol{a}(t) \cdot \delta t \tag{2.3.12}$$

3. The positions $\boldsymbol{r}(t + \delta t)$ are calculated as

$$\boldsymbol{r}\,(t + \delta t) = \boldsymbol{r}(t) + \boldsymbol{u}\left(t + \frac{\delta t}{2}\right) \cdot \delta t \tag{2.3.13}$$

Velocity Verlet Algorithm

A common disadvantage for the Verlet and the Leap Frog algorithms is that the atomistic positions and velocities are not available at the same time. To overcome this a variant of the Verlet algorithm has been developed that uses positions $\boldsymbol{r}_i(t)$, velocities $\boldsymbol{u}_i(t)$ and accelerations $\boldsymbol{a}_i(t)$ defined at the same time [90]. The calculation sequence is

1. The velocity is advanced by a half step $\frac{\delta t}{2}$

$$\boldsymbol{u}\left(t + \frac{\delta t}{2}\right) = \boldsymbol{u}(t) + \boldsymbol{a}(t) \cdot \frac{\delta t^2}{2} \tag{2.3.14}$$

2. The positions are advance to $\boldsymbol{r}(t + \delta t)$

$$\boldsymbol{r}(t + \delta t) = \boldsymbol{r}(t) + \delta t \cdot \boldsymbol{u}(t) + \frac{\delta t^2}{2} \cdot \boldsymbol{a}(t) \tag{2.3.15}$$

3. The acceleration $\boldsymbol{a}(t + \delta t)$ is calculated from the interaction potentials (Equation 2.3.11)

4. Another half step is performed to complete the velocity calculation

$$\boldsymbol{u}(t + \delta t) = \boldsymbol{u}(t + \frac{1}{2}\delta t) + \frac{1}{2}\delta t \cdot \boldsymbol{a}(t + \delta t) \tag{2.3.16}$$

The velocity Verlet algorithm therefore propagates velocities in two stages and split the calculations process into the applied acceleration term.

2.3.4 Boundary conditions

The imposition of boundary conditions is a very important topic of all the numerical simulations. In MD the most commonly used boundary conditions are the periodic ones (PBC). Other boundary conditions that are usually employed are those that lead to non-equilibrium conditions like for example the Lees-Edwards boundary conditions (LEBC).

Periodic boundary conditions

Traditionally, the most often applied boundary conditions in molecular dynamics simulations are periodic boundary condition because they allow the simulation of a homogenous infinite system with a limited number of atoms, which were the only systems that could be simulated with early computers. Periodic boundary conditions copy identical images of the computational box aligned to a space-filling array throughout the space (see Figure 2.1). This approach mimics an infinite computational domain with a finite number of molecules. To implement this condition the following has to be applied:

1. Every atom leaving the box in one direction, enters at the same time from the opposite side. Therefore, one needs to check regularly whether an atom has crossed the boundary and to correct its position accordingly.
2. Every atom whose position is within interaction distance of the boundary interacts with the images of the atoms from the opposite side of the simulation box. This wrap-around effect must be taken into account when calculating the interatomic potentials or forces. While the periodic boundary condition circumvent elegantly the problem of surface atoms, they create another. For calculating the potentials or forces, it would strictly be required to evaluate the interaction between all pairs of the computational box and their images, which is an infinite number of interactions. For short-range forces this problem is overcome through the minimum image convention which is based on the usage of a cut-off distance. Therefore, only the closest periodic image of an interaction between two atoms must be regarded.

Lees-Edwards boundary conditions

LEBC have been developed to deal with accuracy and efficiency issues that arise when the normal periodic boundary conditions are applied for shear flows problems. In this type of boundary conditions the neighbouring cells are shifted, as shown in Figure 2.2, with a constant velocity U calculated from the desired shear rate.

In the LEBC method, every particle that moves out of a cell is replaced by its periodic image. Suppose that a particle moves through the lower face then its periodic image has

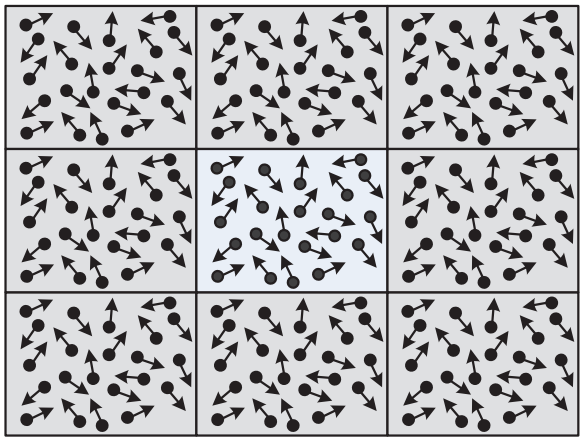

Figure 2.1: Periodic boundary conditions

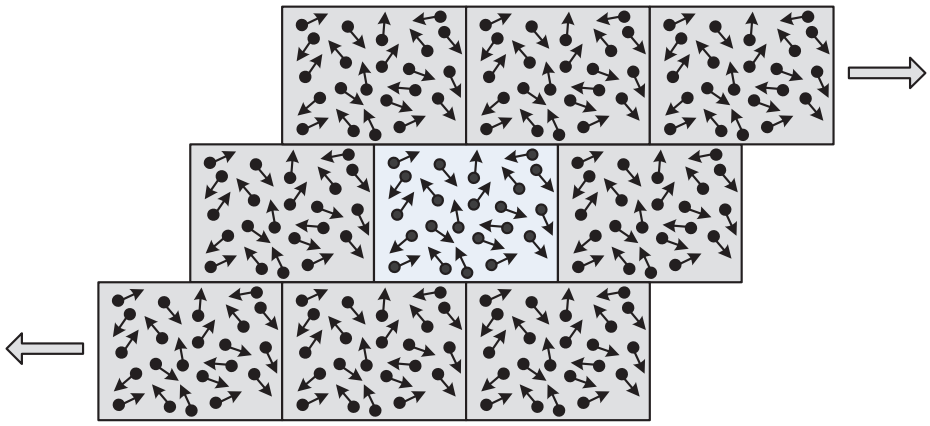

Figure 2.2: Schematic representation of LEBC

to be inserted at the upper boundary, however the presence of the shear implies that the inserted particle is transferred from a faster moving fluid layer. Therefore, the inserted particle will neither have the same velocity nor the same coordinates as the original particle. Coordinates and velocities of the inserted atoms have to be corrected and through these amendments a stable linear velocity profile is generated in the computational domain.

A particle P that leaves the lower boundary and is re-inserted through the upper one has an additional velocity component U along the x direction and therefore its new velocity $\boldsymbol{u}'$ is

$$\boldsymbol{u}' = \begin{cases} u_x + U \\ u_y \\ u_z \end{cases} \tag{2.3.17}$$

At the same time, the upper image is transported, so that the entry point cannot be the P' shown in Figure 2.3, instead an additional correction should be taken into account and

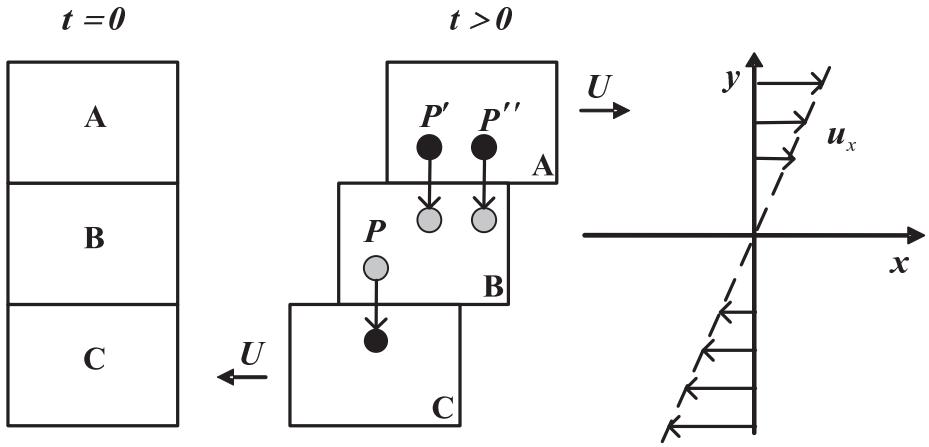

Figure 2.3: Position correction for a moving particle in the LEBC

the new insertion point is the P''. The displacement $\Delta x = x_{P''} - x_{P'}$ is calculated using

$$\Delta x = L\dot{\gamma}t, \tag{2.3.18}$$

where t is the time, L is the cell length in y direction and $\dot{\gamma}$ is the flow's shear rate

$$\dot{\gamma} = \frac{\partial u_x}{\partial y} = \frac{U}{L} \tag{2.3.19}$$

The same procedure is applied for particles leaving the upper boundary and re-entering through the lower one, with the corresponding changes due to the opposite velocity values of the neighbouring cells. The LEBC approach requires a minimum simulation time, approximately equal to the traversal time of the primitive cell, in order to resolve the shear introduced due to the boundary movement.

2.3.5 Calculation of Macroscopic Properties

In the hybrid molecular-continuum frameworks molecular calculations of any hydrodynamic quantity, such as velocity or density, are subject to spatial and temporal fluctuations due to the small number of atoms included in the atomistic region. In this context it is important to quantify these fluctuations,which are originated from the thermal motion of atoms, and obtain a quantitative and qualitative understanding regarding their propagation from the microscopic to the macroscopic description and vice versa. Generally, the strength of the fluctuations can be reduced either by increasing the number of the simulated atoms or performing additional time averaging. However, both additional particles and averaging add a further computational burden to the overall simulation procedure and therefore the selection regarding the number of particles and the time averaging should be made cautiously.

Averaging Time

Time averaging has been acknowledged as one potential approach to reduce the fluctuations' strength. In the time averaging the instantaneous values of a physical quantity A are averaged over a period of time δt_{av}. The value of δt_{ave} is specified depending on the nature of the problem, steady or unsteady, and the computational resources availiable. The averaging of a macroscopic quantity A from time t_m for a period δt_{av} is given by [92]

$$\langle A \rangle = \frac{1}{\delta t_{av}} \int_{t_m}^{t_m+\delta t_{av}} A(t)dt = \frac{1}{N_m} \sum_{i=1}^{i=N_m} A(\tau_m) \tag{2.3.20}$$

where N_m is the number of times that the quantity A is calculated, and the measurements are taken every $\delta t_m = \frac{1}{N_m}\delta t_{av}$

The number of samples utilised for estimation of a thermodynamic parameter have a big impact to the strength of the associated fluctuations. The number of samples can be maximised by performing averaging every integration time step however in this case there is a large number of samples that are statistically correlated and does not contribute to the reduction of the expected error. In MD the correlation time has to be taken into account in order to avoid any additional computational cost that reduces the efficiency of the simulation[90]. The correlation time can be read off the autocorrelation function over time lags. The autocorrelation function of a variable $\mathcal{A}$ is calculated by

$$\phi(\mathcal{A}, \tau_c) = \frac{1}{M - \tau_c} \sum_{\tau_m=1}^{M-\tau_c} \mathcal{A}(\tau_m)\mathcal{A}(\tau_m + \tau_c) \ , \tag{2.3.21}$$

where τ_c is the time lag and the sum runs over the products of the variable of interest at the times τ_m and $\tau_m + \tau_c$.

Statistical Errors

Standard deviation of physical substance $\langle \mathcal{A} \rangle_\tau$ is usually employed to quantify its fluctuations strength. Basically, it gives the average deviation of any computed value $\langle \mathcal{A} \rangle_\tau$ from the true value of $\mathcal{A}$. Assuming that the individual quantities $\mathcal{A}(\tau)$ are independent from each other, it is defined by

$$\sigma(\langle \mathcal{A} \rangle_t) = \sqrt{\sigma^2(\langle \mathcal{A} \rangle_t)} \ , \tag{2.3.22}$$

with $\sigma^2(\langle \mathcal{A} \rangle_t)$ begin the variance in $\langle A \rangle_t$ that is simple given by

$$\sigma^2(\langle \mathcal{A} \rangle_t) = \frac{\sigma^2(\mathcal{A})}{M} \ , \tag{2.3.23}$$

where $\sigma^2(\mathcal{A})$ is the sample variance:

$$\sigma^2(\mathcal{A}) = \frac{1}{M-1}\sum_{\tau_m=1}^{M}(\mathcal{A}(\tau_m) - \langle\mathcal{A}\rangle_t)^2 \ . \tag{2.3.24}$$

The average deviation from the mean is called the standard deviation is simply $\sigma(\mathcal{A}) = \sqrt{\sigma^2(\mathcal{A})}$ and $\sigma(\langle\mathcal{A}\rangle_t) = \sqrt{\sigma^2(\langle\mathcal{A}\rangle_t)}$ for the instantaneous variable and its time average respectively.

In the hybrid continuum-molecular frameworks the state variables density ρ, velocity $\boldsymbol{u}$ and energy density e are measured at the molecular domain and afterwards this information is transfered to the continuum solver. Therefore, it is important to have a quantitative understanding of their fluctuations magnitude. For a time averaged quantity $\langle\mathcal{A}\rangle_t$ the average fluctuation strength can be defined as the fractional error, which is the standard deviation of $\langle\mathcal{A}\rangle_t$ over its true value:

$$F_{\langle\mathcal{A}\rangle_t} = \frac{\sigma(\langle\mathcal{A}\rangle_t)}{|\mathcal{A}|} = \frac{\sqrt{\sigma^2(\langle\mathcal{A}\rangle_t)}}{|\mathcal{A}|} \ . \tag{2.3.25}$$

An important parameter that one may need to calculate is the number of time steps M, that the averaging has to be performed in order to reduce the fluctuations level below an acceptable value. In that sense, Equation (2.3.25) can be rearranged to give the minimum value for M:

$$M = \frac{\sigma^2(\mathcal{A})}{F^2{\mathcal{A}_0}^2} \ , \tag{2.3.26}$$

where $\mathcal{A}_0$ is the true value or the the limit of the average: $\mathcal{A}_0 = \lim_{t\to\infty}\langle\mathcal{A}\rangle_t$.

The predictions can be given for: density, ρ; velocity in one dimension, u_α; temperature, T; and pressure, P. Since the fluctuation strength is based on the standard deviations $\sigma(A)$ of the variables (q.v. Equation (2.3.25)) one has to start with those definitions:

$$\sigma(\rho) = \frac{m\sqrt{N}}{VAc} \ , \tag{2.3.27}$$

$$\sigma(u_\alpha) = \sqrt{\frac{k_BT}{mN}} \ , \tag{2.3.28}$$

$$\tag{2.3.29}$$

$$\sigma(T) = \sqrt{\frac{k_BT^2}{c_vN}} \ , \tag{2.3.30}$$

$$\sigma(P) = \frac{k_BTAc\sqrt{\gamma N}}{V} \ . \tag{2.3.31}$$

It is assumed that the variables of interest are calculated from N atoms. The acoustic number Ac is the ratio of the speed of sound of the fluid c to the speed of sound of an ideal gas a^i: $Ac = a/a^i$. k_B is Boltzmann's constant, m the molecular mass, c_v the specific heat

capacity (constant volume) and γ the ratio of the heat capacities $\gamma = c_p/c_v$.

From the instantaneous standard deviations of Equation (2.3.27) - 2.3.31 one easily obtains the time averaged standard deviation. These can be related to the absolute variable values: ρ_0 for the density; $u_{0\alpha}$ for velocity in dimension α; e_{int0} for the internal energy density; T_0 for temperature; and P_0 for pressure, to give a prediction for the fluctuation strength (q.v. Equation (2.3.25)):

$$F_{\langle\rho\rangle_t} = \frac{\sigma(\langle\rho\rangle_t)}{\rho_0} = \frac{1}{\sqrt{MN}}\frac{1}{Ac} \tag{2.3.32}$$

$$F_{\langle u\rangle_t} = \frac{\sigma(\langle u_\alpha\rangle_t)}{|u_{0\alpha}|} = \frac{1}{\sqrt{MN}}\frac{1}{AcMa\sqrt{\gamma}} \tag{2.3.33}$$

$$F_{\langle T\rangle_t} = \frac{\sigma(\langle T\rangle_t)}{T_0} = \frac{1}{\sqrt{MN}}\sqrt{\frac{k_B}{c_v}} \tag{2.3.34}$$

$$F_{\langle P\rangle_t} = \frac{\sigma(\langle P\rangle_t)}{P_0} = \frac{1}{\sqrt{MN}}\frac{k_B T AcN\sqrt{\gamma}}{P_0 V}\,, \tag{2.3.35}$$

where Ma is the local mach-number: $Ma = u0_\alpha/c$. For most cases considered here, i e. mono atomic substances, $C_V = (3/2)k_B$.

Now, the most interesting question is: Over how many time steps M does someone average to reduce the fraction fluctuation below an acceptable level, for instance $F = 5\,\%$. To this end, Equations (2.3.32) - 2.3.35 can be rearranged to give the minimum value for M:

$$M_\rho = \frac{1}{F^2}\frac{1}{NAc^2} \tag{2.3.36}$$

$$M_u = \frac{1}{F^2}\frac{1}{NAc^2Ma^2\gamma} \tag{2.3.37}$$

$$M_{e_{int}} = \frac{1}{F^2}\frac{k_B T^2 c_v N}{(e_{i0})^2 V^2} \tag{2.3.38}$$

$$M_T = \frac{1}{F^2}\frac{k_B}{Nc_v} \tag{2.3.39}$$

$$M_P = \frac{1}{F^2}\frac{{k_B}^2 T^2 Ac^2 N^2\gamma}{P_0 V}\,. \tag{2.3.40}$$

An automatic calculation simulation mode was used in all the performed atomistic simulations. During the simulation procedure, a minimum number of time step was calculated (based on the above equations) until the mean values of the state variable satisfy a minimum

confidence level of 95%.

2.4 Geometrical Coupling

Geometrical coupling is based on the decomposition of the computational domain into two distinct regions where the continuum and molecular solvers are applied, as shown in Figure 2.4. The cornerstone for the physical consistency and successful application of this coupling scheme is the robust design of the hybrid solution interface (HSI). Two fundamental approaches to the coupling process have been introduced in the past leading to a number of coupling methodologies:

- Coupling through fluxes: The interface should satisfy a basic physical principle, the conservation of mass, momentum and energy flux. Therefore, momentum, mass or energy should be able to flow seamlessly from one description to the other and vice versa.
- Coupling through state: The profiles of the primitive variables such as density, temperature and velocity must be consistent between the two descriptions. To further illustrate that, someone must not be able to identify where the interface is placed based on the primitive variables profiles across the entire domain.

The selection of the most suitable coupling method is not a trivial task and is primarily problem dependent. Compressible and incompressible formulations are associated with different physical and mathematical hydrodynamics limits [35, 93]. Compressibility effects can be a criterion for determining the most suitable coupling approach with time-explicit coupling through fluxes usually used for compressible formulations and the state coupling for incompressible ones [93].

The molecular model has more degrees of freedom and incorporates more information than the continuum model. When the information, in the form of a state or flux, is transferred from the molecular to the continuum model, the amount of information available is reduced through averaging or integration. For example, while there are technical challenges associated with this process, it is straightforward conceptually. In the hybrid multiscale methods the most challenging operation is the transfer of information from the continuum to the molecular description. In this process additional information describing degrees of freedom present in the molecular model but absent from the continuum model must be generated. In the following sections the application of the continuum information to the molecular domain is discussed.

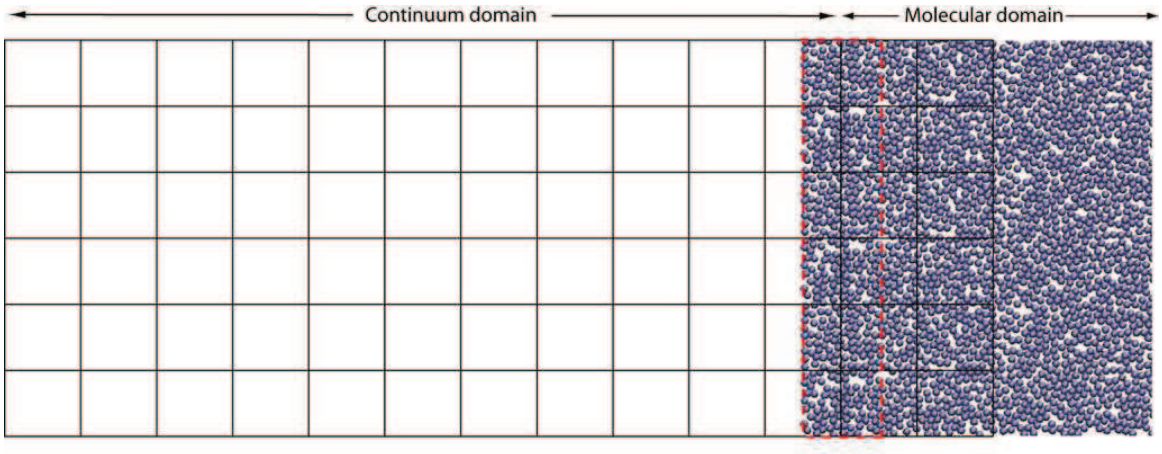

Figure 2.4: Hybrid Solution Interface

2.4.1 Coupling Through Fluxes

The flux coupling scheme is conceptually related to finite volume continuum solvers, where the fluxes between neighbouring cells are calculated and the net flux used to update the average value of conserved variables. Typically, in the multiscale frameworks the fluxes of the conserved variables, that is mass, momentum and energy, are separated into fluxes due to convection, stress and diffusion [13]. The convective flux is the transport of a quantity due to the movement of the fluid elements while stress and diffusive fluxes represent transport of a quantity due to interatomic forces and diffusion phenomena respectively. The fluxes calculated from a volume V_S in continuum and molecular formulations are given by:

- Mass Flux
  - Convective

$$\rho \boldsymbol{u} = \frac{1}{V_S} \left\langle \sum_{i \in V_S} m_i \boldsymbol{u}_i \right\rangle \tag{2.4.1}$$

- Momentum Flux
  - Convective

$$\rho \boldsymbol{u} \otimes \boldsymbol{u} = \frac{1}{V_S} \left\langle \sum_{i \in V_S} m_i \boldsymbol{u}_i \otimes \boldsymbol{u}_i \right\rangle \tag{2.4.2}$$

  - Stress

$$\boldsymbol{\Pi} = \frac{1}{V_S} \left\langle \sum_{i,j \in V_S} \boldsymbol{r}_{ij} \otimes \boldsymbol{f}_{ij} \right\rangle \tag{2.4.3}$$

- Energy Flux

– Convective

$$E\boldsymbol{u} = \frac{1}{V_S}\left\langle \sum_{i \in V_S} E_i \boldsymbol{u}_i \right\rangle \tag{2.4.4}$$

– dissipative and conductive

$$\boldsymbol{\Pi} \cdot \boldsymbol{u} + \boldsymbol{q} = \frac{1}{V_S}\left\langle \sum_{i,j \in V_S} \left(\boldsymbol{r}_{ij} \otimes \boldsymbol{f}_{ij}\right) \cdot \boldsymbol{u}_i \right\rangle \tag{2.4.5}$$

Where the continuum parameters include the fluid density ρ, fluid velocity $\boldsymbol{u}$, total energy E and shear stress tensor $\boldsymbol{\Pi}$. Molecular parameters include m_i and u_i denoting the mass and velocity of the *ith* particle respectively and $\boldsymbol{f}_{ij}$ denoting the force acting between particles i and j.

Momentum Flux

The exchange of momentum across the overlapping region is expressed through Equations (2.4.2) and (2.4.3) and can be summarised in a unified expression as follows

$$\rho \boldsymbol{u} \otimes \boldsymbol{u} + \Pi = \frac{1}{V_S}\left(\left\langle \sum_{i \in V_S} m_i \boldsymbol{u}_i \otimes \boldsymbol{u}_i \right\rangle + \left\langle \sum_{i,j \in V_S} \boldsymbol{r}_{ij} \otimes \boldsymbol{f}_{ij} \right\rangle\right). \tag{2.4.6}$$

The momentum transfer due to convection is balanced by manipulating the average velocity of the particles inside the overlapping domain in order to make it equal to the continuum velocity. The average velocity is adjusted as follows

$$\boldsymbol{u}_i^{new} = \boldsymbol{u}_i^{old} + \left(\boldsymbol{u} - \frac{\sum\limits_{i \in \partial R} m_i \boldsymbol{u}_i^{old}}{\sum\limits_{i \in \partial R} m_i}\right), \tag{2.4.7}$$

where $\boldsymbol{u}_i$ is the velocity of the i^{th} particle, $\boldsymbol{u}$ is the continuum velocity, m_i the mass of the i^{th} particle and ∂R is the overlapping region. The momentum flux due to stresses is represented at micro scale as an external force applied throughout the overlapping region. The main challenge associated with the determination of the external force is that only the average acting force is known and its distribution is not unique. The following general representation for the external force applied to each particle has been proposed [94]

$$\boldsymbol{F}_i^{ext} = -\frac{f(\boldsymbol{r}_i)}{\sum\limits_{i \in \partial R} f(\boldsymbol{r}_i)} \cdot A\boldsymbol{\Pi} \cdot \boldsymbol{n}, \tag{2.4.8}$$

where $f(\boldsymbol{r}_i)$ is a distribution function for the force based on the particle's position. The selection of the distribution function is crucial for the successful application of the scheme.

Incorrect choice of the distribution function can lead to artifacts in the solution, for example it can cause particles to drift away from the molecular region. Several types of the distribution function have been used in the early development of the hybrid algorithms, for example a function $f(\boldsymbol{r}_i) = 1$ has been utilised in a number of studies [19, 95]. However, recent studies [13, 16] indicated that imposing momentum flux through a force causes instabilities in the simulation procedure and can adversely affect the energy flux transfer. Specifically, the force mechanism for the momentum transfer results in relaxation zone that starts from the outer boundary of the HSI and extends for distance δl where the density drops from its bulk value to zero. The density decrease in the relaxation zone, particularly if it is slow, leads to different physical behaviour due to the differences in the transport properties such as viscosity and thermal conductivity. There are also cases [16] where the density profile, at the outer boundary of the hybrid interface, tends asymptotically to a value different from zero, meaning that atoms are drifting away from the molecular region. A number of approaches have been proposed in order to circumvent these issues. For example, it is possible to remove atoms that cross the outer molecular boundary and re-insert them inside the overlapping region at a location which has the same potential energy [96]. Another approach is to stop integrating the positions and the velocities of those atoms and due to the external forces that are still applied they will be transported further into the particle area. However, it has been noticed that these procedures cause an undesirable decrease in the total energy. The external force that is applied to the atoms in the overlapping region can be understood as an external energy field and every atom experiences a force according to the external potential energy given by

$$E^{ext}(\boldsymbol{r}_i) = \frac{1}{N_B}\boldsymbol{F}^{ext} \cdot (\boldsymbol{r}_i - \boldsymbol{r}_0), \tag{2.4.9}$$

where N_B is the number of atoms in the overlapping region, $\boldsymbol{r}_i$ is the position of the atom and $\boldsymbol{r}_0$ is the position of the inner boundary of the overlapping region. Hence, if one atom is shifted towards the overlapping region its potential energy is reduced due the external field. This decrease of the potential energy has to be balanced in order for the total energy to remain constant. This can be achieved by rescaling the velocities of the atoms and therefore by altering the internal energy of the system without introducing or removing any additional momentum [16].

The behaviour of the momentum flux transfer through external forces, despite the energy correction scheme, continue to experience stability issues[13]. If the velocity in the overlapping region presents small deviations compared to the macroscopic one then the energy transferred is not the appropriate one and as a consequence, apparent oscillations of the state variables are generated. A technique that has been recently proposed is the momentum flux transfer through velocity reversing of the outermost particles that are about to escape from the molecular region [16]. Reversing the component in the direction a of the velocity vector $\boldsymbol{u}_i$ of a particle i that is about to escape the molecular domain, $u_{i,a}^{new} = -u_{i,a}^{old}$, will introduce a momentum of $2m_i u_{i,a}$ in the corresponding direction without transferring any energy. In this technique the momentum can be transferred in discrete quantities of $2m_i u_{i,a}$ and therefore the velocities of the outermost atoms that are pointing out of the molecular region will be reversed until the desirable amount of momentum is transferred to the molecular system. The performance of the velocity reversing algorithm presents superior

characteristics compared to the momentum transfer by force due to the fact that the momentum and energy flux can be controlled independently. In addition the density profiles in the overlapping region are sharper and therefore more physically consistent [13, 16].

Energy Flux

The energy flux, as aforementioned, is separated into three components, energy flux due to convection $F_{ec} = -E\boldsymbol{u}\cdot A\boldsymbol{n}$, due to stresses $F_{es} = -\boldsymbol{\Pi}\cdot\boldsymbol{u}\cdot A\boldsymbol{n}$ and due to conduction $F_{eq} = \boldsymbol{q}\cdot A\boldsymbol{n}$. Generally, the energy must be conserved throughout the entire computational domain and therefore each of the kinetic, potential and internal component of the particles' energy has to be examined separately. The kinetic and internal energy are maintained through the balance between the macroscopic and the average microscopic velocity and temperature respectively in the HSI. The most challenging task in the energy transfer procedure is the conservation of the potential energy when, due to the mass flux, new particles are inserted into the molecular region. In order to satisfy the potential energy conservation, the new particles, have to be placed in very specific positions which depend on the local distribution of the rest of the atoms. These issues can be addressed through the USHER algorithm, proposed in [96]. This algorithm is described in the mass flux subsection.

The balance of the energy flux due to conduction requires the implementation of a scheme capable to handle heat transfer between the two descriptions. Such schemes have not been extensively explored since the majority of the studies are focused on isothermal flows and therefore rigorous conclusions cannot be drawn yet. Several suggestions can be provided in order to establish the heat transfer between the two domains including, (i) the application of a force to the "hotter" atoms along the heat flux direction, (ii) the rescaling of the internal energy based on the heat flux [16, 92], (iii) the utilisation of the Chapman-Enskog velocity distribution [21] in order to apply the preferred heat flux and (iv) the application of temperature gradient in discrete regions through Nose-Hoover thermostats [95].

The energy exchange scheme due to stress is directly related to the procedure employed for the momentum flux transfer. Therefore, two procedures can be suggested, one for the energy transfer by force and one for the energy transfer by velocity reversing. In the first case external forces are utilised not only for applying the desirable momentum flux but also for transferring information regarding the stress energy flux. Generally, the energy balance is expressed as

$$\left\langle \sum_{i\in\partial R} \boldsymbol{F}_i^{ext}\cdot\boldsymbol{v}_i \right\rangle = -A\boldsymbol{\Pi}\cdot\boldsymbol{u}\cdot\boldsymbol{n}. \tag{2.4.10}$$

Suppose that $\boldsymbol{F}_i^{ext} = \boldsymbol{F}^{ext} = \text{const}$ then the above can be simplified to

$$\boldsymbol{F}^{ext}\cdot\left\langle \sum_{i\in\partial R} \boldsymbol{v}_i \right\rangle = -A\boldsymbol{\Pi}\cdot\boldsymbol{u}\cdot\boldsymbol{n}. \tag{2.4.11}$$

From Equation (2.4.11) the energy conservation due to stress can be guaranteed if both of the following two statements are satisfied: (i) the average molecular velocity in the overlapping region is equal to the continuum one and (ii) the external force applied to the particle region is equal to

$$\boldsymbol{F}^{ext} = -\frac{1}{N_B} A\boldsymbol{\Pi} \cdot \boldsymbol{n}. \tag{2.4.12}$$

In the case where the momentum flux is applied through the velocity reversing scheme the energy flux has to be transferred independently. This is achieved through the scaling of the velocity vectors of all the atoms inside the HSI. The scalar quantity F_{es} of the energy flux due to stress can be expressed as a vector $\boldsymbol{F}_{es} = \left[(-\boldsymbol{\Pi} \cdot \boldsymbol{n})\, u_x, (-\boldsymbol{\Pi} \cdot \boldsymbol{n})\, u_y, (-\boldsymbol{\Pi} \cdot \boldsymbol{n})\, u_z\right]$ where the scalar energy is given as $F_{es} = \boldsymbol{F}_{es} \cdot \boldsymbol{F}_{es}^T$. The velocities of the atoms are scaled in each respective dimension a as follows [16]

$$u_{i,a}^{new} = u_{i,a}^{old} \cdot f + c. \tag{2.4.13}$$

The parameter f is the scaling factor calculated as

$$f = \sqrt{1 + F_{es,a}/E_{k,int,a}}, \tag{2.4.14}$$

where $E_{k,int,a}$ is the internal kinetic energy of the particles in the overlapping region along the direction a

$$E_{k,int,a} = \sum_{1}^{N_B} \frac{1}{2} m_i (\boldsymbol{u}_{i,a} - \boldsymbol{u}_{b,a})^2, \tag{2.4.15}$$

and $\boldsymbol{u}_{b,a}$ is the average velocity of the atoms in the overlapping region. The parameter c is chosen to ensure that the net momentum will remain the same after the scaling:

$$c = \frac{1 - f}{M} \sum_{1}^{N_B} m_i u_{i,a}, \tag{2.4.16}$$

where M is the total mass of the particles inside the overlapping region.

Mass Flux

If there is mass transfer across the hybrid interface then the continuity of mass in the molecular region can be ensured only by inserting or removing particles, depending on whether mass is transferred to or from the atomistic domain. If the rate of the particles insertion or extraction is given by s, then the mass continuity is expressed as follows:

$$ms = -A\boldsymbol{u} \cdot \boldsymbol{n}, \tag{2.4.17}$$

where m is the average mass of the particles inside the overlapping domain. Positive values of s indicate that particles are inserted from the continuum to the molecular area and

Algorithm 1 USHER Algorithm

STEP 1: Place the new particle at an initial position inside the overlapping area $r^{(0)}$

STEP 2: Evaluate the $f_{N+1} = \sum_{j=1}^{N} f_{N+1,j}$ and the $\delta t_\sigma = \sqrt{\frac{2\delta r}{|f_{N+1}|}}$. Typically $\delta r \simeq \sigma$ can be used. Note: σ is the characteristic length scale

STEP 3: Move the new particle: $r^{(n+1)} = r^{(n)} + \frac{1}{2} f_{N+1}^{(n)} \delta t^2$ where $\delta t = \min(\Delta t, \delta t_\sigma)$ and $\Delta t = 0.05$ in reduced units

STEP 4: Calculate the relative distance between the specific internal energy of the new particle,ψ_{N+1}^{new}, and the one prescribed by the continuum ϕ, $R_{err} = \left|\psi_{N+1}^{new} - \phi\right| / |\phi|$

STEP 5: The process stops when the R_{err} reaches the desired level of accuracy.

negative values indicate that particles are removed from the particle domain. The particle insertion into the molecular domain is one of the most difficult processes in the flux coupling due to the balance of potential energy which arises from the continuity of the energy flux. The USHER algorithm [96, 97] has been developed in order to address this issue. The main idea is to place the new particles in positions with almost the same potential energy. When a new particle is inserted the rest of the particles are frozen [96].

2.4.2 Coupling Through State

The state coupling is primarily suitable for incompressible problems where the physics of the flow dictates the selection of the appropriate numerical formulations [93]. In this type of hybrid schemes the molecular and continuum density, velocity, temperature and pressure are matched in the overlapping region. Several approaches have been proposed in the literature for the state coupling. These can be broadly classified into approaches based on the constrained Lagrangian dynamics (CLD) [17, 23, 98, 99] and approaches based on the Schwarz method [14, 24, 100].

Constrained Lagrangian Dynamics Schemes

The application of the CLD should ensure the continuity of the physical quantities across the interface and therefore the particles' velocities and positions in the overlapping region are integrated to follow the continuum state through a relaxation mechanism. Specifically, the velocity continuity in the HSI implies that the local average of particles velocities, $\boldsymbol{u}_i$, is equal to the continuum velocity $\boldsymbol{u}$

$$\langle \boldsymbol{u}_i \rangle = \boldsymbol{u}(t). \tag{2.4.18}$$

The Lagrangian derivative of the above equation is

$$\frac{1}{N_B}\sum_{i\in\partial R}\ddot{\boldsymbol{r}}_i = \frac{D\boldsymbol{u}(t)}{Dt} \tag{2.4.19}$$

and the general solution of Equation (2.4.19) is given by

$$\ddot{\boldsymbol{r}}_i = \frac{D\boldsymbol{u}(t)}{Dt} + \zeta_i, \tag{2.4.20}$$

where ζ_i is a variable with the value of the sum over all the cells inside the HSI being equal to zero [101]. Taking into account that the variable ζ_i can be written in following general form

$$\zeta_i = \xi_i\left(\frac{\boldsymbol{F}_i}{m_i} - \frac{1}{N_B}\sum_{i\in\partial R}\frac{\boldsymbol{F}_i}{m_i}\right), \tag{2.4.21}$$

where ξ_i is a real number, and using Equation (2.4.21), the constrained equation of motion for each particle can be obtained in the following form

$$\ddot{\boldsymbol{r}}_i = \frac{1}{\Delta t_{MD}}\left[\boldsymbol{u}(t+\Delta t_{MD}) - \frac{1}{N_B}\sum_{i\in\partial R}\dot{\boldsymbol{r}}(t)\right] + \xi_i\left[\frac{\boldsymbol{F}_i(t)}{m_i} - \frac{1}{N_B}\sum_{i\in\partial R}\frac{\boldsymbol{F}_i(t)}{m_i}\right]. \tag{2.4.22}$$

The co-efficient ξ_i essentially controls the strength of the constraint relation and the relation rate. The following three methods have been proposed in order to select the optimal value of the co-efficient ξ_i :

- It is possible to choose $\xi_i \ll 1$ aiming to suppress any fluctuations generated. For example, a value of $\xi_i = \text{const} = 0.01$ has been used in [102].
- Alternatively one can select $\xi_i = \text{const} = 1$ [101] in order to force the local mean velocity of the particles to be equal to the continuum one.
- Finally it is possible to determine the values of ξ_i dynamically:

$$\xi_i(t+\Delta t_{MD}) = \frac{\frac{1}{N_B}\sum_{i\in\partial R}\left(\ddot{\boldsymbol{r}}_i(t) - \frac{\boldsymbol{F}_i(t)}{m_i}\right)}{\boldsymbol{u}(t) - \frac{1}{N_B}\sum_{i\in\partial R}\boldsymbol{u}_i(t)}. \tag{2.4.23}$$

  In this approach different values of the coupling parameter can be employed for every cell inside the HSI in every time step [18].

The selection of the coupling parameter ξ_i has a significant effect on the behaviour of the coupling scheme. Small values of the parameter may cause physical inconsistencies between the continuum and molecular description. On the other hand large values may contribute to an excessive damping of particles fluctuations and consequently to divergence between the two macroscopic and microscopic solutions.

In the CLD methods the continuum pressure is applied to the molecular region through an external force in a similar fashion to the application of momentum flux due to stress. Specifically, the external force is applied in a direction perpendicular to the HSI boundary. The following formula for the pressure force has been proposed in [99]:

$$\boldsymbol{F}(\boldsymbol{r}_i) = -aP_{con}\sigma\frac{\boldsymbol{r}_i\cdot\boldsymbol{n}-\boldsymbol{r_2}\cdot\boldsymbol{n}}{1-\frac{\boldsymbol{r}_i\cdot\boldsymbol{n}-\boldsymbol{r_2}\cdot\boldsymbol{n}}{\boldsymbol{r}_1\cdot\boldsymbol{n}-\boldsymbol{r_2}\cdot\boldsymbol{n}}}\boldsymbol{n}, \tag{2.4.24}$$

where P_{con} is the continuum pressure applied to the molecular description, $\boldsymbol{r}_i$ is the position of the i^{th} particle, $\boldsymbol{r}_1$ represents the outer boundary of the overlapping region and $\boldsymbol{r}_2$ the inner one.

The macroscopic temperature, T_{con} , is applied to the molecular domain by rescaling the thermal fluctuations of the particles inside the overlapping region. The rescaling is performed as follows

$$\boldsymbol{u}_i = \boldsymbol{u} + \sqrt{\frac{T_{con}}{T_{MD}}}\left(\boldsymbol{u}_i - \boldsymbol{u}\right), \tag{2.4.25}$$

where T_{MD} is the current temperature inside the atomistic domain. In this method the thermal fluctuations of the particles around their mean velocity are rescaled and not the particles' velocities [99]. When the particles velocities are rescaled the mean velocity of the molecular description inside the HSI will be significantly altered leading to undesirable artifacts. A weakness of the current method is the elimination of the intrinsic fluctuations between the potential and kinetic energy [99].

Schwarz Method Schemes

The main drawback of the state coupling through CLD and the flux coupling techniques is that the time scales between the atomistic and continuum solvers are not decoupled. The explicit integration of the molecular domain negatively affects the efficiency of the hybrid schemes.

An approach that has been proposed to handle the time scales limitations within the state coupling framework, is the Schwarz algorithm [24, 93]. The Schwarz algorithm is an iterative procedure that leads to a steady solution and its implicit nature enables the time scales decoupling. The technique employs a relaxation scheme, like for example (2.4.26), in order to update the solution of one description inside the overlapping region

$$\boldsymbol{u}_{MD}^{n+1} = \theta\boldsymbol{u}_{MD}^{n} + (1-\theta)\boldsymbol{u}_{C}^{n}, \tag{2.4.26}$$

where $\boldsymbol{u}_{MD}^{n+1}$ and $\boldsymbol{u}_{MD}^{n}$ are the averaged molecular velocities at the n and $n+1$ iteration respectively, $\boldsymbol{u}_{C}^{n}$ is the continuum velocity at the *nth* iteration and θ is the relaxation parameter.

The selection of the parameter $\theta = 0$ leads to the alternating Schwarz algorithm. In this

algorithm the continuum solution provides boundary conditions for the molecular dynamic simulation which returns the boundary condition for the next continuum iteration. The convergence of this iterative process is determined by the matching of the continuum and molecular solution in the overlapping region.

The alternating Schwarz method is a serial technique which has been used to couple the continuum description not only with molecular dynamics but also with direct simulation Monte Carlo simulations. Generally, its efficiency and accuracy vary significantly with the domain size and there is a strong possibility that a large disparity in the domain sizes can cause divergence in the solution. The dependency on the domain can be minimised when appropriately selected values for the parameter $\theta \neq 0$ are used. Furthermore, the convergence of the overall procedure can be affected by the compatibility between the macroscopic and microscopic transport coefficients. Hence, the techniques used to apply the continuum state to the molecular region have a great impact on the quality of the solution.

In the majority of the studies when the Schwarz method is employed, a particle reservoir is utilised to ensure the mass continuity across the HSI. In addition periodic boundary conditions are imposed aiming to prevent particles from drifting away from the particle region. If the nature of the problem prohibits the use of periodic boundary conditions then it is essential to impose a mechanism that handles the particles insertions or the extractions like the USHER algorithm described previously. The continuum velocity and temperature are usually applied through velocity distribution functions, for example, the Maxwell-Boltzmann.

The Maxwell-Boltzmann velocity distribution is the natural velocity distribution of an atomic or molecular system in an equilibrium state. It defines the probability of the one-dimensional velocity components of an atom being in a specific range, based on the temperature T and the atom mass m_i. For the Maxwell-Boltzmann distribution the probability density $f(\boldsymbol{C})$ of the thermal velocity $\boldsymbol{C} = \boldsymbol{u}/\left(2k_BT/m\right)^{1/2}$ is given by

$$f(\boldsymbol{C}) = \frac{1}{\pi^{3/2}} exp\left(-\boldsymbol{C}\right), \tag{2.4.27}$$

where k_B denotes Boltzmann's constant.

2.4.3 Time Coupling

The time evolution procedure is an important problem in the geometrical coupling and primarily in flux imposing methods. The timescales are decoupled and it is necessary to determine points in time at which the two domains should exchange their flux information. Generally, there are three different time steps involved in the hybrid procedures:

- Δt_{MD} is the time step for the molecular domain.
- Δt_C is the time step used for the continuum solver. It is several order of magnitudes greater than the molecular time step $\Delta t_C \gg \Delta t_{MD}$.
- Δt_{AV} is the time interval between two information exchange points.

The merging between the molecular and continuum time evolution can be achieved either sequentially or concurrently. The majority of studies of the flux based techniques deal with one way coupling simulations, from continuum to molecular, and therefore the strengths and weaknesses of different time coupling approaches for a fully coupled system are not yet fully explored.

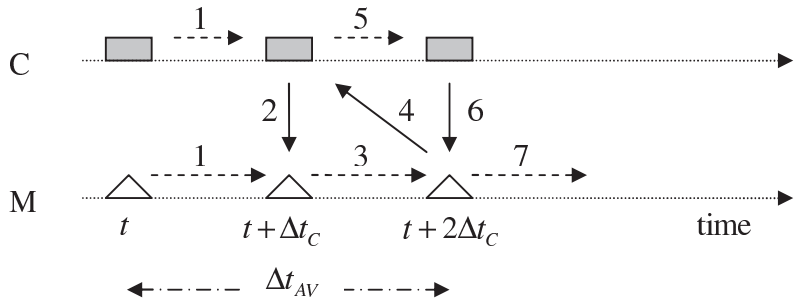

(a) Sequential time Coupling

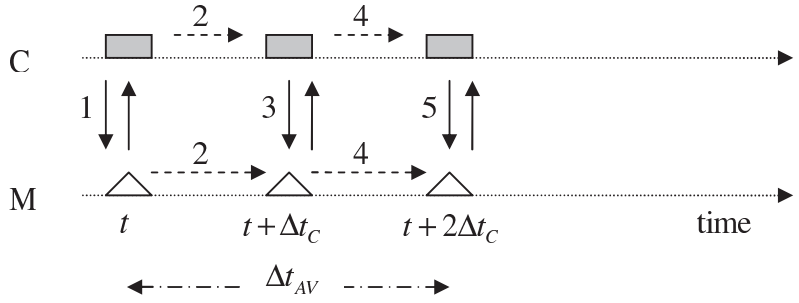

(b) Concurrent time coupling

Figure 2.5: Time matching in geometrical coupling

In the sequential implementation, shown in Figure 2.5(a), of the time coupling both descriptions are integrated from the current time t to $t + \Delta t_C$ where the continuum information is provided to molecular domain. The continuum solver is frozen at this point and the molecular one continues its time evolution to $t + 2\Delta t_C$, with continuum data applied as boundary conditions. The microscopic information is averaged over $\Delta t_{AV} = 2 \cdot \Delta t_C$ and fed back to the continuum solver. The molecular description is now frozen and the continuum is advanced to $t + 2\Delta t_C$ where the continuum information is transferred to the molecular domain and the procedure is repeated. The sequential nature of this time integration type

makes it more suitable for serial code implementation since the two descriptions are not running simultaneously.

In the concurrent implementation, shown in Figure 2.5(b), both solvers are running simultaneously and exchange information at specific points in time. This time coupling approach introduces a delay at the order of $O(\Delta t_{AV}/2)$ in the continuum description. This is due to the averaged nature of molecular information transferred to the continuum solver which refers to the mean of the time averaging interval rather than the current time. The concurrent nature of this time integration type makes it more suitable for parallel code implementation.

2.5 Numerical tools

2.5.1 Neural Networks

The development of neural networks (NN), originated 50 years ago, was motivated by a desire to understand and mimic the human brain and intelligence. Specifically, neural networks were firstly introduced in 1943 by McCulloch and Pitts [103]. McCulloch and Pitts presented simplified neurons as models of biological neurons and as conceptual components for circuits capable of performing computational tasks [104].

The interest in neural networks has emerged due to a combination of reasons. Initially, a number of theoretical results led to techniques of training more sophisticated network architectures and along with the hardware and computational power developments neural networks simulations were made more feasible.

Neural networks have experienced applications in a number of disciplines across the board of science and engineering such as electrical engineering, signal and speech processing, medicine, pattern recognition, business and applied mathematics. Their main advantage is their ability of modelling problems where the relationships among certain variables are not explicitly known [105]. In the framework of this project neural networks are utilised in the framework of multiscale modelling and hybrid codes. To further illustrate the applicability of neural nets a number of examples in various disciplines are listed below:

- Signal Processing: The neural networks have been used for many applications in signal processing. The most common commercial application is the noise suppression in the telephone line.
- Control Systems: Neural networks have been used quite extensively in the control theory. The key properties of the neural networks in this particular area is the “memory” and “experience” that can provide to a control system according to existing data.

- Pattern Recognition: There are several problems that belong to the area of pattern recognition. One of the applications of neural networks in that area is the automatic recognition of handwritten characters. The diversity in the sizes and style is making the automatic recognition difficult problem for the classical approaches.
- Medicine: One of the most common applications of neural networks in medicine is the "Instant Physician" [105]. The main idea behind this application is to train neural networks with a large number of medical records and more particular symptoms, diagnosis and treatment. Consequently, this neural network can take as input the symptoms of one illness and according to the training data to give the most common diagnosis and treatment.
- Speech Processing: In the speech processing neural networks have been used both in speech production and in speech recognition. Especially in the difficult area of speech recognition one neural network of particular interest was developed by Kohonen and respectively is having the same name[105].
- Business: The properties and the characteristics of neural networks have been utilised in a number of business applications. Known applications of neural networks are in the mortgage assessment, in forecasting and in the stock market [105].

The neural networks are information processing systems that have certain performance characteristics in common with the biological neurons. The artificial neural networks have been developed as mathematical models based on the following assumptions:

- The processing of the information occurs in many elements called neurons.
- There are connection links for passing the signals between the neurons.
- All the connection links have a corresponding weight.
- The output is determined by an activation function which is applied at each neuron. The activation function is adding non linearity to the network.

The elements that characterise a neural network is the pattern of connection between the neurons, the method of specifying the values of the weights of the connections and the type of the activation function. The artificial neural networks were inspired from neural biology and therefore the information processing in artificial and biological neurons is having some apparent similarities.

Biological Neurons

The structure of the biological neurons presents a close analogy with the structure of the artificial neural networks. Although the structure of a biological neuron may vary upon

different species, tree types of components can be identified[106]. These components are the:

- Dendrites
- Soma
- Axon

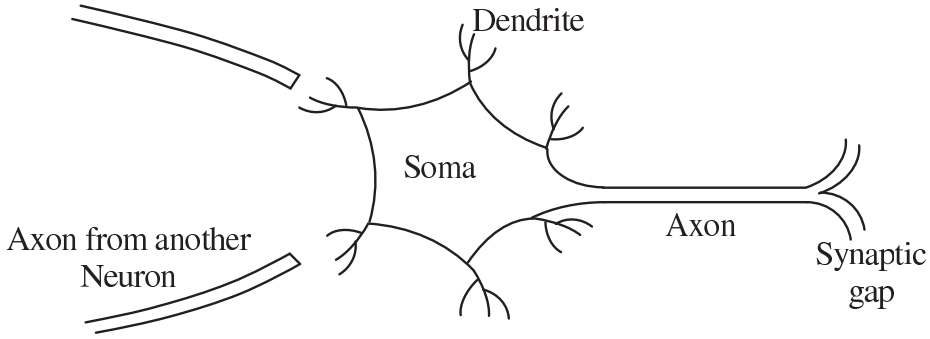

Figure 2.6: Biological Neuron

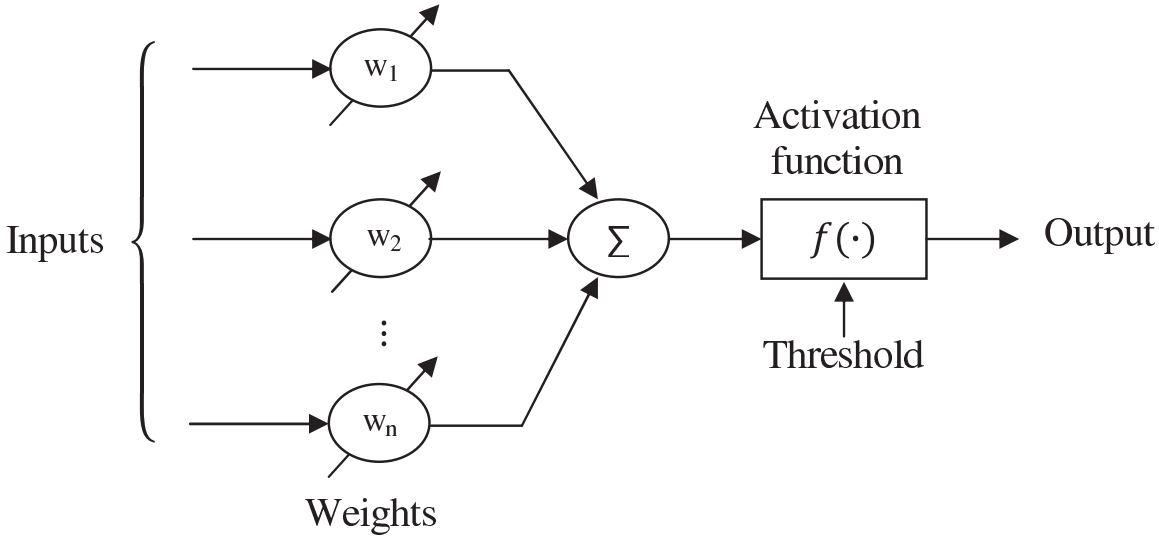

Figure 2.7: Artificial Neuron

The dendrites are the input elements of one biological neuron. They receive the signal, which is an electrical pulse, from the other neurons. These electrical pulses are transmitted by means of a chemical process across a synaptic gap. Consequently, the soma gathers and sums all the incoming signals. When the input is sufficient then the soma is transmitting the signal over the axon to the other neurons(see Figure 2.5).

There are certain analogies between the biological and the artificial neurons. Specifically,the fundamental features of the artificial neurons based on the the properties of the biological neurons are [105](see Figure 2.6):

- The dendrites transfer many input signals and consequently the artificial neuron has many inputs.
- The signals are modified by a weight at the receiving synapse. In the same vein the inputs in the artificial neuron are multiplied with a corresponding weight.
- The soma gathers and sums all the inputs. Respectively, all the weighted inputs of an artificial neuron are gathered.
- The input may exceed a threshold and be transmitted or may not. This is represented by the role of the activation function.
- The output of one neuron either biological or artificial can be used as an input to other neurons.

Neural Networks Architecture

The neurons are combined each other and this combination of neurons is called neural network. More specifically, the arrangement of neurons into layers and the connection patterns between these layers is called network architecture. There are three common layers that can be identified in almost all neural networks:

- The input layer where the input signal is transmitted to the network
- The hidden layers where the signal is being processed
- The output layer which is giving the output for the respective input

The neural networks can be classified upon the number of layers they consist of. In the number of layers that one neural network has the input layer is not counted because does not perform any computations. Consequently, the number of layers can be determined by the number of interconnect links between the neurons (see Figure2.7).

Apart from their layers number, neural networks can be classified either as feedforward or recurrent(see Table 2.1). Feedforward are the neural networks which the signal flows in a forward direction from the input towards the output unit. As recurrent can be characterised the neural networks that contain closed loop units. In the scope of the current study the multilayer feedforward networks are studied.

Network Architecture	Main Application
Multilayer feed-forward	non-linear modeling, predictions of molecules activity, pattern recognition, classification, signal filtering
Recurrent Networks	sequence and time series analysis
Encoder Networks	data compression, factor analysis, feature extraction
Kohonen Self-Organizing Maps	clustering, data compression, visualization
Hopfield Networks	auto-associative recall, optimization
Adaptive Resonance theory Models (ART)	clustering, pattern recognition
Counterpropagation Networks	function approximation, prediction, pattern recognition
Radial Basis Networks	function approximation, prediction, clustering
Adaptive Fuzzy Systems	similar to ART and feed-forward Networks

Table 2.1: Neural networks classification in life sciences.

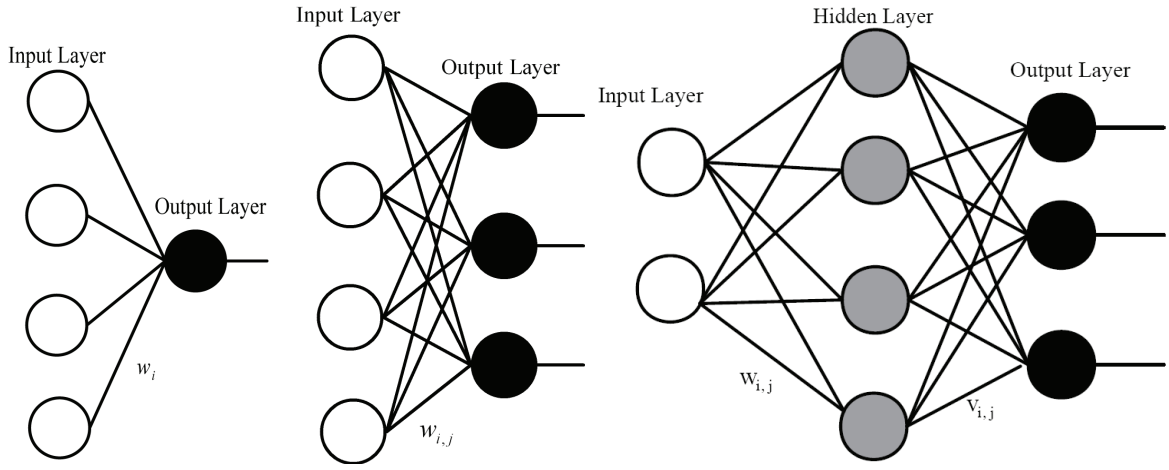

(a) Neural network with 1 input layer and 4 neurons

(b) Neural network with 4 inputs and more than 1 out- put layer puts

(c) Neural Network with 1 input, 1 hidden and 1 output layer

Figure 2.8: Types of neural network's architecture

Activation Functions

The structure of a typical neuron consists of two parts: the net function and the activation function. The net function determines how the inputs are combined inside the neuron while the activation function determines the output of the neuron.

$$u = \sum_{j=1}^{N} w_j \cdot x_j + \theta \qquad and \quad y = f(u) \tag{2.5.1}$$

The activation functions are essential parts of the neural network because they introduce non linearity to the network. Without the activation functions the neural networks are not capable of representing non linear relationships between inputs and outputs. Several types of activation functions can be identified in the literature(see Figure 2.8). The most common ones are:

- Step function:

$$f(x) = \begin{cases} 1 \; if \; x \geq \theta \\ 0 \; if \; x < \theta \end{cases} \tag{2.5.2}$$

The step function can be considered as one of the first representatives of the sigmoid functions which are extremely useful in the neural network theory. This type of functions can be trained with the back propagation algorithm however presents limitations due to the discontinuity at zero of its first derivative. In the same wider

category can be added all the functions of the type:

$$f(x) = \begin{cases} \sigma \; if \; x \geq \theta \\ -\sigma \; if \; x < \theta \end{cases} \tag{2.5.3}$$

- Identity function:

$$f(x) = x \quad for \; all \; x \tag{2.5.4}$$

This type of functions are primarily used in the last neuron in order to sum up the contributions from all the neurons and provide their linear combination. The general form of these functions is:

$$f(x) = \begin{cases} \sigma & if \; x \geq \theta_1 \\ a \cdot x + b & if \; \theta_2 < x < \theta_1 \\ -\sigma & if \; x \geq \theta_2 \end{cases} \tag{2.5.5}$$

- Logistic Sigmoid:

$$f(x) = \frac{1}{1 + e^{-\sigma \cdot x}} \tag{2.5.6}$$

and

$$f'(x) = \sigma \cdot f(x) \cdot (1 - f(x)) \tag{2.5.7}$$

The logistic sigmoid function can be scaled in order to adapt to any range of values that a given problem demands. It is most commonly used in the range of -1 to 1.

- Bipolar Sigmoid (General Hyperbolic Tangent):

$$f(x) = \frac{1 - e^{-\sigma \cdot x}}{1 + e^{-\sigma \cdot x}} \tag{2.5.8}$$

$$f'(x) = \frac{\sigma}{2} \cdot (1 + f(x)) \cdot (1 - f(x)) \tag{2.5.9}$$

The hyperbolic tangent function is taken from the above equations for value of $\sigma = 2$.

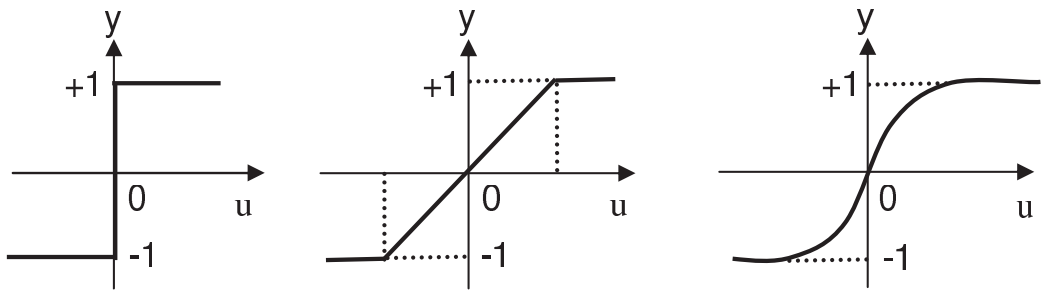

Figure 2.9: Typical activation functions: sgn, semi-linear, sigmoid

Training Procedure

The term training characterises the entire procedure that determines the values of a neural network's weights. This procedure is not unique and is crucial for the behaviour of the network. Generally two types of training can be identified, the supervised and the unsupervised.

The *supervised training* is the most commonly used process for determined a neural network's weights. In the supervised process the training is accomplished by providing training vectors as inputs and the corresponding outputs.

The *unsupervised* process is using for training the networks only the input vectors without providing any target data. The neural network in that case is trying to modify its weights in order to assign similar input vectors to the same output.

The training algorithm that is widely used for supervised training is called Back propagation. This algorithm is one of the main reasons that re-activated the interest of the scientific community for the neural networks.

Back-Propagation

The main idea behind the back propagation learning rule is that the errors for the units of the hidden layers are determined by back propagating the errors of the units of the output layer [104]. The whole concept of the back propagation is generally very clear.

Suppose a feedforward neural network with a known learning pattern. The weights of the neural networks are initialised arbitrarily. When one of those learning patterns is clamped the input values are propagated to the output and a value for the respective output is obtained. The output value is different from the desired one and an error e_o is specified for the output unit o. The goal the value for the error e_o to be equal with zero.

The most convenient way to achieve this is the greedy method. The weights of the connections of the neural network are changed in order to equalise the error e_o in this particular pattern with zero. Although this is the first step for identifying values for the weights of the neural network by itself is not enough because is not changing the weights in the input or the hidden units. The response to this problem is coming through the chain rule. The error an output unit is distributed across the hidden layers that is connected to, weighted by this connection.

Efficiency of Multi-layer Feed-forward Neural Networks

The efficiency that a neural network represents a data set is highly influenced by a number of parameters. The efficiency is counted by the error of the neural network's approximation.

The parameters with the bigger impact on the approximation error are [104]:

1. The training algorithm and the number of iteration that the algorithm performed: These parameters determine how the error is minimised to the given training set.
2. The learning samples: This is a crucial parameter for the efficient training of a neural network. It determines how representative of the actual function the training samples are. A learning sample is one set of input and output data that is used to train the neural network.
3. The number of hidden units: The number of hidden units is determined by the smoothness of the actual function. Smooth functions need only a few hidden units while widely fluctuating functions need more hidden units.

The error of approximation of the neural network can be measured in two different data sets. Initially all the training algorithms try to minimise the error between the learning set and the output of the neural network. Learning set is the set of data (learning samples) that is used for the training of the network. The average error per learning sample, named as $E_{learning}$, is defined as the learning error rate:

$$E_{learning} = \frac{1}{P_{learning}} \sum_{p=1}^{P_{learning}} E^p \tag{2.5.10}$$

where $P_{learning}$ is the number of learning sets and E^p is the error between networks data and the training data for one learning set.

Apart from the average error per learning sample the difference between the desired output and actual output of the neural network should be tested over additional data. The test set includes data that have not been used in the training procedure and are utilised to test the network's performance. Taking into account these test data it can be defined the test error rate, E_{test}:

$$E_{test} = \frac{1}{P_{test}} \sum_{p=1}^{P_{test}} E^p \tag{2.5.11}$$

The E_{test} represents the average error between the provided and the networks predictions.

The effects of the number of learning samples and the number of hidden units can easily understood by a simple example and represented by two graphs. Assume that there is a function $y = f(x)$ which has to be approximated with a feed-forward neural network. Figure 2.10 shows the error rate of a typical feed-forward network as a factor of the number of learning samples. As the number of learning samples increases the error rate for the test data increases asymptotically to a minimum value.

Figure 2.11 shows the effect of the hidden units to a typical feed-forward network. As the number of hidden layers increases the error rate at the learning set decreases towards

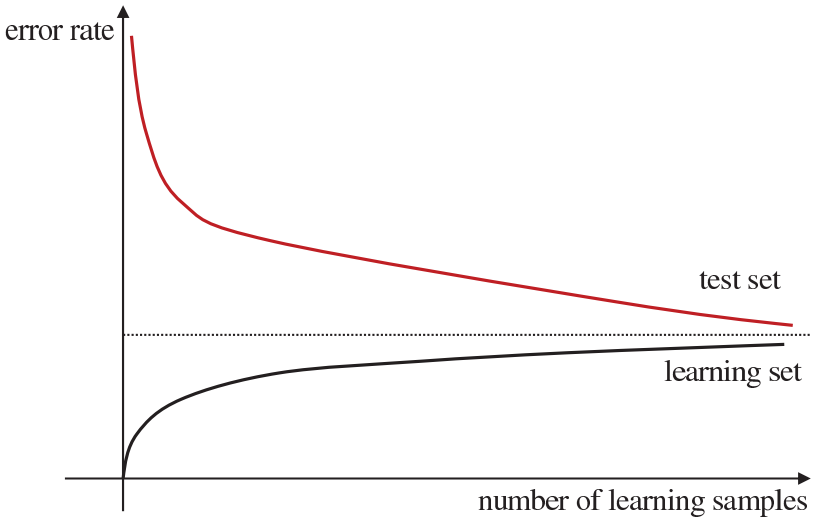

Figure 2.10: Effect of number of samples to the error rate

a minimum value. On the contrary, the error rate at the learning set although it decreases initially from one point and onwards it starts to increase. As the number of hidden layers increases fluctuations are introduced to the network's output and although the error for the learning set is reduced the lack of smoothing affects the error in the testing samples.

2.5.2 Genetic Algorithms

The genetic algorithms (GA) are search algorithms inspired from natural genetics and the mechanics of natural selection and natural genetics [107]. They are designed to simulate evolution processes of a system by utilising Darwin's principles of "survival of the fittest". In nature, individual competition for resources results in the domination of the fittest over the weaker ones. The GA were initially introduced in 1975 by John Holland at the University of Michigan [108]. Since then GA have experienced an explosion of work and their applications can be found in a variety of scientific areas such as Computer Science, Economy, Engineering, Bioinformatics, Manufacturing and many other fields. The main advantage of the GA over the conventional artificial intelligence is their robustness. Furthermore genetic algorithms offer significant benefits over traditional optimisation techniques, like linear programming, due to the fact that rarely can be led astray by local minima or maxima especially when searching in large multidimensional data.

In order to define a typical GA two things are essential: the first one is a genetic representation of the solution domain and the second one is a objective function in order to evaluate the solution. The solution domain is described as a finite length vector of variables, according to some alphabet, something that presents analogies with the DNA chromosomes. Each individual represent a point in the search domain and consequently a possible solution. A standard representation or alphabet is an array of bits 0 and 1. Hence,

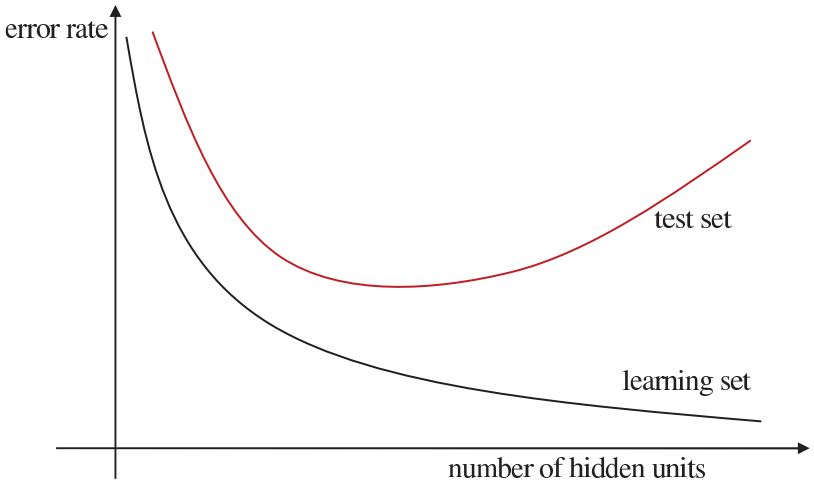

Figure 2.11: Effects of the number of hidden layers to the error rate

the individuals are linked to chromosomes and the variables to genes. Thus several genes (variables) compose a chromosome (solution). The objective function aims to measure the quality of each chromosome. The objective function is problem dependent and a fitness score is assigned to each chromosome representing its ability to "compete".

Three are the main operations of a genetic algorithm are shown in Algorithm 2.

In the scope of this study the GA are utilised to optimise the structure of the ANN involved in the PWC. This section aims to provide a quick overview of fundamental processes related to genetic algorithms.

Initialisation

In the initialisation process an initial population with possible solution is created. The generation of the initial population is random and is achieved through a generation of randomly selected $pop_{size} \cdot m$ bits, where pop_{size} is the size of the population and m is the number of bits for each individual member of the population. The size of the population remains constant throughout the operation of the genetic algorithm.

Selection

For the new population selection process a slotted roulette wheel is employed. The selection is based on the performance of each individual of the population. Higher values of the objective function or better fitness of a chromosome are translated to higher probability to be selected for the new generation.

Algorithm 2 Genetic Algorithm Pseudo code

Random initialisation population: P

Evaluation: for each i in P, compute *Objective(i)*

while !(termination_criterion)

1. **Selection:** Probabilistic selection of members of P for the new population *P_new*
2. **Crossover:** Probabilistic selection of pairs combined for crossover and probabilistic selection of the *crossover point*
3. **Mutation:** Selection of *m percent* of the member *P_new* with a uniform probability and for each one invert one randomly bit
4. **Update:** $P \leftarrow$*P_new*
5. **Evaluate:** for each $i \in P$ compute *Objective(i)*

Return i from P with the *highest objective function*

The development of a slotted roulette wheel is as follows:

1. The performance of each individual in the population is calculated according to the objective function:$Objective(i)$, $i = 1, ..., pop_{size}$
2. The total performance of the population is calculated: $F = \sum_{i=1}^{pop_{size}} Objective(i)$
3. The selection probability p_i for each member of the population is calculated: $p_i = Objective(i)/F$, $i = 1, ..., pop_{size}$
4. The cumulative probability q_i for each member of the population is calculated: $q_i = \sum_{j=1}^{i} p_j$

For the selection of the new generation the wheel is spun as many times as the size of the population and the selection is done as follows:

1. A number r is chosen randomly between 0 and 1
2. If $r < q_1$ then the first chromosome is selected. In any other case that $q_{i-1} < r < q_i$ the i^{th} chromosome is selected.

Crossover

After the selection of the new population the next operation that takes place is the crossover. A crossover probability for each chromosome in the population is considered p_c and for each chromosome in the population the process is as follows:

1. A number r is chosen randomly between 0 and 1
2. If $r < p_c$ the current chromosome is selected for crossover

The population members that have been selected for the crossover process are divided to pairs. The expected number of the chromosomes that have been selected is $p_c \cdot pop_{size}$, if the number of the selected chromosomes is odd then one more chromosome from the population is randomly selected. For each pair a random number pos between 1and $m-1$ is selected. The number pos indicates the crossover point for each particular pair. To further illustrate the process, the crossover of the following two chromosomes:

$$b_1 b_2 K b_{pos} b_{pos+1} K_1 b_m$$

$$c_1 c_2 K_2 c_{pos} c_{pos+1} K_3 c_m$$

will lead to the following pair of descendants

$$b_1 b_2 K b_{pos} c_{pos+1} K_3 c_m$$

$$c_1 c_2 K_2 c_{pos} b_{pos+1} K_1 b_m$$

The descendants will substitute their parents in the population.

Mutation

In the mutation process one gene from one chromosome of the population is randomly selected to change value. Due to the fact that the genetic algorithms that are going to be examined in the scope of this study are using bit values $0, 1$ for the chromosome the mutation will lead one chromosome to change its value from 0 to 1 and vice versa. Every gene in the population has the same probability for mutation and this is equal to p_m. The

expected number of mutations in each population is expected to be $p_m \cdot m \cdot pop_{size}$ and the process is as follows:

For each chromosome in the population and for each gene of this chromosome:

1. A random number r is chosen between 0 and 1
2. If $r < p_m$ then the value of this gene is changed

2.5.3 GA for Optimising ANN architecture

Over the last years increased attention from the scientific community has been noticed for finding the optimum architecture of a neural network [109]. The reason for that is twofold. Firstly, the architecture of one neural network is directly related with its performance and consequently necessity for optimum design is apparent. Secondly, there is no theoretical background or systematic methodology of how this architecture will be found. The traditional methods follow a trial and error process which is time consuming, is based on human expert's experience and involve high degree of uncertainty [109].

In order to confront the aforementioned problem several approaches have been proposed in the literature without concluding to a definite answer or a widely adopted methodology. These approaches can be broadly classified upon the following groups:

1. Statistical or empirical methods that are utilised to study the effects of the internal network's parameters based on performance criteria [110, 111]. The most systematic methodology in this group utilises the basic principles of the Taguchi's design in order to determine the internal parameters and meet the speed and accuracy requirements.
2. In the second group of methods the neural networks are interpreted as adaptive fuzzy systems. These methods can be characterised as fuzzy methods and their novelty is the introduction of a moving fuzzy consequent in if-then rules [112].
3. In the third group constructive or pruning algorithms are included where neurons are added or deleted from a certain architecture according some performance based criteria [113, 114]. The basic methodology for this type of algorithms is that neurons are added to the system when the training is slow or when the mean square error is above a pre-specified value. Neurons are deleted from the network when the values of the weights remain constant from a pre-specified number of training epochs or when the neurons are not having impact to the network's response. The main drawback of these methods is that they are primarily gradient based methods [109]. Their gradient nature implies that they can be trapped to local minima and consequently their convergence to global minimum is not guaranteed.

4. In the last fourth group evolutionary strategies and algorithms that search over the topology by varying the number of hidden units and layers are included [109, 115–117].

In this section a method for optimising the architecture of ANN is described. The method falls into the fourth group and is an extension of a method proposed by Bernardos and Vosniakos in [109].

Architecture Optimisation Methodology

The elements that consist the architecture of an ANN and have paramount importance for the performance of the network are:

- The training algorithm
- The number of hidden layers
- The number of neurons in each layer
- The activation function of each layer

Taking that into account, the procedure for optimising the neural network's architecture is as follows:

1. An initial population is created using a coding scheme where the number of hidden layers, number of neurons, activation function and training procedure are encoded in the chromosome. The novelty of the current approach compared to Benardos and Vosniakos [109] is the coding scheme where not only the number of hidden layers and hidden units are included but also the training algorithm and each layer's activation function.
2. By decoding the initial population's chromosomes a number of ANN is created.
3. For every ANN that is created the weights are initialised randomly and the corresponding algorithm is utilised for the training procedure.
4. The performance of every ANN is quantified according to specified criteria related with the mean square error and its complexity.
5. Based on the above objective function the evolutionary process is initiated until the GA converges or the maximum number of generations is reached.

0	1	1	1 1 0 1 0	0	0 0 0 1 1
Training	Algorithm	Activation Function		Activation Function	
		1st Hidden Layer		2nd Hidden Layer	

Table 2.2: Chromosomes Coding Example

Chromosome Coding

For the coding problem an indirect coding scheme is employed. Specifically, one ANN can be decomposed to a number of hidden layers and each hidden layer can be coded for example by using 6 bits. The number 6 is indicative since it can be increased of decreased depending on the nature of the problem. The first of the 6 bits that represents a hidden layer, indicates the activation function used. For example 0 corresponds to a linear activation function and 1 to sigmoid one. The number of bits used for the activation function can be increased if more functions have to be included. The rest of the bits represent the number of neurons of the hidden layer. For this particular example 5 bits correspond to $2^0 + 2^1 + 2^2 + 2^3 + 2^4 = 31$ neurons. Consequently, each hidden layer in this example may have either a linear or sigmoid activation function and a maximum number of 31 neurons.

The second step is to define the maximum number of hidden layers that the network will accommodate. Once the number of the hidden layers is defined then the next step towards the construction of the chromosome is to multiply the number of hidden layers with the number of bits used to code each one. For example if the maximum number of hidden layers is 2 and the bits used for each one 6 then 12 bits are needed. In order to finalise the chromosome coding 2 bits for example are engaged to represent the training algorithm that is going to be used. This results to 4 different training algorithms. However, the number of bits used can be adjusted to the nature of the problem.

Summarising for the particular example 14 bits are required in order to represent the ANN. The first two code the training algorithm and the remaining 12 are divided to 2 groups resulting 6 bits for every hidden layer. From those 6 bits the first one represents the activation function and the rest 5 number of neurons of the layer (see Table 2.2).

Objective Function - Error Criteria

The determination of the objective function for the genetic algorithm that optimises the architecture of a neural network includes the following four criteria [109]:

1. The first criterion is the training error and is used to quantify the neural network's performance in the training data set. The formula for calculating the training error is

the following:

$$E_{training} = \frac{\sum_{i=1}^{n} |(Y_{oi} - Y_i) / Y_{oi}|}{n} \tag{2.5.12}$$

where Y_{oi} are the target values, Y_i are the network's response and $E_{training}$ is the training error.

2. The second criterion is the general error for data sets that the neural network has not been trained. Usually from the amount of data available the 75% is used for the network's training and the rest 25% is used for producing the general error. The aim of this criterion is to test the performance of the network for predicting outputs for inputs that have not been used in the training. The calculation of the general error presents similarities with the calculation of the training error and it is expressed mathematically as follows:

$$E_{general} = \frac{\sum_{i=1}^{n} |(Y_{oi} - Y_i) / Y_{oi}|}{n} \tag{2.5.13}$$

where Y_{oi} are the target values, Y_i are the network's predictions and $E_{general}$ is the general error.

3. The third criterion is related with the architecture of the neural network. The general idea is that larger architectures are penalised over the smaller ones. This is due to the fact that smaller architectures present significant benefits related with the training procedure and the generalisation ability of the network. Particularly, smaller architectures accelerate the training process which is the most cost intensive part and at the same time augment the generalisation ability of the network which remains as complex as it has to be and not more. This criterion has been named from Bernardos and Vosniakos [109] as feedforward architecture criterion (FFAC) and its mathematical expression is the following:

$$FFAC = a \cdot e^{f(x)} \tag{2.5.14}$$

where $f(x)$ is a function of the total number of biases and weights and a is a constant.

4. The fourth criterion aims to penalise architecture that their predictions are not consistent throughout the solution space. Despite the fact that one architecture may exhibit low general error may have significant discrepancies is particular parts of the solution space. Consequently, it is essential to penalise the architectures that their predictions are not consistent and this is materialised through the consistency criterion (CCR) as follows:

$$CCR = 1 + 0.35 \cdot x + y \tag{2.5.15}$$

where x is the number of test cases that prediction of the network differed from 15% to 25% from the desired one and y is the number of test cases that the network's prediction differed more than 25%.

The total objective function that is formulated from the combination of the above criteria is expressed as follows:

$$Objective = FFAC \cdot CCR \cdot (E_{training} + E_{general}) \tag{2.5.16}$$

The criteria in the objective function can be easily adjusted in order to meet the needs of each particular application that is going to be applied. Lower values for the objective functions correspond to simpler neural networks with smaller and consistent error. Minimum values for the objective function are achieved when $FFAC = 1$ and $CCR = 1$.

CHAPTER 3

Point Wise Coupling

3.1 Introduction

The majority of the geometrical coupling methods are limited in terms of applicability to larger spatial and temporal scales. Particularly, these methods are constrained by (i) the size of the overlapping region that can influence the convergence of the continuum solver [23], and (ii) the integration of the molecular domain that has to be done explicitly for the whole simulated time. The scope of the current chapter is to provide a detailed description of the hybrid framework, developed in the context of the current project, named as Point Wise Coupling (PWC).

The impact of the microscopic structures and the particle interactions is modelled macroscopically through (i) transport coefficients such as viscosity or thermal conductivity; (ii) appropriate boundary conditions, such as slip velocity or tangential stress; and (iii) the constitutive relations, for example, the thermal equation of state. However, when either the microscopic structures or the particle interactions become more complicated, the continuum models break down and new models have to be derived. Typical examples are the polymeric fluids where the stress-strain rate relation is not linear and consequently the viscosity is not constant, and the gas-solid interactions where at high Knudsen numbers apparent slip is present and the no-slip boundary conditions break down.

The basic idea of the PWC is to perform MD simulations during the simulation procedure to estimate parameters needed for the continuum solver. Accurate estimation of parameters that include microscopic information will greatly enhance the accuracy of the continuum simulations. The molecular simulations are constrained by the continuum solver in order to be consistent with the local macroscopic state under the local equilibrium assumption. In the PWC coupling the entire domain is covered with the macroscopic solver and the atomistic model enters as a local refinement. Thus, the results from the microscale are embedded in the continuum simulation and in that sense PWC inherits characteristics of an embedded framework. This scheme naturally decouples the time scale between the

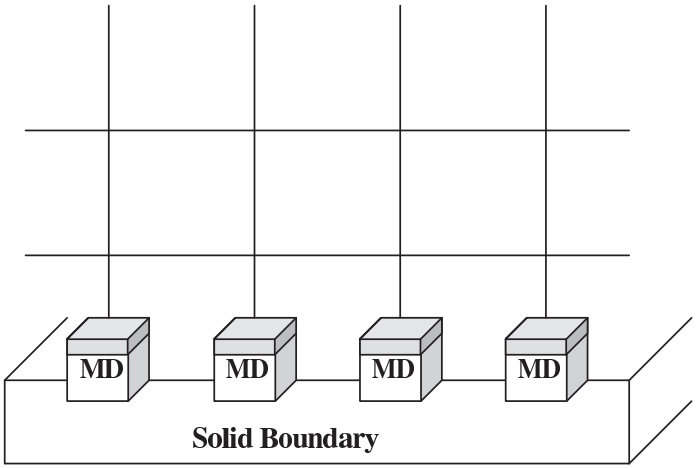

Figure 3.1: Schematic representation of a grid with the MD simulations

atomistic and continuum description.

The type of the problems that PWC is applied can be classified as follows:

Boundary condition problem: In the majority of the macroscopic simulations the no-slip hypothesis is assumed or in the cases of rarefied gases in high Knudsen numbers continuum slip models are employed. However, there are cases like the liquid flow over hydrophobic surfaces where further molecular level information is required. In this problem molecular simulations are performed around specific grid points (see, Figure 3.1), to examine the fluid behaviour in the context of fluid-solid interaction and consequently to calculate the appropriate boundary conditions. The MD simulations are constrained through the local continuum state, the slip velocities are calculated by the microscopic simulations and fed back to the continuum solver. The constrained factors for the molecular simulations and the data fed back to the continuum solver may vary depending on the nature of the problem.

Transport coefficient problem: Accurate knowledge of transport coefficients such as viscosity, thermal conductivity or accommodation coefficients can significantly improve the quality of the continuum model. When these coefficients are not explicitly known particle based methods can be directly applied in order to provide the missing data. For example in the gas slip simulations the values of the accommodation coefficients can affect significantly the amount of slip generated. However these values can be affected by local conditions and therefore there are problems where they have to be evaluated on the fly.

Constitutive relations problem: In the macroscopic simulations the constitutive relations, for example the relation between the stresses and the strain rate, can be not known explicitly. For these cases molecular simulations can be utilised to calculate the constitutive relations that are needed for the continuum solver (see Figure 3.2). The MD

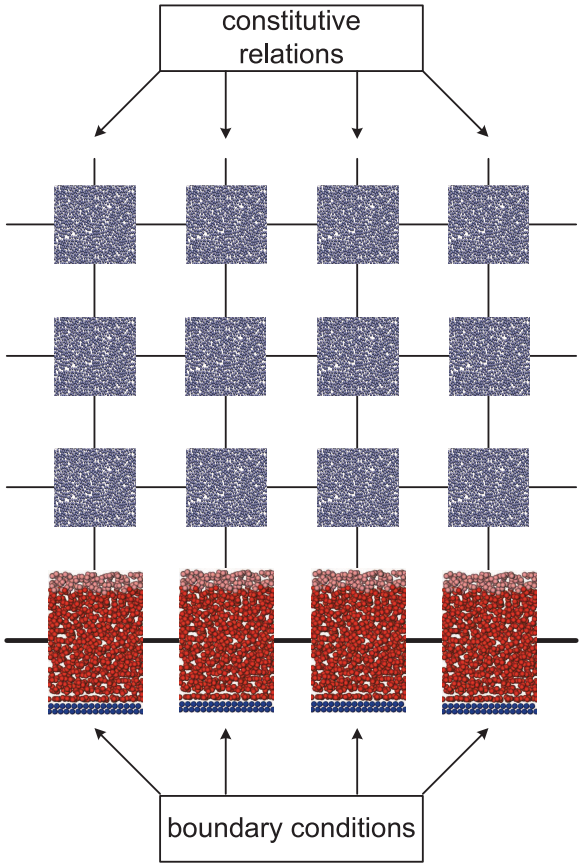

Figure 3.2: Schematic representation of a grid with the MD simulations

simulations are then performed around specific grid points, constrained through the velocity gradients, and the calculated stresses are fed back to the continuum solver.

3.2 Continuum to Molecular

The accuracy and efficiency of multiscale approaches depend to a great extent on the boundary condition transfer (BCT) method that constrains the atomistic region to the continuum conditions. The problem of imposing macroscopic conditions on a molecular system is a very challenging task and has not yet been addressed for a general case [13, 93]. The main difficulty is the disparity between degrees of freedom modelled by the atomistic and continuum models.

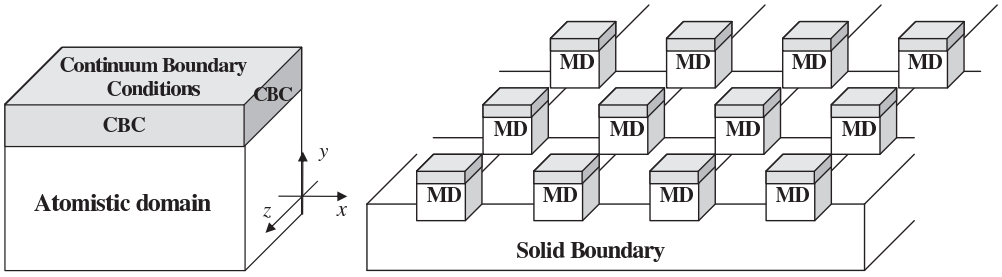

Figure 3.3: (a) Continuum state imposed on the molecular domain for the boundary conditions problem and (b) Atomistic simulations in the embedded coupling for obtaining boundary conditions

3.2.1 Boundary Condition Problem

For this type of problems MD simulations are employed in specific grid points near the walls to model molecular interactions and produce more accurate boundary conditions. The local continuum state, for example velocity, density, pressure and temperature, is applied to the microscopic simulations through the appropriate boundary conditions and then the data calculated from the molecular simulations are fed back to the continuum solver.

In Figure 3.3(a) the region where the continuum boundary conditions are transferred to the molecular model is shown in grey. In general continuum boundary conditions can be applied not only at the upper boundary but also at the other faces except the lower one that faces the solid wall. This region plays a twofold role, it ensures that the molecular simulations are consistent with the continuum state and it serves as a particle reservoir for the rest of the molecular domain (see Figure 3.3).

Enforcing the continuum constraints requires to alter the properties of the atoms inside the constrained region to match the continuum velocity, $\boldsymbol{u}_{con}$, and temperature, T_{con}. Additionally, the local continuum pressure, P_{con}, must be applied normal on the outer surface of the constrained region in order to keep the atoms within the molecular domain and to subject the molecular system to the correct pressure.

The velocity and temperature conditions can be imposed by two alternative methods. The first one is based on periodic rescaling of the atomic velocities [15, 17, 96, 99, 101, 118, 119], and the second one on a periodic re-sampling from a velocity distribution functions, such as the Maxwell-Boltzmann [25, 120, 121] or the Chapman-Enskog [21, 24, 122–125] distribution.

Rescaling techniques

The average velocity of particles in the constrained region R_{ctr} must correspond to the continuum velocity $\boldsymbol{u}_{con}$:

$$\frac{1}{M_{ctr}} \sum_{i \in R_{ctr}} m_i \boldsymbol{u}_i = \boldsymbol{u}_{con} \ , \tag{3.2.1}$$

where $M_{ctr} = \sum m_i,\ i \in R_{ctr}$ is the total mass of particles inside the constrained region. In order to satisfy Equation (3.2.1) velocities, $\boldsymbol{u}_i$ of the atoms inside the constrained region are periodically replaced by $\boldsymbol{u}_i^{'}$, which is calculated by

$$\boldsymbol{u}_i^{'} = \boldsymbol{u}_i - \frac{1}{M_{ctr}} \sum_{i \in R_{ctr}} m_i \boldsymbol{u}_i + \boldsymbol{u}_{con} \ . \tag{3.2.2}$$

Hybrid methods usually apply the normal pressure through external forces [14, 101]. The disadvantage of using an external force is that inserts/removes energy depending on the velocity of the atoms onto which the force is applied to. This results in oscillations in the molecular system [13, 16]. The oscillations can be significantly reduced by using the velocity reversing scheme [16]. According to this, the pressure, P_{con}, is applied by reversing the velocity vector of atoms that move in the opposite direction of the pressure force. If the outer surface of the constrained region is normal to a dimension α, then an atom i is reversed by changing the sign of the respective velocity component (in all the cases examined in the framework of the current thesis only the normal to the molecular boundary component of the velocity is reversed): $\boldsymbol{v}_{i,\alpha}^{'} = -\boldsymbol{v}_{i,\alpha}^{'}$. For each reversed atom, i, a momentum $p_i = 2m_i\boldsymbol{v}_{i,\alpha}^{'}$ is applied. To apply a pressure of P_{con} at each MD time step, the algorithm continues to reverse atoms until the transferred momentum equals the required momentum transfer due to the pressure:

$$\sum_i 2m_i \boldsymbol{v}_i^{'} = P_{con} \Delta t A_{ctr} \ , \tag{3.2.3}$$

where the sum is over the reversed atoms, Δt is the size of the time step and A_{ctr} is the surface area of the constrained region. The main advantages of the velocity reversing scheme are its simplicity, robustness, and the absence of any artifacts due to transfer of energy [16].

The continuum temperature is applied to the microscopic system through an energy transfer scheme [16]. The main idea is to add or remove energy from the microscopic system in order to match the macroscopic temperature without modifying the particles' mean velocity. The energy transfer is performed independently for each dimension and is achieved through scaling the velocity vectors of the atoms as follows:

$$\boldsymbol{u}_i^{'} = \boldsymbol{u}_i f + \boldsymbol{c}. \tag{3.2.4}$$

The scaling factor, f, is calculated by

$$f = \left(1 + \frac{3N_{ctr}k_B T_{con}}{2E_{k,int}}\right), \tag{3.2.5}$$

where N_{ctr} is the number of atoms in the constrained regions, E_{k,int_a} is the internal kinetic energy of these atoms, k_B denotes the Boltzmann's constant and T_{con} is the target energy. The internal kinetic energy is given by

$$E_{k,int} = \sum_{i \in R_{ctr}} \frac{1}{2} m_i \left(\boldsymbol{u}_i - \bar{\boldsymbol{u}}\right)^2, \tag{3.2.6}$$

with $\bar{\boldsymbol{u}}$ being the mean velocity component of the constrained atoms that is calculated by $\bar{\boldsymbol{u}} = (1/M_{ctr}) \sum_{i \in R_{ctr}} m_i \boldsymbol{u}_i$. The factor $\boldsymbol{c}$ is given by

$$\boldsymbol{c} = \bar{\boldsymbol{u}}(1 - f) \tag{3.2.7}$$

and ensures that no momentum is transferred along with the energy.

Resampling techniques

The second BCT method utilises velocity distribution functions. For the scope of this study the atomistic velocities are periodically sampled either using the Maxwell-Boltzmann or the Chapman-Enskog distribution. Resampling has been previously applied by other authors in relation to the moving contact line problem [120, 121].

The Maxwell-Boltzmann velocity distribution is the natural velocity distribution of an atomic or molecular system in an equilibrium state [126]. It defines the probability of the one-dimensional velocity components of an atom assuming a specific value, based on a temperature T and the atom mass m.

For the Maxwell-Boltzmann distribution the probability density $f(\boldsymbol{C})$ of the thermal velocity $\boldsymbol{C} = \boldsymbol{u}/\left(2k_B T/m\right)^{1/2}$ is given by

$$f(\boldsymbol{C}) = \frac{1}{\pi^{3/2}} exp\left(-\boldsymbol{C}\right) \ . \tag{3.2.8}$$

Each particle in the upper region is assigned a velocity $\boldsymbol{u} = \boldsymbol{u}_{con} + \boldsymbol{u}_{maxwell}$, where $\boldsymbol{u}_{maxwell}$ is the velocity of the Maxwellian distribution and $\boldsymbol{u}_{con}$ is the macroscopic velocity. The assigned atomistic velocities in the constrained region are then defined as

$$u_{ia} = u_a^{con} + \sqrt{\frac{k_B T^{con}}{m_i}} \cdot \psi, \tag{3.2.9}$$

where ψ denotes a Gaussian distributed number $N(0,1)$ and u_a^{con} is the ath component of the continuum velocity.

In order to ensure that every particle remains inside the molecular domain a reflective plane is placed at the upper boundary of the constrained region. This is simpler than the velocity reversing scheme, but can only be applied to incompressible flows because the normal pressure is a result of the reflected atoms.

For non-equilibrium situations the Chapman-Enskog distribution is a better model and, therefore, its application for sampling the atomic velocities has also been investigated. It has been used primarily in hybrid simulations of dilute gases that employ geometrical decomposition and state coupling [21, 24, 123–125].

The Chapman-Enskog distribution is a perturbed Maxwell-Boltzmann distribution [122] with probability density given by

$$f(\boldsymbol{C}) = \Gamma(\boldsymbol{C})\,\pi^{-3/2} exp\left(-\boldsymbol{C}^2\right), \tag{3.2.10}$$

where $\Gamma(\boldsymbol{C})$ is the perturbation term given by

$$\begin{aligned}\Gamma(\boldsymbol{C}) \;=\; & 1 + \left(q_x u_x + q_y u_y + q_z u_z\right)\left(\frac{2}{5}\boldsymbol{C}^2 - 1\right) - \\ & 2\left(\tau_{x,y} C_x C_y + \tau_{x,z} C_x C_z + \tau_{y,z} C_y C_z\right) - \tau_{x,x}\left(C_x^2 - C_z^2\right) - \\ & \tau_{y,y}\left(C_y^2 - C_z^2\right),\end{aligned} \tag{3.2.11}$$

where q_a and $\tau_{a,b}$, $(a, b = x, y, z)$ denote the dimensionless heat flux and stress tensor, respectively. The atomistic velocities for the current distribution are sampled from Equation (3.2.10) through the implementation of an acceptance-rejection random velocity generator described in [122].

The novelty of PWC, apart from its boundary conditions imposing techniques, is that MD simulations, constrained from the macroscopic solver, are performed around specific grid points, using the assumption of a local equilibrium, and the data that are fed back to the continuum solver are not only stresses but also velocity or temperature boundary conditions. This approach makes PWC more flexible and concurrently minimises the instabilities that may be introduced in the continuum solver through the molecular calculation of the stresses [28].

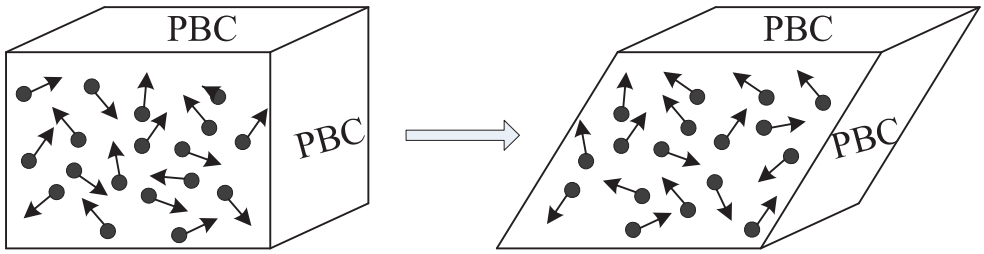

Figure 3.4: Deformation Box Procedure

3.2.2 Constitutive relations and transport coefficients

Parrinello-Rahman

Figure 3.4 shows deformation of an orthogonal box using the Parrinello-Rahman technique, when a constant shear is applied in one direction.

Consider a molecular system of N particles in a parallelepiped domain with periodic boundary conditions. The parallelepiped is defined by three vectors $\boldsymbol{a}$, $\boldsymbol{b}$ and $\boldsymbol{c}$ that span the edges of the domain. These vectors can be arranged to create a 3×3 matrix $\mathbf{H}$ where the columns are the components of $\boldsymbol{a}$, $\boldsymbol{b}$ and $\boldsymbol{c}$. The volume of the domain is given by

$$\Omega = \boldsymbol{a} \cdot (\boldsymbol{b} \times \boldsymbol{c}) \tag{3.2.12}$$

The position $\boldsymbol{r}_i$ of *ith* particle in the $(\boldsymbol{a}, \boldsymbol{b}, \boldsymbol{c})$ coordinate system is given by

$$\boldsymbol{r}_i = \mathbf{H}\boldsymbol{s}_i = \xi_i \boldsymbol{a} + \eta_i \boldsymbol{b} + \zeta_i \boldsymbol{c} \tag{3.2.13}$$

where $0 \leq \xi_i,\ \eta_i,\ \zeta_i \leq 1$.

Consider an initial reference state for the system $\mathbf{H}_0$ with a corresponding volume $\Omega_0 = ||\mathbf{H}_0||$ and a general stress applied to the molecular domain. In the reference state, any point with a coordinate vector $\boldsymbol{s}$ is transformed into the coordinate system associated with the parallelepiped:

$$\boldsymbol{r}_0 = \mathbf{H}_0 \boldsymbol{s} \tag{3.2.14}$$

With a homogeneous distortion of the system from $\mathbf{H}_0$ to $\mathbf{H}$, the position of the coordinate vector $\boldsymbol{s}$ changes from $\boldsymbol{r}_0$ to $\boldsymbol{r}$ as follows

$$\boldsymbol{r} = \mathbf{H}\boldsymbol{s} = \mathbf{H}\mathbf{H}_0^{-1}\boldsymbol{r}_0\ . \tag{3.2.15}$$

The system evolves according to the SLLOD equations of motion [127]:

$$\dot{\boldsymbol{r}}_i = \frac{\boldsymbol{p}_i}{m_i} + (\nabla \boldsymbol{u})^\tau \cdot \dot{\boldsymbol{r}}_i \tag{3.2.16}$$

$$\dot{\boldsymbol{p}}_i = \boldsymbol{f}_i - (\nabla \boldsymbol{u})^\tau \cdot \dot{\boldsymbol{p}}_i \tag{3.2.17}$$

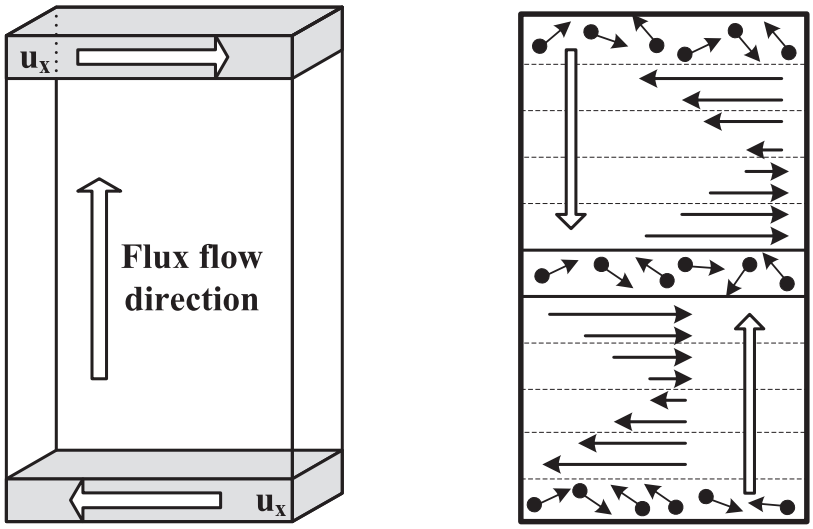

Figure 3.5: Schematic of a simulation box in RNEMD

where $\boldsymbol{p}_i$ is the momentum and $\boldsymbol{f}_i$ is the force associated with the *ith* particle.

For this type of problems the microscopic solver is constrained with the continuum strain rate and the shear stresses calculated from MD are fed back to the continuum solver. The NEMD Parrinello-Rahman method is used to perform the microscopic simulations at constant shear rate. The main advantage of this NEMD method is that it allows the application of periodic boundary conditions and therefore larger domains can be accommodated. At the same time it allows to avoid the calculation of stresses under conditions where the validity of other formulations like the Irving-Kirkwood is not justified. With the aid of the embedded methods continuum simulations can progress without considering any constitutive relations models, using averaged stresses calculated from the molecular simulations.

Reverse Non Equilibrium Molecular Dynamics

Transport coefficients can be treated as proportionality constants between a field and a corresponding flux, for example the shear viscosity correlates the shear field with the momentum flux

$$F_{p,x} = -\mu \frac{\partial u_x}{\partial y}, \tag{3.2.18}$$

where $F_{p,x}$ is the x component of the momentum flux transferred in the y direction and μ is the shear viscosity. The momentum flux $F_{p,x}$ is defined as the momentum transferred through a surface, perpendicular to the y direction, with area S over a time t.

In the RNEMD method the momentum is imposed on the molecular system artificially through a procedure that has similarities in its basic concept to the velocity reversing scheme. Specifically, in this method the simulation box is divided into N bins along the y direction, as shown in Figure 3.5, and momentum is non-physically exchanged between the

lower and the middle bin. If the atoms in lower bin are transferred along the $+x$ direction and the particles in the middle bin - along the opposite $-x$ direction, then in both areas the particles with the largest momentum in the $-x$ or $+x$ direction, for the first and middle bins respectively, are found. The momentum is exchanged between the two particles and hence a known amount of momentum Δp is transferred. This procedure is repeated for a time Δt and the total amount of momentum transferred P_{RNEMD} is calculated as the sum of the individual Δp. In the opposite direction, above the middle of the channel, there is a physical transfer of momentum arising as a response of the system to the imposed non equilibrium state [128, 129]. In a steady state, the transfer of momentum due to the physical and artificial mechanisms is the same. This can be expressed as follows

$$\frac{P_{RNEMD}}{2S\,\Delta t} = -\mu \frac{\partial u_x}{\partial y}. \tag{3.2.19}$$

From the obtained velocity profile the corresponding gradients are calculated. Then the viscosity μ is calculated from Equation (3.2.19). Apart from the velocity profile generated through the momentum exchange algorithm a temperature profile is also generated with a half period compared to the velocity one. Therefore the application of the method is not restricted only to viscosity but can also be applied to calculations of thermal conductivity and thermal diffusion [130].

Example: RNEMD Viscosity Calculation

In this example the viscosity of Lennard-Jones fluids is calculated through the RNEMD method. This procedure can be directly applied during a continuum simulation for obtaining the fluid's viscosity when it is not explicitly known. In the current example the simulation box size is 10.0585σ in the x direction, 30.1756σ in the y direction and 10.0585σ in the z direction. The fluid density is selected to be equal to $\rho = 0.81\ m\sigma^{-3}$, resulting in 2592 particles, and numerical experiments are carried out for the following three temperatures $T_1 = 0.9\epsilon k_B^{-1}$, $T_2 = 1.1\epsilon k_B^{-1}$ and $T_3 = 1.3\epsilon k_B^{-1}$. A molecular dynamics time step of 0.003τ is used and the simulations are performed for a total number of $6 \cdot 10^5$ time steps. The x momentum component is exchanged along the y direction, and the simulation domain is divided to 20 bins. An important parameter for the RNEMD scheme is the momentum exchange frequency due to its impact on the velocity distribution, large frequency can lead to non-linear velocity profiles.

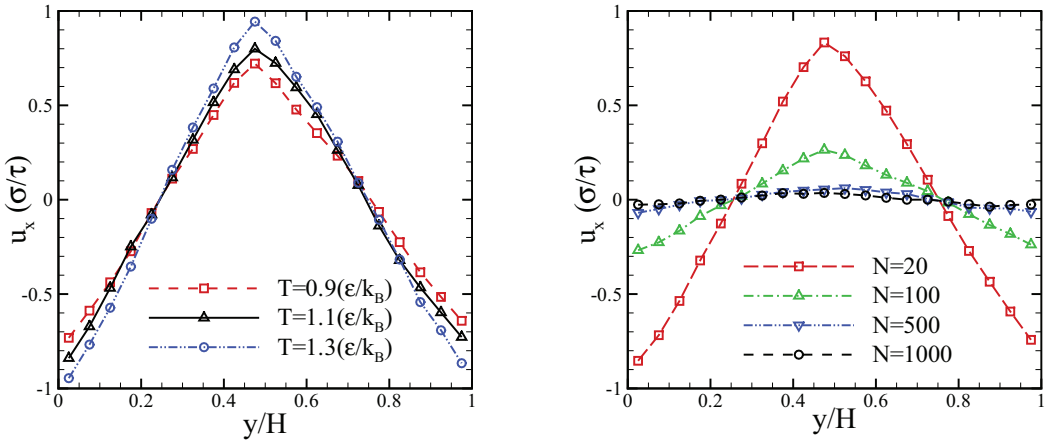

(a) Various temperatures

(b) Various momentum exchange periods

Figure 3.6: Velocity profiles obtained from RNEMD for (a) different temperatures and (b) different momentum exchange periods

Figure 3.6(a) shows the velocity profiles obtained from the simulations, with the momentum being exchanged every 20 molecular time steps. The velocity profile from $y = 0$ up to the centre of the channel $y = 0.5H$ is due to the artificial transfer of momentum between the lower and the middle bin whereas the velocity profile in the rest of the channel is a result of the momentum transfer due to the physical mechanism of friction. Hence, knowing the total momentum P_{RNEMD} that has been exchanged, the area S, the total simulation time Δt and the velocity gradient from the corresponding profiles in Figure 3.6(a) the shear viscosity is directly calculated from Equation (3.2.19).

As has been mentioned previously, an important parameter for the accuracy of the viscosity calculations through the RNEMD is the period of the momentum transfer. As shown in Figure 3.6(b) the impact of the number of time steps on the velocity profiles is apparent. A very frequent exchange of momentum generates sharper velocity profiles, however it also introduces nonlinearities that compromise the accuracy of the calculations. On the other hand, if momentum is exchanged over a large number of time steps, smaller gradients are generated and the calculation is subject to larger statistical errors.

To summarise, during the simulation procedure the amount of momentum that is artificially exchange between the lower and the middle bin is recorded. Different momentum exchange periods will result to different amount of momentum transferred and therefore to different velocity profiles and specifically different velocity gradients, as shown in Figure 3.6. Based on (i) the velocity gradient calculated from Figure 3.6 for a specific exchange period, like for example 100 time steps, and (ii) the amount of momentum transferred during the simulation P_{RNEMD} the viscosity is calculated by utilising Equation (3.2.19).

3.3 Molecular to Continuum

The transfer of information from the molecular to the continuum description, although less complicated compared to the reverse procedure, is crucial for the efficiency and accuracy of the hybrid scheme. In atomistic simulations the calculation of macroscopic variables is performed through averaging the corresponding microscopic properties. Thus, the information transferred to the continuum description is subject to fluctuations in space and time. The fluctuations introduced can affect the stability and convergence of the continuum solver; however this is a problem that primarily arises in the geometrical decomposition approach. For PWC the fluctuations can be reduced simply by increasing the number of atoms and/or the number of time steps from which the respective quantity is calculated. This is achieved by increasing the volume of the cell and the overall simulation time for which the calculations are performed. This is possible through the decoupled time and length scales in the PWC.

3.3.1 Linear Optimisation

In the first implementation of PWC molecular simulations were performed at every time step of the continuum solver. The macroscopic quantities of interest were measured from the MD simulations and fed back to the CFD solver, where they were used to advance the solution forward in time. This basic procedure leads to repetitive MD simulations of nearly identical states and, thus, a more sophisticated algorithm that utilises already performed MD simulations is employed. For simplicity consider an example, where the MD simulation of the flow at the boundary have to be performed for specified density, ρ_{con}, and velocity, u_{con}. The slip velocity as function of ρ_{con} and u_{con}, i.e. $u_{slip}()$, is fed back to the continuum solver. Instead of performing atomistic simulations for every data set required by the continuum solver, the macroscopic variables are discretised based on an initial value, u_{in}, ρ_{in}, and an interval, δu, $\delta\rho$. Therefore, when a set of (u_{con}, ρ_{con}) is given as an input, the discrete sets $(u_{in} + m\delta u,\ \rho_{in} + n\delta\rho)$, $(u_{in} + (m+1)\,\delta u,\ \rho_{in} + n\delta\rho)$, $(u_{in} + m\delta u,\ \rho_{in} + (n+1)\,\delta\rho)$, and $(u_{in} + (m+1)\,\delta u,\ \rho_{in} + (n+1)\,\delta\rho)$ are identified, where $u_{in} + m\delta u < u_{con} < u_{in} + (m+1)\,\delta u$ and $\rho_{in} + n\delta\rho < \rho_{con} < \rho_{in} + (n+1)\,\delta\rho$ and $m, n \in \mathbb{Z}$. Molecular simulations are performed for the four data sets and through a bilinear interpolation the outcomes for the input (u_{con}, ρ_{con}) are calculated. The calculated molecular data are stored and are being utilised if another input is in the same or an adjacent interval. Therefore, as the simulation evolves the number of the performed MD simulations is minimised. Furthermore, depending on the simulation set up, the accuracy requirements and the resources available by modifying the δu, $\delta\rho$ parameters the number of total atomistic simulations will varies, larger values implies less MD simulations.

Algorithm 3 PWC: Molecular operations under Linear optimisation

STEP 1: For every continuum input x_{con} find $m \in \mathbb{Z}$ where $x_{in} + m\delta x < x_{con} < x_{in} + (m+1)\,\delta x$
STEP 2: Search in the stored data if simulations with inputs $x_{in} + m\delta x$ or $x_{in} + (m+1)\,\delta x$ have been performed
STEP 3: If one or more simulations have been previously performed, then run MD for the missing data
STEP 4: Store the atomistic data produced y^m and/or y^{m+1} in the simulation's data library
STEP 5: Based on the library data calculate the data needed from the continuum solver

3.3.2 Neural Network Optimisation

In the NN optimisation instead of predefining the input sets for the atomistic simulations through for example the parameters x_{in} and δx, are utilised to define a confidence interval around the input data. If any library data are inside this confidence interval then the output is based on the library data otherwise atomistic simulations are performed for the exact continuum input set (see Algorithm 4). For example assume a continuum input x_{in} and a parameter δx. Based on these values a library search is performed for data x_{lib} with $x_{in} - \delta x < x_{lib} < x_{in} + \delta x$. If data that fulfill the aforementioned requirements are found then the atomistic outputs are estimated based on neural networks trained with the library's information. In the event that the information transferred from the continuum is not in the library's confidence limits then MD simulations are performed, the outputs are stored in the library, the neural networks are trained to accommodate the new information and are used to provide the atomistic output.

Depending on the efficiency and accuracy requirements the δx_i parameters that determine the confidence intervals can be adapted. Smaller values implies higher number of atomistic simulations and therefore larger data availability for obtaining statistical averages and for training and testing the neural networks. On the other hand, larger values of δx suggest that fewer MD will be performed and more atomistic simulations will be substituted by neural networks contributing to the reduction of the computational workload. Another parameter that can be defined based on the problem's requirements is the acceptable minimum number of library data that should be included in inputs confidence intervals. As this number increases more atomistic simulations will be carried aiming to enhance the problem's computational accuracy.

The main advantage of the neural network optimisation procedure is its flexibility to encompass additional number of continuum input parameters, its implementation simplicity and robustness. Every data provided from the atomistic description to the continuum solver are transferred through the neural networks that act as filters that suppress the inherent fluctuations of the molecular data. The aim of the neural network optimisation is twofold (i) initially to utilise already performed data for similar states and minimise the overall computational procedure and (ii) to minimise any instabilities induced to the macroscopic description due to propagation of atomistic fluctuations towards the continuum solver

Algorithm 4 PWC: Molecular operations under Neural Network optimisation

foreach *Input parameter* $x_i,\ i = 1,\ \ldots, n$ **do**
  $i \leftarrow$ Search if $x_{i,lib} \in [x_i - \delta x_i, x_i + \delta x_i]$
  if $x_{i,lib} \notin [x_i - \delta x_i, x_i + \delta x_i]$ **then**
    1. Perform atomistic simulations for continuum inputs
    2. Store atomistic outputs to library
    3. Re-train neural networks
  end
  $\boldsymbol{Calculate}$ data needed by the continuum solver based on neural networks
end

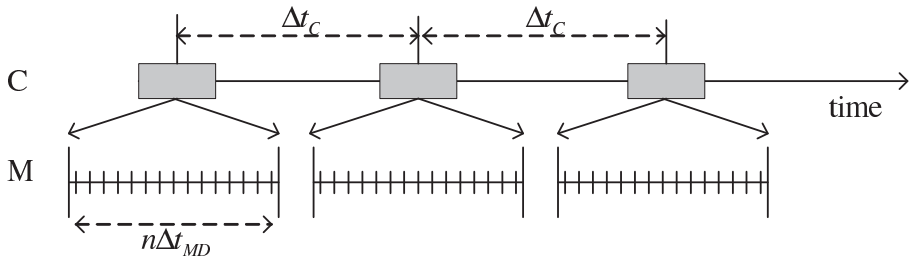

Figure 3.7: Time decoupling in the embedded based methods

3.4 Time Decoupling

The time decoupling is an important issue for all hybrid multiscale approaches. A major advantage of the PWC is that the time scales of the micro and macro solvers are naturally decoupled. Microscopic solution is obtained once per given number of time steps using macroscale solution as a constraint and used to derive missing data or unknown parameters for the macroscale simulation. Microscopic simulations are thus used as a local high resolution refinement rather than as a subset of the entire flow domain like in the geometrical coupling [25, 30, 32]. Hence, in PWC the overall time that the micro solver has to simulate can potentially be much smaller compared to that required in geometrical coupling methods and therefore these methods are more computationally attractive especially when applied to large scale problems. The time scale decoupling at PWC is shown at Figure 3.7.

CHAPTER 4

Molecular Studies

All the MD simulations in the framework of this PhD project have been performed using LAMMPS software developed by Sandia Laboratories [131]. Along the duration of this study several versions of LAMMPS have been used, however every new version was validated towards a number of fundamental test cases that are provided together with the LAMMPS code by Sandia Laboratories. However, it has to be stated that all test cases presented in this thesis have been simulated through the same version of LAMMPS that was released 21st of March 2008.

4.1 Nanoscale material modelling using Neural Networks

Nanoscience and nanotechnology have been emerging fields of research and development, and their advances are impacting on many diverse sectors, including engineering, physics, biology and medicine. Despite the impact of nanoscience and nanotechnology on a variety of products, such as medical devices, security sensors, computer hardware devices, diagnostics, and manufacturing techniques[132], nano scale developments remain time-consuming and cost-intensive processes. Numerical methods can be used to test new concepts and speed up the design process.

Molecular dynamics is a widely adopted technique for modelling and simulating materials on nano and micro scales[9, 90, 133]. The Achilles heel of MD is the computational time and computing power required, especially for fine grain simulations. For example, simulation of $1\mu s$ of pure water with fixed $O-H$ bonds and fixed $H-O-H$ angles, using a time step of $\delta t = 2\ fs$, requires 500 million time steps, corresponding approximately to 19 months simulation time[14] in a personal computer with 3 GHz CPU power. Establishing MD simulations as a practical tool in a design environment requires the development of numerical techniques that will significantly speed up the computational process.

Neural networks are versatile numerical techniques that can make MD simulations

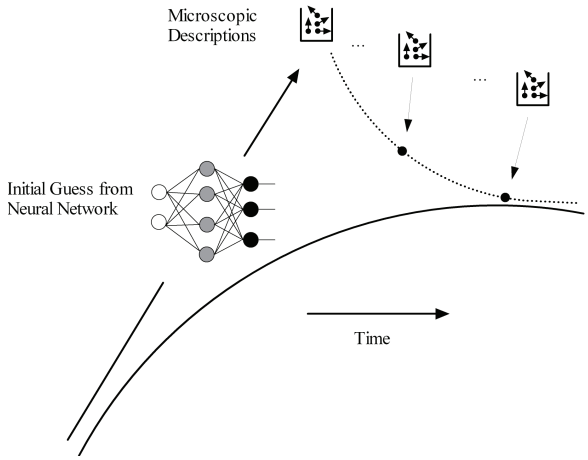

Figure 4.1: Schematic representation of neural networks used to provide an initial guess for simulations.

less computationally intensive. In the past, neural networks have been developed for diverse research problems in engineering, biology, chemistry, and medicine[134–139]. In nanosciences neural networks have been employed in nanoelectronics, drug design, gene predictions, and MEMS[133, 140–143]. Here, neural networks properties relating to nonlinear modelling, prediction accuracy, feature extraction and classification, are explored in the context of molecular simulations, aiming at advancing the applicability of MD models in micro and nano scale applications.

4.1.1 Combining neural networks and MD modelling

Neural networks are an ideal tool for comprehensive parametric analysis of multidimensional data and physical properties. They can be used either to model the co-ordinates of the simulation particle at different time steps and/or for different initial conditions, or to correlate the relationship between physical variables, e.g., temperature, with the initial conditions of the simulation. Although neural networks are not an exact approximation, they offer the best compromise between accuracy and computational cost. Moreover, neural networks can be used to provide an initial guess for MD simulations, as well as for multiscale modelling involving molecular and continuum models. A neural network can be trained using a given data set of initial microscopic conditions and averaged macroscopic data. This neural network will provide an estimate of macroscopic variables for any other data set of initial conditions. The estimated macroscopic variables are finally used to initialize and perform a microscopic simulation[144]. A schematic representation is shown in Figure 4.1.

4.1.2 Model Validation

In order to validate the applicability of neural networks in conjunction with MD simulations, a molecular system consisting of 560 molecules surrounding a cylindrical void, with a side shear applied has been employed. After performing MD simulations for this system, neural networks have been trained to predict the trajectories of the molecules for all the time steps under different shear stresses.

The crucial decisions are related to the architecture of the neural network, particularly to:

- The number of inputs;
- the number of outputs;
- the number of hidden layers;
- the number of neurons;
- the activation function;
- the training algorithm.

The neural networks that have been trained had as input the values of the shear stress, the time step and as output the co-ordinates of the particles. Consequently, in the test cases that have been implemented, the outputs of the neural networks are equal to the number of molecules of the simulation. An alternative implementation was to use the unique particle identification number as an additional input to the neural network and have as outputs only the co-ordinates x, y, z of the respective particle. This approach would complicate the neural network's architecture and it was therefore left to be investigated in future work.

After obtaining the data from the MD simulations the neural networks were trained using the back-propagation algorithm; 75% of the MD data were used for training and 25% for validation. The neural networks employed here have 1 hidden layer with 5 neurons and the *tanh* as an activation function. The neural network's structure that has been validated in this study has 2 inputs and 560 outputs.

The neural network has 560 outputs, one output for each particle of the simulation. The errors presented in this section are calculated as follows: (i) for particle the relative error regarding its x, y, and z coordinates is calculated as the $Error_{i,x} = |x_{sim} - x_{ANN}|/x_{sim}$ and (ii) the average error of all the particles is presented $\frac{1}{N}\sum Error_{i,x}$, where N is the number of particles 560 in our case.

The neural network predictions were found in very good agreement with the training data obtained by MD, with the error being of the order of 10^{-20}. Figure 4.3 shows the

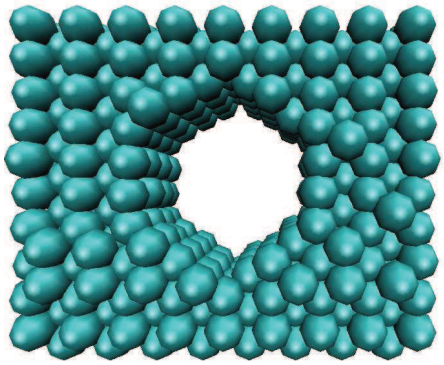

Figure 4.2: Initial simulation box.

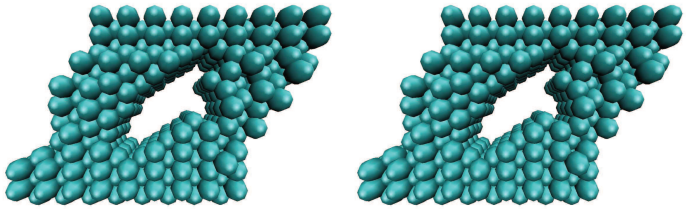

(a) Simulations Results (b) Neural networks predictions

Figure 4.3: Neural networks predictions (for trained data) against MD results (validation data)

structure of the material as predicted by MD and the neural network, respectively. The results of the neural network for the intermediate validating data with respect to the particles co-ordinates exhibited an error of the order of 10^{-4}. This error could possibly be further reduced by applying different network's architectures. Figure 4.4 shows the differences between neural network and MD results. In this case, the neural network has been trained with only two different values of shear stress and validated for the intermediate one. In the results of Figure 4.5 the training sets have been increased to five and the accuracy of the neural network for the same case has been improved.

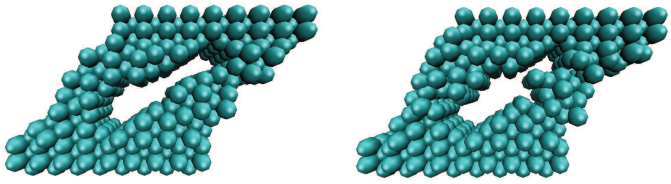

(a) Simulations Results (b) Neural networks predictions

Figure 4.4: Neural networks predictions against MD results (validation data)

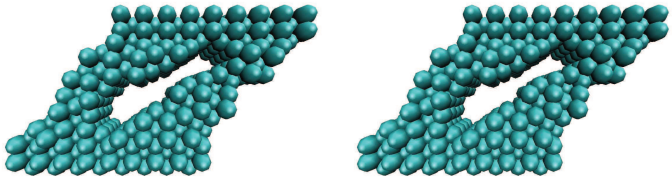

(a) Simulations Results (b) Neural Networks Predictions

Figure 4.5: Neural networks (trained with five data sets) predictions against MD results (validation data)

4.1.3 Concluding overview

This study presented an efficient utilisation of neural networks in conjunction with MD simulations. A neural networks model was implemented for a solid material with a void, subjected to shear. The neural networks predictions were found in very good agreement with the actual simulation results.

The present study shows that neural networks can be used as an efficient tool to circumvent computer resource issues associated with molecular simulations, as well as to obtain information for different sets of initial and boundary conditions. Research is under way to apply the proposed model to various applications, including design of nanofluidic sensors and dynamic friction at material interfaces.

4.2 Surface roughness effects

The phenomena observed in micro and nanofluidic systems are dominated by interfacial interactions due to their high surface-to-volume ratio[145]. The static and dynamic properties of the interface can greatly influence the flow characteristics, particularly the slip across the solid fluid interface. To quantify the slip, the slip length (L_s) is utilised, which is defined as the extrapolated distance from the wall to the point where the tangential velocity component is equal to zero ($L_s = \frac{u_{slip}}{\partial u/\partial n}$, see Fig. 4.6). Recent experimental observations [146, 147] and computational modelling indicated a number of factors such as surface energy [66], wettability [148, 149] and rate dependency[65, 66] that influence the slip length. Despite the scientific interest to the slip phenomena, the implications of the aforementioned factors to the slip's existence and magnitude are not yet fully understood [66].

Computational techniques such molecular dynamics [90, 150, 151] are employed to study the slip mechanisms and enhance our understanding in the momentum transfer across the liquid-solid interface. The majority of the computational studies [30, 88, 152–154] in

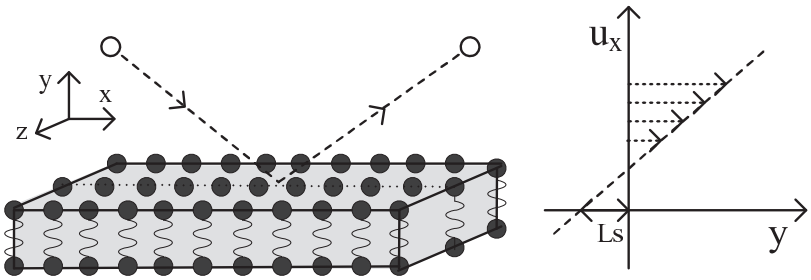

Figure 4.6: Schematic representation of the thermal wall employed along with a definition of the slip length.

the literature concentrates on the influence that the interaction potential and entropy constraints near the solid surface have on the slip generation. An equally important component for the slip process is the nanoscale surface roughness. Previous works [152] show that the presence of roughness leads to higher drag forces and, hence, to a tendency for slip elimination. The uncertainty regarding the slip's decreased rate as a factor of roughness is a research subject of crucial importance and the primary objective of the current study.

It is commonly recognised [155] that surface corrugation can greatly influence the interfacial flow characteristics. However, it is still unclear whether it contributes towards slip or stick conditions, since experimental evidence [71, 156, 157] suggests that both possibilities exist. Numerically, although a number of studies [67, 152] have been performed, the slip's decreased or increased rate as a factor of roughness, has not been fully quantified. An important component for the slip process, that may elucidate the variability of the experimental and numerical outcomes, is surface stiffness. In the current study MD simulations are employed to study the slip length's dependency on the wall stiffness for a Lennard-Jones (LJ) fluid.

In this study, the effects of nanoscale surface roughness in a channel undergoing Poiseuille flow are simulated through MD aiming at advancing our understanding of nanoscale corrugation contribution to slip generation.

4.2.1 Simulation Method

The computational domain for the present molecular simulations consists of monoatomic fluid particles confined by two rough walls separated by a distance H along the y direction. Specifically, rectangular corrugations with variable heights are simulated as shown in Figure 4.7. Periodic boundary conditions are applied in the x, z directions and the total size of the considered computational domain is 16.97σ, 34.64σ and 6.54 in the x, y and z direction, respectively.

The interatomic interactions of the wall and fluid particles are modelled by the shifted

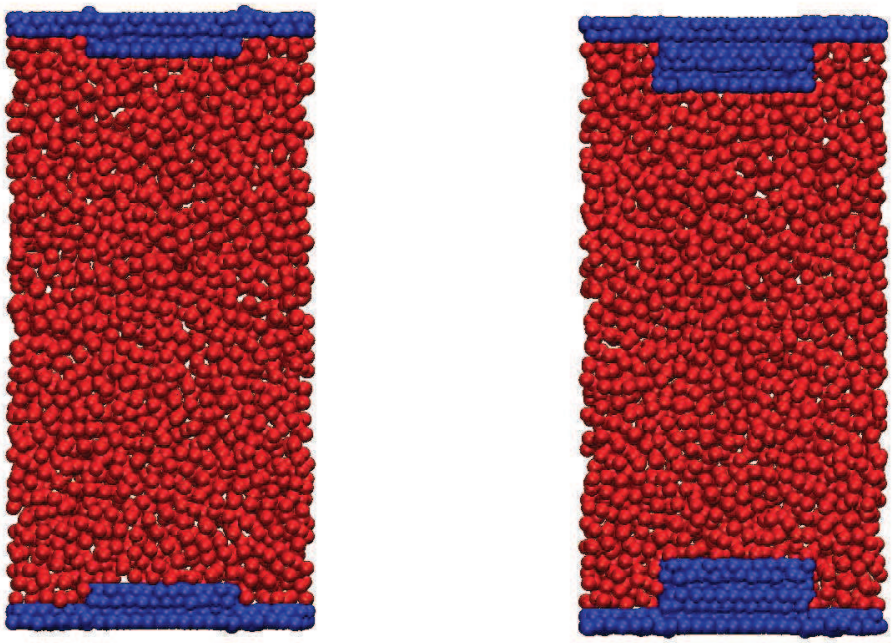

(a) Corrugation height $A = 0.86\sigma$ (b) Corrugation height $A = 2.16\sigma$

Figure 4.7: Schematic representation of a channel under the presence of nanoscale surface roughness

Lennard-Jones (LJ) potential. For a pair of atoms i and j with distance r_{ij} the potential is:

$$V_{ij}^{LJ} = 4 \cdot \epsilon \cdot \left[\left(\frac{\sigma}{r_{ij}} \right)^{12} - \left(\frac{\sigma}{r_{ij}} \right)^{6} - \left(\frac{\sigma}{r_c} \right)^{12} + \left(\frac{\sigma}{r_c} \right)^{6} \right] , \tag{4.2.1}$$

where ϵ is the characteristic energy level, σ is the molecular length scale and r_c is the cut-off distance. For the scope of this study liquid Argon particles are considered with mass m, $\epsilon = 120K/k_B$ and $\sigma = 0.34nm$ with density $\rho_f = 0.8\, m\sigma^{-3}$, cut off distance $r_c = 2.2\, \sigma$ and fluid temperature $T = 1.1\, \epsilon k_B^{-1}$.

The walls are modelled as (111) face centred cubic (fcc) planes with variable roughness height spanning from 0.43σ to 2.16σ and density $\rho_w = 4.0\, m\sigma^{-3}$. The mass of the wall and fluid particles is equal and the attachment of the wall particles to their equilibrium lattice sites is described by a non linear spring potential:

$$V_w = \frac{1}{2} k r^2 , \tag{4.2.2}$$

where k is the spring stiffness. The value specified for k should not allow the mean square displacement of the wall atoms to be larger than the Lidemann criterion of melting [66, 158] and for the current simulations a constant value $k = 600\epsilon\sigma^{-2}$ is assigned for the spring stiffness. The temperature at the solid walls is $T_w = 1.1\ \epsilon k_B^{-1}$ and is maintained through a velocity rescaling thermostat [90]. Each wall, depending on its roughness height, consists of 768 to 1800 particles for the minimum and maximum corrugation, respectively, while regarding the fluid a total number of 2640 liquid Argon particles are generated for all the simulations considered here.

The steady Poiseuille flow is imposed through an external force f_x acting on each fluid particle along the x direction. The values for the driving force is constant throughout this study and equal to $f_x = 0.02\epsilon\sigma^{-1}$. The heat exchange is controlled by a Langevin thermostat[90] with a random uncorrelated force and a friction term $\Gamma = 1.0\ \tau^{-1}$, where τ is the characteristic time $\tau = \left(m\sigma^2/\epsilon\right)^{0.5}$ [154]. The thermostat is applied only in the z direction to avoid any possible influences in the flow direction. The equations of motion for the fluid molecules are

$$m\ddot{x}_i = -\sum_{i\neq j}\frac{\partial V_{ij}}{\partial x_i} + f_x\ , \tag{4.2.3}$$

$$m\ddot{y}_i = -\sum_{i\neq j}\frac{\partial V_{ij}}{\partial y_i}\ , \tag{4.2.4}$$

$$m\ddot{z}_i + m\Gamma\dot{z}_i = -\sum_{i\neq j}\frac{\partial V_{ij}}{\partial z_i} + \eta_i\ , \tag{4.2.5}$$

where η_i is the Gaussian distributed random force with zero mean $< \eta_i(t) >= 0$ and variance $< \eta_i(0)\eta_j(t) >= 2mk_BT\Gamma\delta(t)\delta_{ij}$. The equations are integrated through a velocity-Verlet algorithm [9, 90] with a time step $\delta t = 0.001\tau$ and for a total number of $1,2\cdot 10^6$ time steps.

The interactions between the wall and the fluid are fundamental for the magnitude of slip generated at the interface. Previous MD studies have shown that the amount of momentum transfer across the interface decreases as the wall's surface energy corrugation is decreased [154]. In this study three sets of parameters for the wall-fluid interactions corresponding to different slip conditions are employed:

(1) $\epsilon_{wf} = 0.6\ \epsilon \quad \sigma_{wf} = 0.75\sigma$
(2) $\epsilon_{wf} = 0.4\ \epsilon \quad \sigma_{wf} = 0.75\sigma$
(3) $\epsilon_{wf} = 0.2\ \epsilon \quad \sigma_{wf} = 0.75\sigma$

As the strength of the wall fluid interactions ϵ_{wf} increases the slip production at the interface decreases [154]. For the present study, simulations are performed for roughness

with height 0.43σ to 2.16σ for every set of wall-fluid interactions.

From a continuum hydrodynamics perspective the wall slip boundary conditions are:

$$u_x|_{y=-h} = u_x|_{y=h} = u_{slip} \ , \tag{4.2.6}$$

where $h = H/2$ and the solution of the Navier-Stokes for the Poiseuille flow is:

$$u_x(y) = \frac{\rho f_x}{2\mu}\left(h^2 - y^2\right) + u_{slip} \ , \tag{4.2.7}$$

where μ is the fluid viscosity with values of $\mu = (2.2 \pm 0.2)\epsilon\tau\sigma^{-3}$ for the cases considered here.

4.2.2 Results and Discussion

Density Profiles

Figures 4.8-4.11 show the average density profiles under various combinations of surface roughness and wall-fluid interaction parameters. A common characteristic in all the figures is the density layering with profound oscillations near the solid walls. The fluid particles are constrained in the direction normal to the flow due to the presence of the walls and as a consequence oscillations are noticed in the density profiles. The high density layers, induced near the walls, produce other layers with smaller amplitude and these new layers further propagate the layering effect following the same mechanism. Typically, the density oscillations become weaker as the distance from the wall increases [66, 159]. For the present simulations the density rests to its bulk value after $(4 - 6)\ \sigma$. Changes in the surface attraction energy affect the layering phenomena and in particular the maximum values of the amplitude of the density oscillations. Larger values of ϵ_{wf} enhance the layering and are also correlated with larger density peak values without affecting their location. This phenomenon is noticed not only for flat walls, as shown in Figure 4.8, but also for corrugated surfaces, as shown in Figures 4.9 and 4.10.

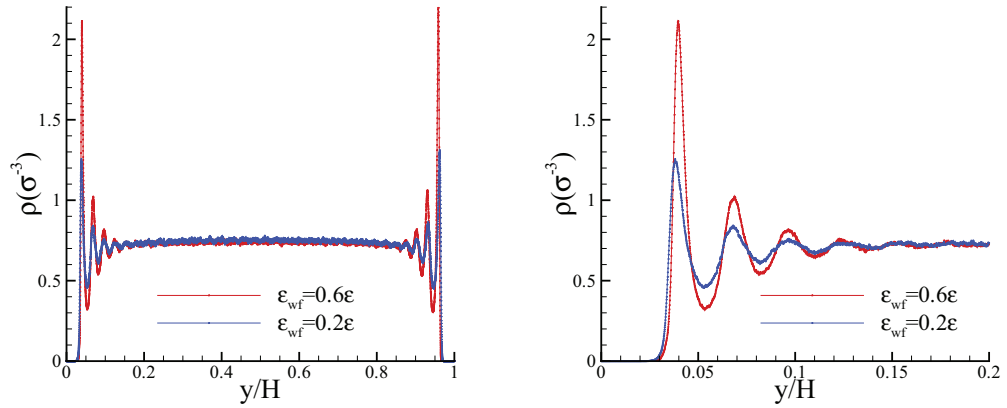

(a) Average density profile throughout the flow region (b) Average density profile near the lower wall

Figure 4.8: Density distributions for zero roughness height $A = 0.0\sigma$

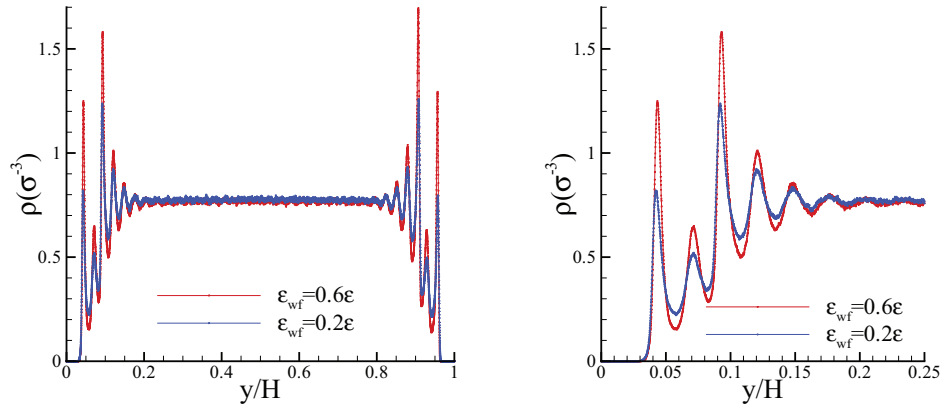

(a) Average density profile throughout the flow region (b) Average density profile near the lower wall

Figure 4.9: Density distributions for zero roughness height $A = 1.3\sigma$

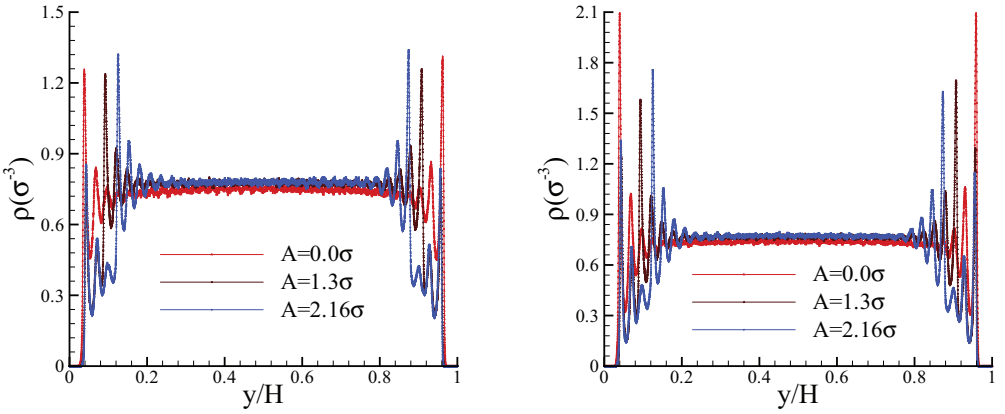

(a) Average density profile for $\epsilon_{wf} = 0.2\epsilon$ (b) Average density profiles for $\epsilon_{wf} = 0.6\epsilon$

Figure 4.11: Average density profiles for various roughness heights for $\epsilon_{wf} = 0.2\epsilon$ and $\epsilon_{wf} = 0.6\epsilon$

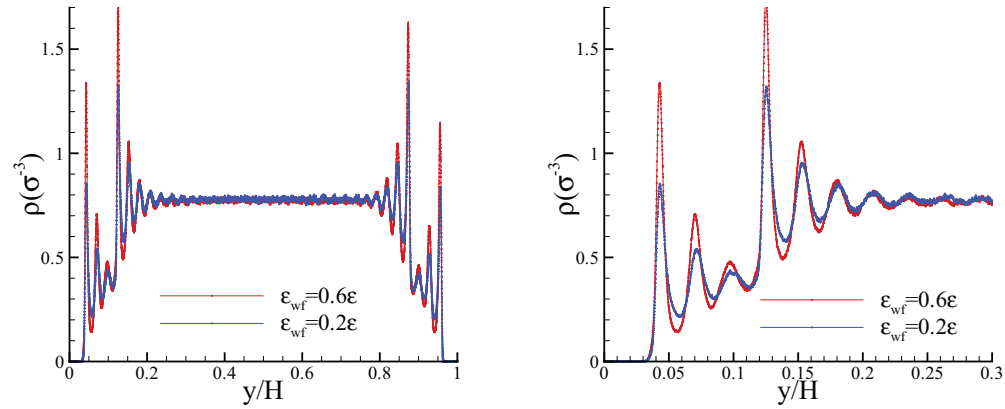

(a) Average density profile throughout the flow region (b) Average density profile near the lower wall

Figure 4.10: Density distributions for zero roughness height $A = 2.16\sigma$

Figures 4.9 and 4.10 show that the layering phenomena are enhanced through the presence of roughness. Secondary oscillations are observed at a distance equal to the height of the corrugation and are moving towards the center of the channel as the roughness amplitude increases (Figure 4.11). Therefore, an increase in the surface attraction energy ϵ_{wf}, or in the surface corrugation, will result to layering augmentation of the fluid structure and to lower slip velocities, as shown in Figure 4.12. However, the increased layering by itself is not necessarily an indicator of reduced slip and there are cases [66] where increased layering is associated with infinite slip.

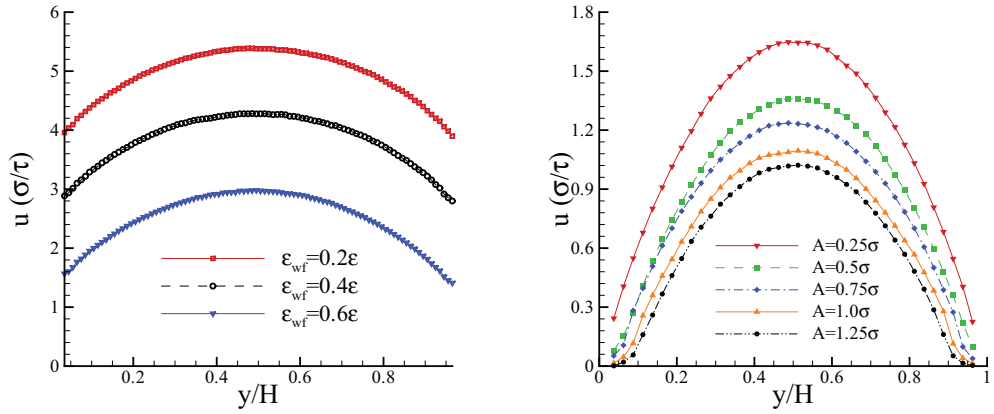

(a) Velocity profiles for various surface attraction energies without any corrugation

(b) Velocity profiles for various surface corrugations and surface attraction energy $\epsilon_{wf} = 0.6\epsilon$

Figure 4.12: Velocity profiles for various surface corrugations and surface attraction energies

Slip Velocity and slip length

Figure 4.12 shows the fluid velocity profiles under various surface roughness heights and various surface attraction energies. The velocity profile for a flat wall for three different values of $\epsilon_{wf} = 0.2\epsilon$, 0.4ϵ and 0.6ϵ (Figure 4.12(a)) shows that larger ϵ_{wf} values are correlated with smaller amount of slip. As the wall's surface energy decreases, the amount of momentum transferred at the interface also decreases, thereby leading to larger slip values[154]. In Figure 4.12(b) the velocity profiles for five corrugation amplitudes $A = (0.43 - 2.16)\ \sigma$ and for $\epsilon_{wf} = 0.6\epsilon$ are shown. The impact of the surface roughness is apparent not only at the slip velocities but also at the overall flow characteristics; for example, the maximum velocity value for corrugation $A = 0.43\sigma$ is 65% is greater than that with corrugation $A = 2.16\sigma$ and these effects are more evident for lower ϵ_{wf} values.

Figure 4.13 shows the effects of the surface attraction energy on the velocity profile under the presence of roughness with amplitudes $A = 0.43\sigma$ and $A = 2.16\sigma$. As the surface roughness increases the fluid's slip velocity tends to zero and the effects of the attraction energy on the flow characteristics is less noticeable. For flat surfaces (Figure 4.12(a)), the changes in the ϵ_{wf} values used in this study have a linear effect on the slip velocity. However, as the surface roughness is introduced in the simulations the flow characteristics and the slip velocities are affected from the surface energy ϵ_{wf} in a non-linear manner.

To provide a unified analysis regarding the effects of the roughness amplitude on the flow characteristics, the slip length is calculated for various surface properties and is plotted versus the corrugation amplitude as shown in Figure 4.14. The behaviour of the slip length suggests an exponential reduction as the roughness height increases. Regardless of the interaction parameters between the wall and the fluid particles, Figure 4.14 reveals that the

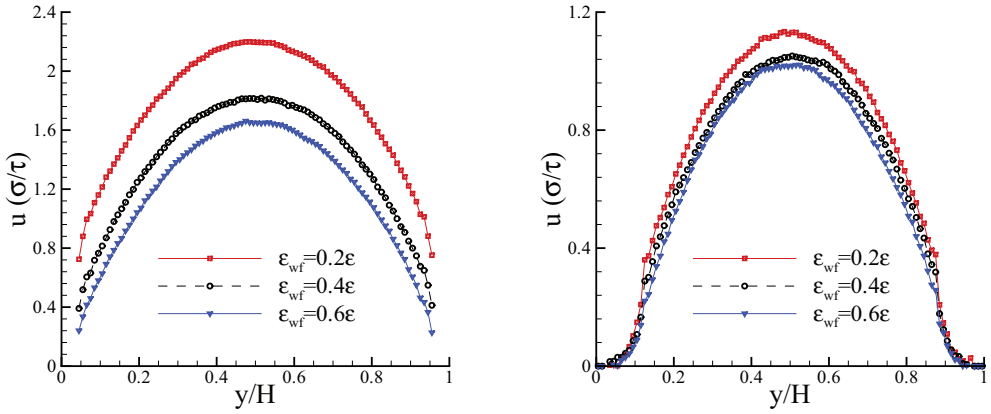

(a) Velocity profiles for various surface attraction energies and for $A = 0.43\sigma$

(b) Velocity profiles for various surface attraction energies and for $A = 2.16\sigma$

Figure 4.13: Velocity profiles for various surface attraction energies and for corrugation amplitude $A = 0.43\sigma$ and $A = 2.16\sigma$

continuum no-slip boundary condition is valid when the corrugation height is greater than 2σ. Although the slip can be affected by a number of factors such as wettability or surface attraction energy, the impact of the surface roughness on the flow becomes dominant as its amplitude increases.

4.2.3 Conclusions

In this study the effects of rectangular surface roughness with variable height and surface attraction energy on the slip generated, are investigated using molecular dynamics simulations. The numerical experiments were carried out for corrugation amplitudes and attraction energy varying from $A = 0.43\sigma$ to $A = 2.16\sigma$ and $\epsilon_{wf} = 0.2\epsilon$ to $\epsilon_{wf} = 0.6\epsilon$, respectively. As ϵ_{wf} or A increase, the density layering in the near the wall region is enhanced by higher values or secondary layering phenomena. In addition, the rectangular corrugation provides a mechanism for propagation of the fluid particles layering towards the center of the channel. The higher the corrugation amplitude is the closer to the center of the channel the density fluctuations are transferred. The velocity profiles are greatly affected by the roughness of the surface. The simulation results indicate a non-linear variation of slip as a factor of roughness amplitude. Specifically, the simulation outcomes revealed an exponential relationship between the slip length and, consequently, the slip velocity and the roughness height. However, there are still open questions regarding the mechanism that generates the slip and the factors affecting the amount of the interfacial slip produced. Future work should be carried out to further investigate the contribution of parameters, such as generalised nanoscale roughness, wettability, rate dependency and interaction parameters to the slip behaviour.

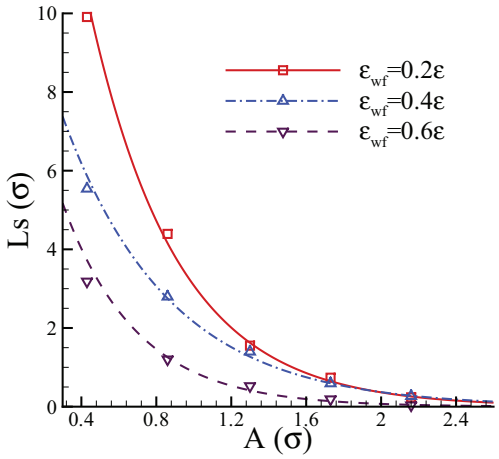

Figure 4.14: Slip length L_s against corrugation amplitude A for different surface attraction energies

4.3 Boundary slip dependency on surface stiffness

In the majority of the macroscale flows the fluid is considered to be immobile near the solid boundary; however as the scales shrink a number of experimental studies [146, 157, 160] revealed the presence of slippage. Surface structure, wettability and, nanoscale roughness are some of the factors that have been recognised to affect slippage phenomena [148, 161]. Generally, the parameters that contribute to slip generation along with their implications to the slip's magnitude are not explicitly known and fully understood [155]. Therefore, identifying and quantifying their impact poses a great challenge that will assist the development of micro and nanofluidic devices.

High fidelity computational modelling has been embraced to compliment experiments related to slippage effects, primarily due to accuracy and precision difficulties involved in measuring physical quantities at nano scales. Specifically, molecular dynamics [66, 154, 162, 163] simulations, have been employed to study the slip's mechanism and enlighten the impact of parameters such as nanoroughness or surface wettability to the slip's magnitude.

The computational domain considered for the current numerical experiments consists of monoatomic fluid particles confined by two stationary thermal walls separated by distance L_y along the y direction. The size of the computational domain is $L_x = 16.97\sigma$, $L_y = 34.64\sigma$ and $L_z = 6.53\sigma$, where σ is the molecular length scale; and periodic boundary conditions are applied in the parallel to the walls directions x and z. The interatomic interactions among the fluid molecules are modelled through a LJ potential and all the interatomic interactions are truncated at a cut-off distance $r_c = 2.2\sigma$. The fluid's density is selected to be $\rho_{fluid} = 0.81\ m\sigma^{-3}$, where m is the mass of a fluid's molecule, and corresponds to the generation of 2880 particles. A constant external force f_x, along the x direction, is applied to each fluid molecule to drive the flow. The simulations have been performed for a range

of force's values spanning from $f_x = 0.005\ \epsilon\sigma^{-1}$ to $f_x = 0.015\ \epsilon\sigma^{-1}$ with step $0.0025\ \epsilon\sigma^{-1}$. The parabolic velocity profile, described by Equation (**??**), implies that the shear rate is proportional to the applied force and consequently force's variations corresponds to subsequent adjustments of the shear rate. Previous computational studies [66, 154, 164] have indicated a non linear relationship between the shear rate and the slip length. Therefore, aiming to minimise the shear rate's influences to the outcome's variability, the impact of the wall stiffness to the slip phenomena is studied for a broad range of shear rates. The magnitude of the applied force should be cautiously selected, since high force values can drive the system out of the linear response regime [165]. The excessive viscous heating of the system is dissipated through a Langevin thermostat[154], applied only in the z direction to circumvent any possible influences to the flow direction, with fluid's temperature being $T = 1.1\ \epsilon k_B^{-1}$.

The friction coefficient has been selected to be $\Gamma = 1.0\ \tau^{-1}$ throughout the simulations, aiming to minimise any undesirable effects to the self diffusion coefficient [66, 166]. The equations of motion are integrated through a velocity-Verlet algorithm [90] with time step $\delta t = 0.001\tau$. A total number of $6 \cdot 10^5$ time steps have been performed for equilibration and afterwards another $6 \cdot 10^5$ for averaging.

Each of the solid walls is modelled as two (111) fcc lattice planes with density $\rho_{wall} = 4.0\ m\sigma^{-3}$ corresponding to 528 particles. The wall particles interact with the fluid through a LJ potential with energy and length scales ϵ_{wf} and σ_{wf} respectively. Generally, slippage phenomena are sensitive to the wall-fluid interactions and, particularly, as the wall's surface energy decreases, the amount of momentum transferred across the interface decreases leading to larger slip values [154]. Therefore, the effects of surface stiffness are studied for two sets of interfacial parameters (i) $\epsilon_{wf} = 0.2\epsilon,\ \sigma_{wf} = 0.75\sigma$ and (ii) $\epsilon_{wf} = 0.4\epsilon,\ \sigma_{wf} = 0.75\sigma$. Every wall particle i is attached to its equilibrium lattice site $\boldsymbol{r}_0$ with an elastic spring force

$$\boldsymbol{F} = -\kappa\,(\boldsymbol{r}_i - \boldsymbol{r}_0) \tag{4.3.1}$$

where κ is the wall's stiffness. Stiffness is a pivotal parameter that provides a link between the wall model and real materials and determines the wall's physical properties. Its values reveal the strength of particles' bonds and larger rates are related to higher melting points and Young's modulus. Their selection should not allow (i) the mean square displacement of the wall atoms to be larger than the Lidemann criterion of melting [66, 158] and (ii) the movement of the wall's atoms to be in a regime that cannot be entirely addressed in the molecular simulation's time step [66]. For the current study κ ranges from $\kappa = 100\ \epsilon\sigma^{-2}$ to $\kappa = 1200\ \epsilon\sigma^{-2}$; this interval is consistent with typical κ magnitudes employed in previous MD studies [66, 167, 168]. Although it is not straight forward to establish exact relations between simplified models, such as the one employed here for the wall, and real physical substances, the selected values of solid's stiffness corresponds to a broad range of real materials including silicon based structures, that are primarily used for microfluidic fabrications and typically their Young modulus is lower compared to the metals one [169]. The wall temperature is kept constant equal to $T_{wall} = 1.1\ \epsilon k_B^{-1}$ during the simulations through a velocity rescaling thermostat [170].

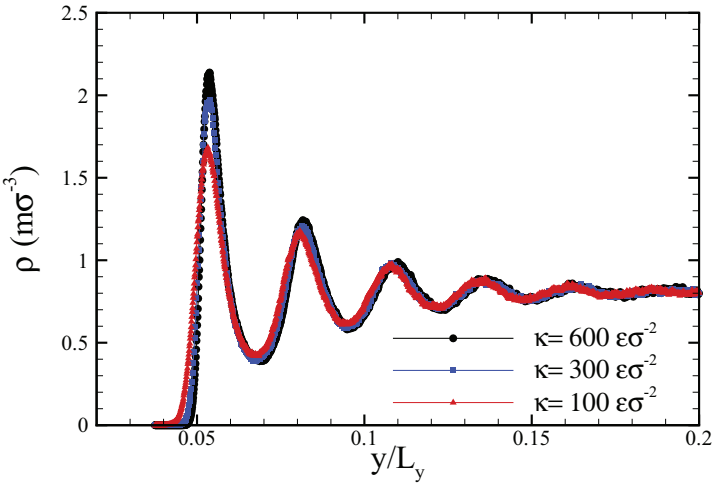

Figure 4.15: Density profiles near the lower wall for various values of the spring stiffness κ with $f_x = 0.0075\ \epsilon\sigma^{-1}$, $\epsilon_{wf} = 0.2\epsilon$.

Figure 4.15 shows examples of averaged fluid density profiles under different values of surface stiffness. These simulations have been carried out with interaction parameters $\epsilon_{wf} = 0.2\epsilon$, $\sigma_{wf} = 0.75\sigma$ and an external driving force $f_x = 0.0075\ \epsilon\sigma^{-1}$. A common element observed in the density distributions is their large oscillations near the solid wall. Despite the changes in the surface stiffness, the density follows the same pattern, since the locations of its local maxima and minima remain almost constant, and rests to its bulk value after $(5-7)\ \sigma$. The variation of the spring stiffness primarily influences the density's absolute maximum value and for the simulations considered in Fig. 4.15 this value increases, with a non linear manner, as κ increases from $\kappa = 100\ \epsilon\sigma^{-2}$ to $\kappa = 600\ \epsilon\sigma^{-2}$. Furthermore, deviations between the outcomes are reduced as higher surface stiffness rates are employed in the numerical simulations (see Fig. 4.15). Smaller κ implies that the wall particles oscillate around their equilibrium positions with higher amplitude and lower frequency and therefore the fluid molecules can potentially travel closer to the solid wall [66]. As a consequence, a broader density profile is observed near the first peak. However, as the spring stiffness κ increases its influence on the wall particles oscillations is primarily related to oscillation frequency rather than oscillation amplitude, which is mainly determined by the wall temperature [170]. Thus, its impact on the in-plane fluid's layering and hence on the density's profile is less apparent.

Figure 4.16 shows an example of the slip length as a function of surface stiffness. In the performed molecular simulations the interaction parameters are $\epsilon_{wf} = 0.4\epsilon$, $\sigma_{wf} = 0.75\sigma$ and the external driving force is $f_x = 0.01\ \epsilon\sigma^{-1}$. In Fig. 4.16 the slip length has been scaled over the parameter L_0, which represents the slip length when a fixed lattice wall is employed. In this wall model the solid particles are immobilised in their lattice sites and, therefore, are not allowed to vibrate [154, 170]. Figure 4.16 shows that the slip varies along with the surface stiffness indicating its importance to the slip process. It is visible that for

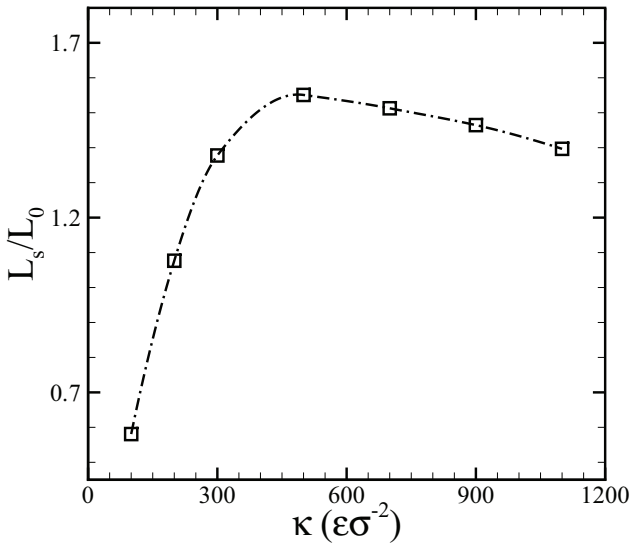

Figure 4.16: Variation of the slip length as a function of surface stiffness for a flow with $f_x = 0.01\epsilon\sigma^{-1}$, $\epsilon_{wf} = 0.4\epsilon$.

the less stiff surfaces, such as $\kappa = 100\ \epsilon\sigma^{-2}$ for the example of Fig. 4.16, the degree of slip is smaller compared to the one calculated when a fixed lattice wall is employed. Smaller values of κ imply larger displacements of the wall particles resulting to an increased surface roughness. In this case the interactions between the wall's and fluid's particles are enhanced leading to improved momentum transfer and consequently to less slippage. As κ increases the wall's surface becomes effectively smoother and higher slip is produced. However, it can be observed in Fig. 4.16 that the slip length, instead of increasing monotonically with the wall's stiffness, it obtains a maximum value $L_{s,max}$ and then starts to decline. Although stiffer walls are employed the impact of bonding stiffness to the oscillation amplitude of the walls' particles is continuously decreasing. The amplitude, as already mentioned, is primarily dictated from walls' temperature and therefore κ is no longer a dominant factor for the surface smoothness or roughness. In these cases, increasing the values of κ alters the oscillation frequency towards higher values that contribute to a more efficient interfacial momentum transfer and consequently to a reduction in the slip length.

Similar behaviour has been observed in all the performed simulations regardless the various wall-fluid interactions or shear rates employed. The results of the numerical experiments are summarised in Fig. 4.17. Here, the slip length has been scaled over the $L_{s,max}$, which represents its maximum value in a series of simulations with the same interaction parameters, driving force and variable κ. The stiffness has been scaled over the κ_{max}, which represents the value of κ that maximises the slip. It is apparent that the parameters $L_{s,max}$ and κ_{max} depend upon the various simulations conditions such as shear rate or surface attraction energy. Figure 4.17 shows that the effect of the wall's stiffness to the slip process

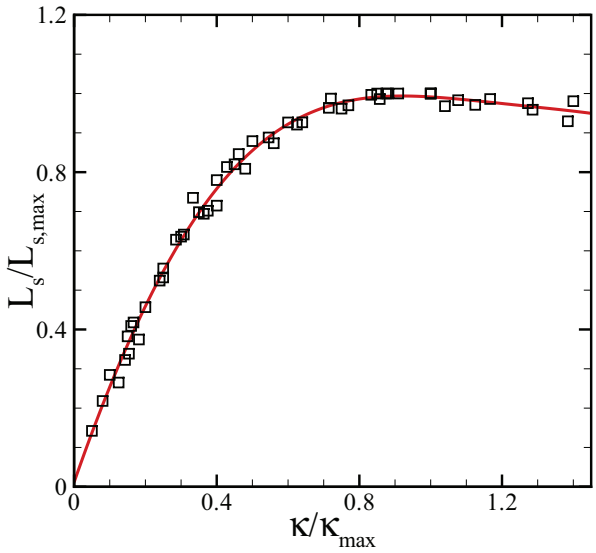

Figure 4.17: Master curve describing the variation of the slip length as a function of wall stiffness.

can be well quantified by a master curve, which in our case is a fifth order polynomial

$$\frac{L_S}{L_{S,max}} = a + b \cdot \frac{\kappa}{\kappa_{max}} + \cdots + f \cdot \left(\frac{\kappa}{\kappa_{max}}\right)^5 \tag{4.3.2}$$

where $a = 0.01$,$b = 2.59$, $c = -1.68$, $d = -0.77$, $e = 1.16$ and $f = -0.32$. In addition, Fig. 4.17 suggests that the selection of the wall's stiffness during the molecular simulations should be made cautiously since it can lead to various slip scenarios. Potentially the master curve can be extended to accommodate the variation of $L_{s,max}$ and κ_{max} as functions of other parameters that are important to the slip process, like for example the shear rate.

In summary, this study has investigated the relationship between the wall stiffness and the slip produced. For the first time we show that the slip length variations as a function of surface stiffness can be approximated and well described through a master curve. Quantifying the dependence of L_s on κ provides a mechanism for obtaining a better insight in the slip phenomena and reducing the variability regarding the values of surface stiffness employed in molecular simulations. Generally, the stiffness factor influences not only the slip process but also the thermal equilibrium at the solid liquid interface [170]. Further studies towards a better understanding of the stiffness effects on the slip and thermal transfer phenomena are also currently being pursued.

4.4 Thermal interaction effects at nano-scales

The majority of the numerical studies are mainly focused on the effects of the wall-fluid interactions to the existence of slip velocity near the solid boundary. On the other hand, phenomena regarding the thermal transport across the solid-liquid interface have not been equally exploited. Previous works[170] revealed that the main difficulty associated with the thermal boundary conditions is related to thermal wall models employed by the molecular simulations. Realistic modelling of the solid wall is crucial for the accuracy of the numerical experiments and the primary objective of the current study.

Two are the main thermal wall models applied to MD simulations. In the first one [154, 171] the wall consists of a fixed lattice structure and interacts with the fluid through the particles' intermolecular forces. Since the wall molecules are fixed in their lattice positions a thermostat has to be applied in the fluid, to dissipate the excessive viscous heating of the system. This wall model cannot accommodate heat transfer from and to the solid boundary and therefore the thermal interactions cannot be realistically simulated. In the second wall model [66, 170] the solid particles are attached to their equilibrium lattice sites with a non linear spring potential. They are allowed to vibrate from their lattice position imitating the thermal motion, and these thermal oscillations impact the momentum transfer across the interface. The walls are operating as heat baths aiming to maintain the liquid's thermal equilibrium without the need of an additional thermostat.

In this case, different thermal wall models are utilised to simulate heat transfer problems aiming to broaden our understanding of thermal transport across solid-liquid interfaces.

4.4.1 Simulation method

The computational domain for the current molecular simulations consists of monoatomic fluid particles confined by two thermal walls separated by distance H along the y direction. Periodic boundary conditions are applied in the x, z directions and the total size of the considered computational domain is 16.97σ, 34.64σ and 6.54 in the x, y and z direction respectively.

The interatomic interactions of the wall and fluid particles are modeled by the shifted Lennard-Jones (LJ) with cut-off distance $r_c = 2.2\ \sigma$. For the scope of this study liquid Argon particles are simulated particles with mass m, $\epsilon = 120K/k_B$ and $\sigma = 0.34nm$ with density $\rho_f = 0.8\ m\sigma^{-3}$. The parameters for the wall fluid interaction are $\epsilon_{wf} = 0.2\ \epsilon$ and $\sigma_{wf} = 0.72\ \sigma$.

Each wall, consists of 528 particles and regarding the fluid a total number of 2640 liquid Argon particles are generated. The time step used in all the simulations is $\delta t = 5 \cdot 10^{-4}\tau$, where τ is the characteristic time $\tau = \left(m\sigma^2/\epsilon\right)^{0.5}$, and the simulations have been performed

for $2,5 \cdot 10^6$ time steps to reach steady state and another $2.5 \cdot 10^6$ time steps for averaging.

For the scope of the current study two wall models are examined. In both of the models the walls are modeled as (111) fcc planes and density $\rho_w = 4.0\, m\sigma^{-3}$. The mass of the wall and fluid particles is equal and the wall's particles are attached to their equilibrium lattice sites with a non linear spring potential. The value specified for the spring stiffness κ should not allow the mean square displacement of the wall atoms to be larger than the Lidemann criterion of melting [66, 158] and for the current simulations two values $\kappa = 100\epsilon\sigma^{-2}$ and $\kappa = 600\epsilon\sigma^{-2}$ are assigned for the spring stiffness. The main difference between the two models is based on the wall's thermalised procedure. In the first model a velocity rescaling thermostat [90] is applied to the solid wall whereas in the second model the thermostat is applied to every layer of the wall separately.

4.4.2 Results

The first test case is an isothermal flow where the temperature on both walls of the channel is kept constant $T_w = 1.1\ \epsilon k_B^{-1}$. Two simulations for each wall model have been carried out for the two aforementioned values of the spring stiffness $\kappa = 100,\ 600\ \epsilon\sigma^{-2}$. Figure 4.18 shows the temperature profiles. It can be identified the profiles obtained from simulations based on the 1^{st} wall model, are not physically realistic and consistent. In the current test case the temperature of the fluid along the channel is expected to remain constant and equal to the walls' temperature. In the case where the 1^{st} wall model is applied, although the fluid's temperature remains constant, its value presents significant deviations from the one of the walls. In additions major differences are also observed for the different values of the spring stiffness. For the 2^{nd} wall model, as shown in Figure 4.18, the temperature profiles, from both values of the bond stiffness, remain constant and very close to the temperature value of the walls. The motion of the fluid's particles is primarily experienced by the solid molecules that belong to the first wall layer. As a consequence, the first solid layer has higher thermal velocity and higher temperature compared the averaged wall's values. Therefore, each of the layers has to be thermalised independently, to avoid any artifacts induced in the thermal transport.

In the second test case a temperature difference is applied between the walls and specifically the temperature for the lower and upper one is $T_{w,lower} = 1.1\ \epsilon k_B^{-1}$ and $T_{w,upper} = 1.3\ \epsilon k_B^{-1}$ respectively. Figure 4.19(a) shows the temperature distributions obtained when the 1^{st} wall model has been engaged. The outcomes are not physically correct since the temperature remains constant, despite the temperature difference that is applied between the walls, and in the case of spring stiffness $\kappa = 600\ \epsilon\sigma^{-2}$ is outside the applied temperature regime. Figure 4.19(b) shows the results obtained when the 2^{nd} wall model has been employed. The expected linear profile [170] is obtained. In addition a temperature jump is observed in the liquid solid interface. This jump can be quantified through the thermal (Kapitza) resistance and it varies with the spring stiffness. As shown in Figure 4.19(b) the temperature jump is higher for stiffness $\kappa = 600\ \epsilon\sigma^{-2}$.

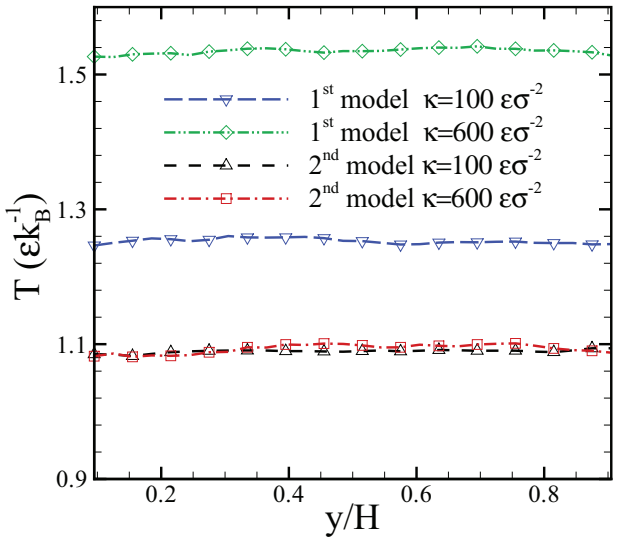

Figure 4.18: Temperature profiles for the examined wall models with various spring stiffness, when the same temperature is applied to both walls

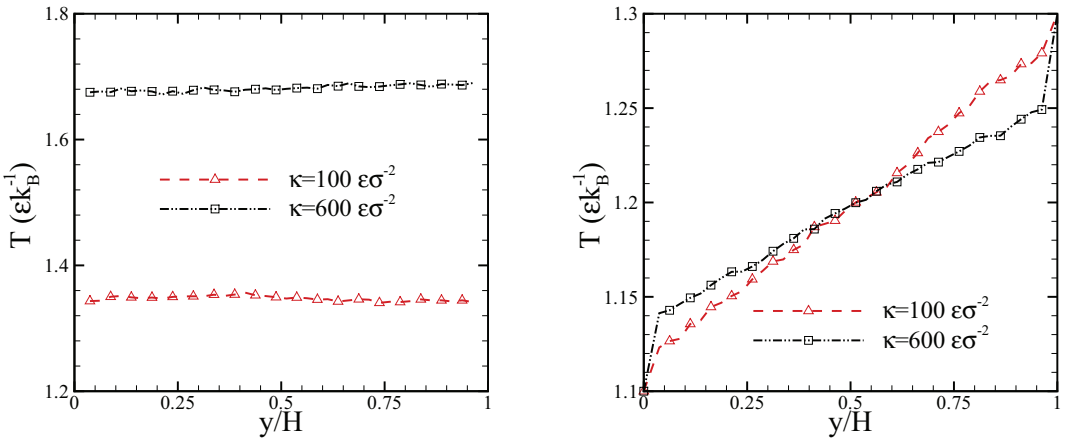

(a) Temperature profile when the 1^{st}wall model with various spring stiffness applied

(b) Temperature profile when the 2^{nd}wall model with various spring stiffness applied

Figure 4.19: Temperature profiles for the examined wall models with various spring stiffness, when a temperature gradient is applied to the channel's walls

4.4.3 Conclusions

An investigation of the different thermal wall models employed to molecular simulations has been presented. Two wall types have been examined for two fundamental heat transfer test cases. In both models the solid particles are attached to their equilibrium positions with a spring potential, and they are allowed to vibrate aiming to mimic the thermal oscillations. The main difference in the two approaches remains in the thermalisation process. The numerical experiments revealed that a thermostat has to be applied in every solid layer separately in order to represent realistically the thermal transport. Furthermore, the simulations showed a temperature jump in the solid liquid interface which is related also to the value of the bond stiffness of the wall.

4.5 Gas slip flow in a microchannel

A gas flow problem inside a microchannel is a typical example where the atomistic simulations can greatly enhance the accuracy of the continuum models. Specifically, the aim of the current example is to underline the potential benefits of embedded hybrid methods even in cases where macroscopic models exist.

4.5.1 Tangential Accommodation Coefficient

In this example an essential parameter of the continuum slip models, the momentum accommodation coefficient, is determined from first principles. The tangential momentum accommodation coefficient (TMAC) is defined as

$$\sigma_u = \frac{\tau_i - \tau_\tau}{\tau_i - \tau_{wall}}, \tag{4.5.1}$$

where τ_i represents the tangential momentum of incoming molecules, τ_τ is the tangential momentum of reflected molecules and τ_{wall} is the tangential momentum of remitted molecules. The limiting cases $\sigma_u = 0$ and $\sigma_u = 1$ correspond to specular and diffusive reflection respectively.

The momentum accommodation coefficient depends on the interaction between the wall and the gas, the temperature of the wall, local pressure and the mean direction of the flow. The accommodation co-efficient is a very important factor which has to be defined correctly since small variations of that co-efficient have a great impact on the total amount of slip due to the factor $\frac{2-\sigma_u}{\sigma_u}$ that arises in slip models.

The TMAC is sensitive to a number of parameters for example surface materials, surface roughness and gas species. In order to investigate the effect of the aforementioned

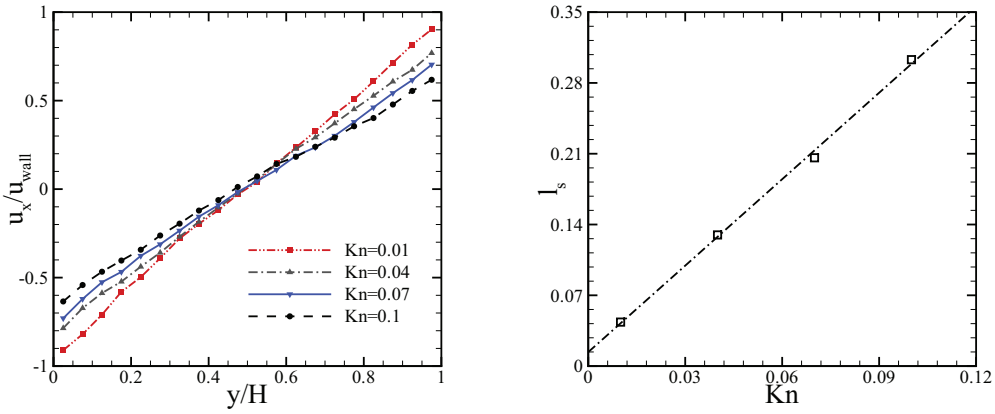

Figure 4.20: (a) Couette flow velocity profiles at various Kn numbers and $T = 1.0\epsilon/k_B$ (b) Variation of the dimensional slip length with the Knudsen number

parameters on the TMAC and gain a better understanding of the physical processes involved, MD simulations have been employed in a number of studies [68, 172–177]. In this example MD simulations are utilised in order to specify the TMAC for a specific solid-gas combination at constant temperature. The problem considered is a Couette flow of Argon between two solid Platinum surfaces. The microchannel has a characteristic length $H = 7 \cdot 10^{-2} \mu m$ and the wall is modelled as two (111) fcc planes with fixed relative positions in space. Several alternative wall schemes have been proposed in the literature [68, 170] however the choice of the wall model presented is more appropriate because of the large density difference between the gas, while at the same time it leads to significant reduction in the computational cost in comparison with more complicated models.

The particle interactions are modelled through a Lennard-Jones 6-12 potential with the following parameters $\epsilon_{Ar-Ar} = 1.67 \cdot 10^{-21} J$, $\sigma_{Ar-Ar} = 3.405 \cdot 10^{-10} m$, $\epsilon_{Pt-Ar} = 0.894 \cdot 10^{-21} J$ and $\sigma_{Pt-Ar} = 0.894 \cdot 10^{-10} m$ [172]. The equations of motion were integrated using the velocity Verlet algorithm with time step of 0.005τ where $\tau = 2.15 ps$ is the characteristic time. The temperature is controlled through a Langevin thermostat applied in the y direction.

The simulations are performed in a constant $200\sigma \times 200\sigma$ domain at four different Knudsen numbers $Kn = 0.01,\ 0.04,\ 0.07,\ 0.1$ under constant temperature $T = 1.0\epsilon/k_B$. The Knudsen number is controlled by varying the gas density according to the relation

$$\rho = \left(\sqrt{2} \pi Kn\, \sigma^2 L \right)^{-1} . \tag{4.5.2}$$

The two walls are moving with opposite velocities $U_{wall} = \pm 0.5 \sigma_{Ar}/\tau$ and the simulations run for $\sim 4 \cdot 10^6$ time steps. The steady state velocity profiles, shown in Figure 4.20, are obtained by dividing the simulation domain in bins in the y direction.

The obtained velocity profiles are linear in the middle of the channel and in the region near the wall the velocity slip is apparent. The velocity gradient increases in the region close to the wall due to rarefaction effects which is consistent with the predictions of the kinetic theory [172] and Monte Carlo simulations [178]. From the velocity profiles the slip is quantified through the dimensionless slip length $ls/H = u_{slip}/(\partial u_x/\partial y)$ which is determined by fitting a straight line to the corresponding velocity profile [179]. The slip velocity u_{slip} is calculated as the difference between the wall speed and the extrapolated velocity at the wall. The relation between the slip length and the Knudsen number for the linear Couette flow profiles can be modelled as

$$l_s = \frac{2-\sigma_u}{\sigma_u} Kn, \tag{4.5.3}$$

where σ_u is the tangential momentum accommodation coefficient. From Equation (4.5.3) the TMAC is determined through the slope of the Knudsen number and dimensional slip length relation, as shown in Figure 4.20(a).

The TMAC is calculated to be 0.27 which is in good agreement with previous MD studies [172] where for the same temperature the TMAC has been calculated 0.275. The small difference in the two values is primarily due to the different integration algorithms and time step used, for integrating and averaging the atomistic variables.

4.5.2 Slip model vs MD

In the current example the Knudsen number is in the interval $0.01 < Kn < 0.1$ and consequently the flows are in the slip regime. Navier-Stokes equations with slip boundary conditions can be then applied in order to obtain an analytic solution for a plane channel. The 1st order slip boundary condition is given by (e.g. [39]):

$$u_s - u_{wall} = \frac{2-\sigma_u}{\sigma_u} \frac{1}{\rho\left(2RT_w/\pi\right)^{1/2}} \tau_s + \frac{3}{4} \frac{Pr\left(\gamma-1\right)}{\gamma \rho R T_w} \left(-q_s\right), \tag{4.5.4}$$

where q_s is the tangential component of the wall heat flux, γ is the ratio of specific heats, τ_s is the viscous stress component, u_{wall} is the reference wall velocity, σ_u is the tangential momentum accommodation coefficient and Pr is the Prandtl number defined as

$$Pr = \frac{c_p \mu}{k}. \tag{4.5.5}$$

A number of second order slip models have been proposed in the literature. In general these can take the following asymptotic series form:

$$u_s - u_{wall} = \frac{2-\sigma_u}{\sigma_u} \left[Kn \left(\frac{\partial u}{\partial n} \right)_s + \frac{Kn^2}{2} \left(\frac{\partial^2 u}{\partial n^2} \right)_s \right]. \tag{4.5.6}$$

However an alternative formulation can be used which does not include the second order derivative (e.g. [39]):

$$u_s - u_{wall} = \frac{2 - \sigma_u}{\sigma_u} \left[\frac{Kn}{1 - b \cdot Kn} \left(\frac{\partial u}{\partial n} \right)_s \right], \tag{4.5.7}$$

where b is the slip coefficient which is determined either experimentally or through molecular simulations.

In the current example molecular dynamics simulations of Poiseuille flow have been performed to study the relation between the slip velocity and the Knudsen number and essentially to validate the first and second order slip models. In these simulations the size of the channel is fixed to $H = 7 \cdot 10^{-2} \mu m$, the wall is modelled by Platinum molecules with fixed lattice positions and the flow of gaseous Argon is computed. The Poiseuille flow is forced by an external gravitational field $g_x = 3.7\ 10^{11} m/s^2$ applied to the gas molecules. The interaction between the gas and solid molecules is modelled by the shifted Lennard-Jones (LJ) 6-12 potential with $\epsilon_{Ar-Ar} = 1.67 \cdot 10^{-21} J$, $\sigma_{Ar-Ar} = 3.405 \cdot 10^{-10} m$ and $\epsilon_{Pt-Ar} = 0.894 \cdot 10^{-21} J$ and $\sigma_{Pt-Ar} = 0.894 \cdot 10^{-10} m$ [172]. The equations of motion were integrated using velocity Verlet algorithm with time step of 0.005τ where τ is the characteristic time $\tau = 2.15 ps$. The temperature is controlled through a Langevin thermostat applied in the y direction.

The velocity profiles, normalised over the corresponding maximum velocity, for various Knudsen numbers are shown in Figure 4.21(a). The correlation of the velocity profiles can be obtained using a quadratic function:

$$u(y) = a_0 + a_1 y + a_2 y^2, \tag{4.5.8}$$

where coefficients a_0, a_1 and a_2 are based on curve fitting of the velocity profiles data. The coefficient a_0 is the non-dimensional slip velocity at the wall surface, the coefficient a_1 is the non-dimensional velocity derivative at the wall surface or the non dimensional shear rate and the coefficient a_2 is half of the non-dimensional second order velocity derivative which is linked to the forcing term.

From the data fitting the values for first and second order velocity derivatives, $\left(\frac{\partial u}{\partial y}\right)_{wall}$ and $\left(\frac{\partial^2 u}{\partial y^2}\right)_{wall}$, are calculated for the various Knudsen numbers. Figure 4.21(b) shows the relations $u_{slip} \sim Kn \left(\frac{\partial u}{\partial y}\right)$ and $u_{slip} \sim Kn \left(\frac{\partial u}{\partial y}\right) + \frac{Kn^2}{2} \left(\frac{\partial^2 u}{\partial y^2}\right)$ which correspond to first and second order slip models. In both cases the data are fitted by a least squares method and the accuracy of the fit is measured from both models through the R^2 values. For the first order model the $R^2_{1^{st}order} = 0.9978$ and for the second order $R^2_{2^{nd}order} = 0.9994$. Note, that the ideal regression is given by $R^2 = 1$. Furthermore, as expected, the least square approximation of the simulation data is more effective in the second order slip model. Even in cases where continuum models exist the above outcomes revealed that the order of the continuum models accuracy is compromised compared to the full atomistic simulations and therefore the need for embedded atomistic calculations is apparent. Furthermore the atomistic simula-

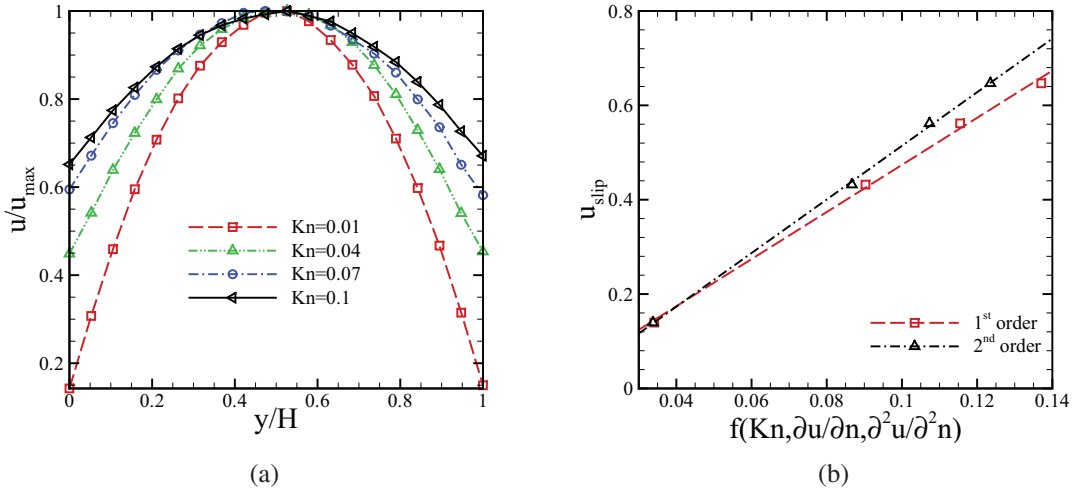

Figure 4.21: (a) Normalised velocity profiles for Poiseuille flow at various Knudsen numbers and (b) Slip velocity over $Kn\left(\frac{\partial u}{\partial y}\right)$ and $Kn\left(\frac{\partial u}{\partial y}\right)+\frac{Kn^2}{2}\left(\frac{\partial^2 u}{\partial y^2}\right)$ for the first and second slip models respectively

tions become necessary in cases where the continuum models do not exist or fail to provide accurate boundary conditions like for example gas flows over chemically patterned surfaces or over corrugated surfaces.

CHAPTER 5

Hybrid Studies

LAMMPS code is utilised to perform the molecular simulations in the hybrid test cases. The code itself is written in C++, using an object-orientated structure. This allows a relatively uncomplicated extension of additional modules into the existing code.

Several additional parts have been implemented into LAMMPS to be able to perform the hybrid simulations for this work (details regarding the methods are provided to Chapter 3):

- Maxwell Distribution: This module draws the particle velocities that belong to specific region according to a given velocity and temperature based on the Maxwell-Boltzmann distribution
- Champan Distribution: This module draws the particle velocities that belong to specific region according to a given velocity and temperature according to the Chapman-Enskog distribution
- Continuum Vel/Temp : This module rescales the particle velocities that belong to specific region to match a given velocity and temperature
- Continuum Pres : In this module the velocity reversing scheme has been implemented to apply a give pressure to molecular region

For the numerical simulations of neural networks the open source library Artificial Neural Network Library ANNIE (version 0.51) has been used. The optimisation procedure of the networks' architecture, that includes the genetic algorithms, has been implemented by the author. This code is written in C++ and has been validated for several optimisation problems of functions with known minima and maxima.

5.1 Boundary condition transfer

5.1.1 Liquid flow for the boundary problem

In this section the results of BCT schemes for liquid and gas flow and heat transfer problems are presented. The size of the molecular domain was 20σ, 50σ and 20σ in x, y and z directions, respectively. Periodic boundary conditions were applied in the x and z directions. Three regions were assigned: the wall at the bottom, the BCT region at top of the domain and the flow region in between.

The wall was modelled by two planes of a face-centred cubic lattice, where the wall molecules were allowed to vibrate around their lattice sites by a harmonic spring with stiffness $k = 50\epsilon/\sigma^2$. Their velocities were rescaled to the wall temperature $T_{wall} = 1.0\epsilon/k_B$. The density of the wall atoms was $\rho_{wall} = 1.0\ m\sigma^{-3}$ and their mass was equal to that of the fluid atoms. Here, the wall properties do not correspond to any specific solid material, but represent a solid wall with no slip boundary condition. Similar models for solid walls have been used in previous studies [70, 71, 120]. The BCT region was located at $y > 45\sigma$ and the flow region at $1.5\sigma < y < 45\sigma$. The total number of atoms was 18, 820, of which 676 formed the wall and the remaining 18, 144 the fluid within the flow and BCT regions. The fluid density was $\rho_{fluid} = 0.8\ m\sigma^{-3}$ and the simulation time step was $\Delta t_{MD} = 0.001\tau$. Each simulation was run for 2×10^6 time steps and the calculated quantities were averaged over the last $2 \cdot 10^5$ time steps.

Initially, the rescaling technique and the one based on the Maxwell-Boltzmann distribution have been tested for a stationary heat transfer problem with continuum conditions $T_{con} = 1.5\ \epsilon/k_B$ and $u_{con,x} = 0\ \sigma/\tau$ on the upper constrained region (see Figure 5.1). The Chapman-Enskog distribution was utilised when the results obtained from the Maxwell-Boltzmann were not physically correct. A typical example is the application of the Maxwell-Boltzmann distribution in the dilute gases.

In the second test case the boundary conditions were $T_{con} = 1.0\ \epsilon/k_B$ and $u_{con,x} = 1.0\ \sigma/\tau$. The temperature of the constrained region was equal to the wall temperature and, thus, the temperature was expected to remain nearly constant throughout the molecular domain. The results from both BCT methods are in good agreement with the theory as shown in Figure 5.2. A linear velocity profile was obtained and the temperature remained constant and equal to $1.0\ \epsilon/k_B$.

It was found that for the rescaling technique the size of the BCT region can influence the consistency of velocity values with the macroscopic conditions. In Equation 2.3.2 the atomistic velocities are rescaled to a new mean velocity equal to the continuum constraint. In the current test case this results in an underestimated velocity in the lower boundary of the rescaled region (Figure 5.3). The inconsistency between the macroscopic and microscopic states introduces inaccuracies in the simulation procedure. To address this issue, in

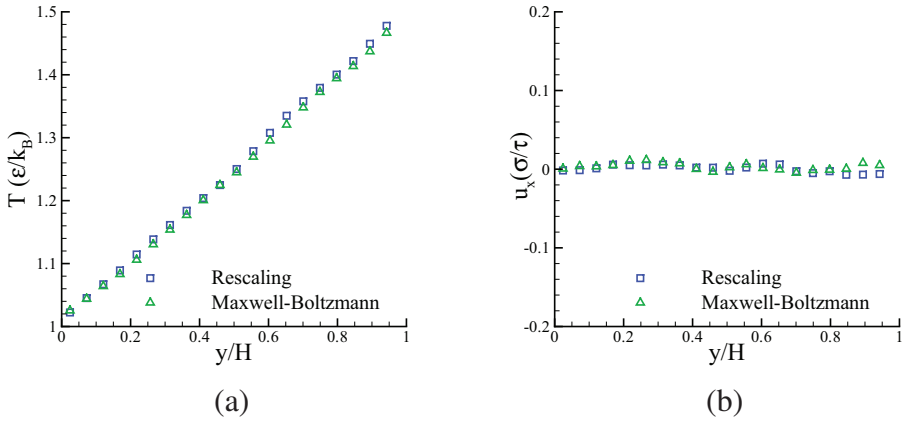

(a) (b)

Figure 5.1: Temperature profile for the Couette flow with $u_{x-con} = 0\ \sigma/\tau$ and $T_{con} = 1.5\ \epsilon/k_B$.

the current test cases the BCT region has been further divided to four bins, with height 2.5σ each.

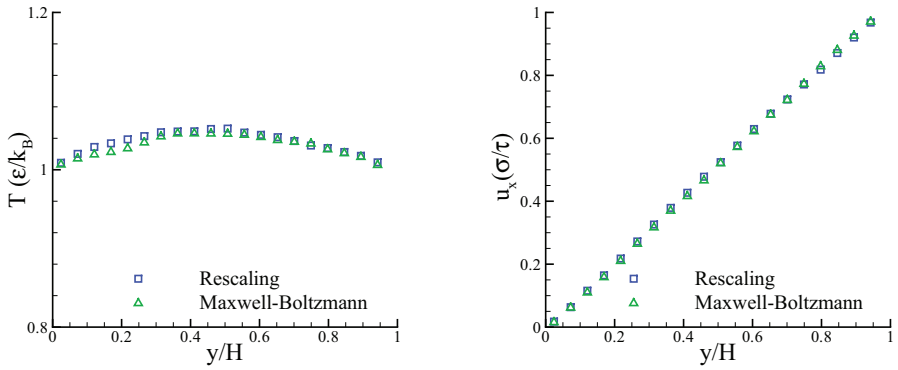

(a) (b)

Figure 5.2: Velocity and temperature profiles for the Couette flow with $u_{x-con} = 1.0\ \sigma/\tau$ and $T_{con} = 1.0\ \epsilon/k_B$.

For the third test case, the continuum conditions in the constrained region were $T_{con} = 1.2\ \epsilon/k_B$ and $u_{con,x} = 1.0\ \sigma/\tau$. Both BCT methods provide similar results. Figure 5.4 shows the linear and parabolic profiles obtained for the velocity and temperature, respectively.

5.1.2 Liquid flow for the general problem

This is essentially a Couette flow problem with the molecular domain being constrained to continuum values on two opposite sides. The size of the molecular domain was 10σ, 30σ

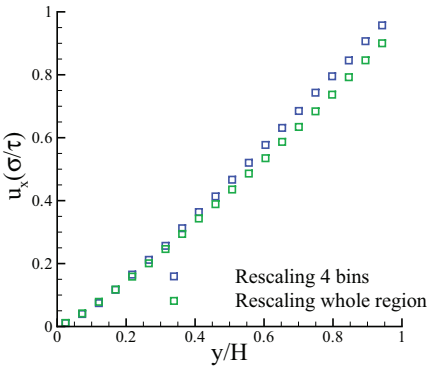

Figure 5.3: Velocity profiles obtained with velocity constraints applied to the whole constrained region as well as the constrained region divided into subdomains.

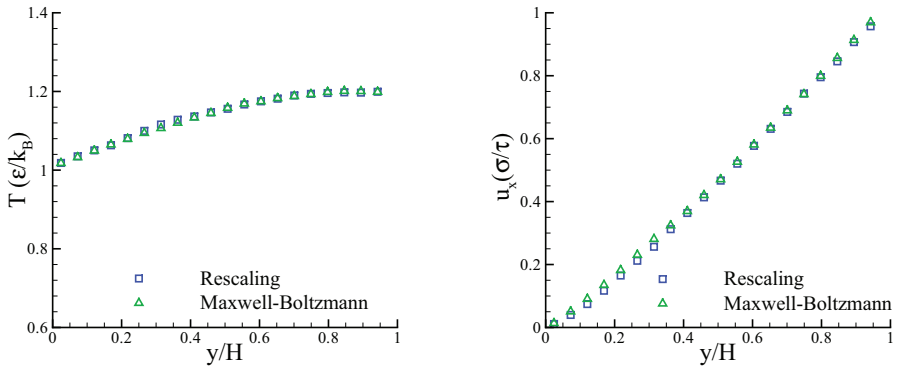

Figure 5.4: Velocity and temperature profiles for the Couette flow with $u_{x-con} = 1.0\ \sigma/\tau$ and $T_{con} = 1.2\ \epsilon/k_B$.

and 10σ in the x, y and z dimensions, respectively. The molecular domain was subdivided into three regions: the upper and lower BCT regions and the flow region in between. Periodic boundary conditions were applied in the x and z dimensions. The lower constrained region was located at $y < 5\sigma$, the flow region at $5 < y < 25$ with height $H = 20\sigma$ and the upper constrained region at $y > 25\sigma$. The simulations were performed with a fluid density $\rho_{fluid} = 0.8\ m\sigma^{-3}$, which resulted in a total number of $2,592$ particles. Using a time step $\Delta t_{MD} = 0.001\tau$, the simulations were run for 2×10^6 time steps. The temperature and velocity measurements were averaged over the last 2×10^5 time steps.

Three simulations were performed with different type of continuum conditions. In the first one, the temperature and velocity applied to the upper and lower boundaries were $u_{con,x}^{uppper} = 0\ \sigma/\tau$, $T_{con}^{upper} = 1.5\epsilon/k_B$ and $u_{con,x}^{lower} = 0\ \sigma/\tau$, $T_{con}^{lower} = 1.0\epsilon/k_B$ respectively. This set-up corresponds to a pure heat transfer problem. Figure 5.5 shows the temperature and

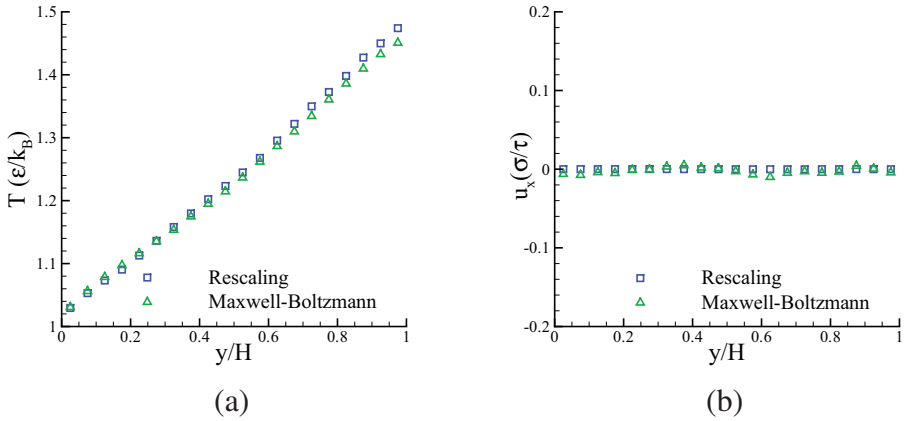

Figure 5.5: Velocity and temperature profiles for the Couette flow with upper boundary conditions $u^{upper}_{x-con} = 0\,\sigma/\tau$, $T^{upper}_{con} = 1.5\,\epsilon/k_B$ and lower boundary conditions $u^{lower}_{x-con} = 0\,\sigma/\tau$, $T^{lower}_{con} = 1.0\,\epsilon/k_B$.

velocity profiles. As expected, the temperature profile obtained using both BCT methods is linear and the profile of the x component of the velocity across the y direction of the domain remains equal to zero. Furthermore, similar temperature profiles are obtained from both techniques. Small deviations are within the margin of statistical error due to the size of the MD domain and constrained region, as well as the time averaging procedure.

In the second simulation, the boundary conditions at the upper and lower boundaries were $u^{uppper}_{con,x} = 1.5\,\sigma/\tau$, $T^{upper}_{con} = 1.0\epsilon/k_B$ and $u^{lower}_{con,x} = 0.8\,\sigma/\tau$, $T^{lower}_{con} = 1.0\epsilon/k_B$, respectively. The velocity and temperature profiles obtained from both BCT methods are similar Figure 5.6.

For the third simulation, the applied boundary conditions were $u^{uppper}_{con,x} = 1.5\,\sigma/\tau$, $T^{upper}_{con} = 1.2\epsilon/k_B$ and $u^{lower}_{con,x} = 0.8\,\sigma/\tau$, $T^{lower}_{con} = 1.0\epsilon/k_B$ at the lower and upper boundaries respectively. Results are shown in Figure 5.7. The temperature profile is parabolic due to the heat generated by viscous dissipation and its conduction towards the boundaries [99]. Small deviations in the temperature profile are associated with statistical errors and the frequency with which the atomistic velocities are sampled from the velocity distribution function. The frequency with which the continuum constraints are applied is an important factor for the resampling method. A high frequency - in the extreme case, where resampling is performed at every time step - leads to a situation where the atoms are basically trapped inside the BCT region, because their velocities are continuously resampled and, therefore, change direction so that these atoms are almost stationary. This effect becomes more apparent in the case of large BCT regions. On the other hand, one should be careful not to choose a too large resampling frequency that will not match the prescribed continuum state.

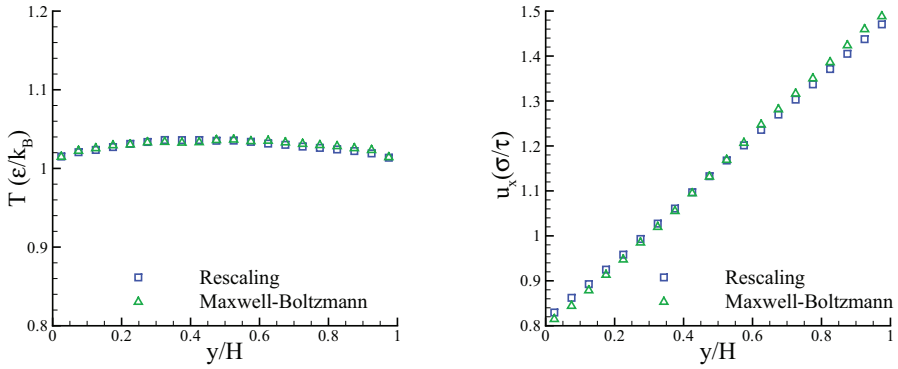

(a) (b)

Figure 5.6: Velocity and temperature profiles for the Couette flow with upper boundary conditions $u_{x-con}^{upper} = 1.5\ \sigma/\tau$, $T_{con}^{upper} = 1.0\ \epsilon/k_B$ and lower boundary conditions $u_{x-con}^{lower} = 0.8\ \sigma/\tau$, $T_{con}^{lower} = 1.0\ \epsilon/k_B$.

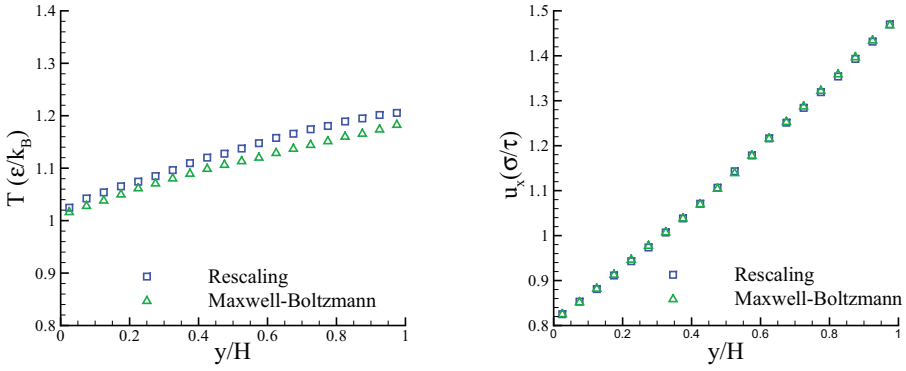

(a) (b)

Figure 5.7: Velocity and temperature profiles for the Couette flow with upper boundary conditions $u_{x-con}^{upper} = 1.5\ \sigma/\tau$, $T_{con}^{upper} = 1.2\ \epsilon/k_B$ and lower boundary conditions $u_{x-con}^{lower} = 0.8\ \sigma/\tau$, $T_{con}^{lower} = 1.0\ \epsilon/k_B$.

5.1.3 Gas flows

The second set of test cases aims to test the applicability of BCT methods to gas flows. The performed simulations were restricted to boundary node problems only. The size of the molecular domain was 200σ, 120σ and 200σ in the x, y and z dimensions, respectively, and similar to the liquid flows the domain was divided into two subregions; the flow region was located at $y < 100\sigma$ and the BCT region at $100\sigma < y < 120\sigma$. At the bottom of the molecular domain a stochastic thermal wall was imposed. A stochastic thermal wall is similar to a reflective wall but corrects or resamples the velocity vector of the reflected atom depending on the transferred thermal energy to or from the wall. Such walls have been extensively used for gas flow simulations [180–183]. In the current study the following rules have been implemented by re-setting the velocities of each atom striking the wall:

$$\begin{aligned} v_x &= \sqrt{\tfrac{k_B T_{wall}}{m}} \cdot \psi \\ v_y &= \pm \sqrt{-\tfrac{2k_B T_{wall}}{m} \cdot ln\psi_1} \\ v_z &= \sqrt{\tfrac{k_B T_{wall}}{m}} \cdot \psi' \end{aligned} \tag{5.1.1}$$

where T_{wall} is the wall temperature; m is the atom's mass; ψ and ψ' are Gaussian distributed random numbers, $N(0,1)$; and ψ_1 is a uniformly distributed random number in $U(0,1)$. Hence, in the adopted model the components of velocity which are parallel to the wall are sampled from a Maxwellian distribution

$$f(v_\alpha) = \sqrt{\frac{m}{2\pi k_B T_{wall}}} exp\left(\frac{-mv_\alpha^2}{2k_B T_{wall}}\right), \tag{5.1.2}$$

where α is the corresponding direction and the normal to the wall velocity component, v_β, is sampled from a Rayleigh distribution given by

$$f(v_\beta) = \frac{m}{k_B T_{wall}} \left|v_\beta\right| exp\left(\frac{-mv_\beta^2}{2k_B T_{wall}}\right) \tag{5.1.3}$$

The ± in Equation (5.1.1) corresponds the upper and lower walls, respectively. The + sign is used at the lower wall in order to force the particle to re-enter the simulation box. If the wall is placed at the upper boundary, the − sign is used.

The first test case concerns simulations where the BCT is enforced through a Maxwell-Boltzmann distribution. The simulations have been performed for different values of gas density with continuum constraints $u_{con,x} = 1.0\ \sigma/\tau$ and $T_{con} = 1.0\ \epsilon/k_B$ and wall temperature $T_{wall} = 1.0\ \epsilon/k_B$. Three values of density were simulated $\rho = 0.02\ m\sigma^{-3}$, $\rho = 0.04\ m\sigma^{-3}$ and $\rho = 0.08\ m\sigma^{-3}$ resulting in the generation of $10,240$, $20,000$ and $40,316$ atoms, respectively. The time step used in the MD simulations was $\Delta t_{MD} = 0.001\tau$ and each simulation was run for 8×10^6 time steps. The macroscopic quantities were averaged

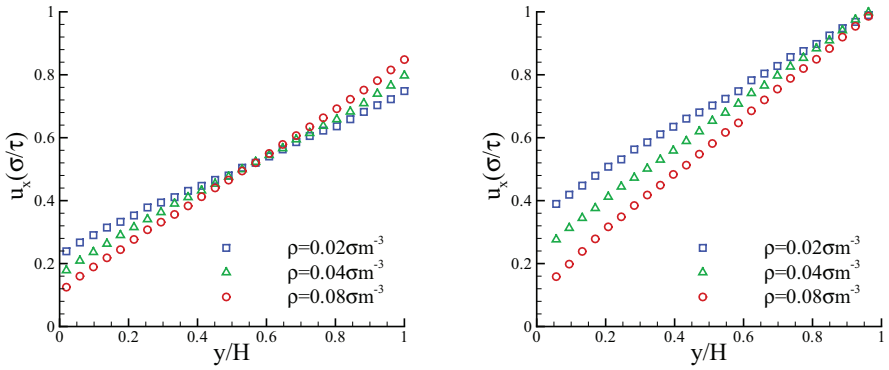

(a) Maxwell-Boltzmann based BCT method (b) Chapman-Enskog based BCT method

Figure 5.8: Velocity profiles obtained with Maxwell-Boltzmann and Chapman-Enskog distributions, respectively, for different gas densities

over the last 2×10^6 time steps.

For low-density gas flows, slip at the boundary is expected, whose magnitude is related to the Knudsen number. High Knudsen numbers result in increased slip [70, 181]. The Knudsen number is calculated by [182]

$$Kn = \frac{\lambda}{L} = \frac{1}{\sqrt{2}\pi\rho\sigma^2 L}, \tag{5.1.4}$$

where λ is the mean free path of the gas, ρ is the number density and L is the characteristic length. Equation (5.1.4) means that low density results in higher Knudsen numbers and, consequently, higher magnitudes of the slip velocity. Figure 5.8(a) shows the velocity profiles obtained from the gas flow using the Maxwell-Boltzmann distribution based BCT scheme for the three densities. As expected, higher slip velocities near the wall are obtained for lower density values. However, large deviations are observed between the applied velocity constraints and the actual velocity in the upper boundary of the flow region. This is because of an additional slip velocity generated between the flow and BCT regions due to the application of the Maxwell-Boltzmann distribution. Note that lower gas density results in higher deviation between the actual and applied velocity [24, 121]. To circumvent the unphysical slip at the constrained region, the same simulations have been performed with Maxwell-Boltzmann distribution replaced by the Chapman-Enskog distribution. Figure 5.8(b) shows velocity profiles obtained with the Chapman-Enskog distribution. Application of this distribution eliminates artificial slip phenomena between the flow and BCT regions.

For the last test case, the rescaling based technique and the method based on resampling the Chapman-Enkog's distribution are utilised for gas flow simulations in the same domain with the previous gas simulations, with density $\rho = 0.05\ m\sigma^{-3}$, and continuum constraints

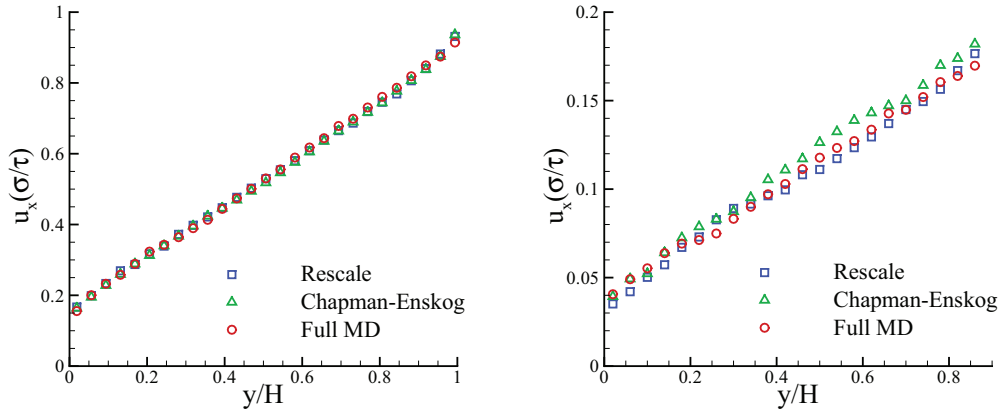

(a) $u_{x-con} = 1\ \sigma/\tau$ (b) $u_{x-con} = 0.2\ \sigma/\tau$

Figure 5.9: Velocity profiles for gas with $\rho = 0.05\ m \cdot \sigma^{-3}$ obtained from the rescaling BCT method, the BCT method based on the Chapman-Enskog distribution and the full MD simulation.

$u_{con,x} = 1.0\ \sigma/\tau$ and $T_{con} = 1.0\ \epsilon/k_B$ and wall temperature $T_{wall} = 1.0\ \epsilon/k_B$. In the simulations, 25,168 particles have been generated, the MD time step was $\Delta t_{MD} = 0.001\tau$, each simulation was run for 8×10^6 time steps and the calculated macroscopic quantities were averaged over the last 2×10^6 time steps.

MD simulations of a larger system have been performed to verify the validity of the results. An MD domain of 200σ in each direction was selected, comprising a total number of 42,592 particles. The density was $\rho = 0.05\ m\sigma^{-3}$ and the time step was 0.001τ. The simulations were performed for 8×10^6 time steps and the calculated quantities were averaged over the last 2×10^6 time steps. Two stochastic thermal walls were placed at the upper and lower boundaries of the simulation domain with conditions chosen as $u^{upper}_{wall,x} = 2.0\ \sigma/\tau$, $T^{upper}_{wall} = 0.8\ \epsilon/k_B$ for the upper wall and $u^{lower}_{wall,x} = 0\ \sigma/\tau$, $T^{lower}_{wall} = 1.0\ \epsilon/k_B$ for the lower wall, respectively.

Figure 5.9(a) shows that results obtained from both BCT methods are in excellent agreement with the large MD simulation. Figure 5.9(b) shows the velocity distributions for continuum velocity $u_{con,x} = 0.2\ \sigma/\tau = 25\ m/s$.

5.1.4 Conclusions

An investigation of different mesoscale approaches for coupling macroscopic and microscopic simulations was presented. Two BCT methods of constraining the molecular domain to the continuum state have been examined, one based on rescaling the atoms' velocities and the other one is based on velocity sampling through a distribution function.

The rescaling BCT method was implemented in conjunction with a velocity reversing scheme with regards to the macroscopic pressure. Applying the correct value of pressure and minimising any associated artifacts is crucial for the performance of any hybrid scheme. Inconsistencies in the pressure can shrink the simulation domain or even make particles drift away. This can generate errors and instabilities in the hybrid procedure. Simulations performed with the rescaling BCT method show that it can be successfully applied to both liquid and gas flows. The size of the regions where the velocity constraints are applied has to be selected carefully in order to obtain consistent velocities with the continuum state.

For the second BCT method, Maxwell-Boltzmann and Chapman-Enskog distribution functions were examined. The former has been used in liquid simulations and the results were found in good agreement with the rescaling BCT method. The size of the constrained domain, the way that the domain is terminated and the sampling frequency may have significant impact on the results when the Maxwell-Boltzmann distribution is used. Inadequate sampling frequency can lead to unrealistic effects, such as trapping of particles in the constrained region, or deviations between the macroscopic and microscopic velocities. Selection criteria of these parameters depends on the problem in question and cannot be defined explicitly. The application of the Maxwell-Boltzmann distribution to gas flows leads to discrepancies between the desired and the actual applied velocity. This discrepancy can be corrected by applying the Chapman-Enskog distribution. For the correct application of the Chapman-Enskog distribution the equilibrium pressure has to be applied, due to the absence of continuum solver for the current case the equilibrium gas pressure is applied that has been pre-calculated by previous MD simulations.

The Maxwell-Boltzmann distribution function is sufficient for equilibrium cases however for non equilibrium flows the Chapman-Enskog distribution which is a perturbation expansion of the Maxwell-Boltzmann has to be employed. The Chapman-Enskog velocity distribution function is a second order expansion in Kn and includes terms up to Kn^2. Therefore, as higher Kn are employed and non-equilibrium cases are simulated the Maxwell-Boltzmann fails to fully describe the physical phenomena.

The results obtained are then consistent with the rescaling-based BCT method and larger MD simulations.

The selection of BCT method is not a trivial issue. It depends on the specific simulated problem and a number of other parameters such as the accuracy requirements and the available computational resource. The main advantage of the rescaling method is its generic nature and broad range of applicability. However, it is less computationally efficient compared to the velocity distribution function method.

5.2 Polymeric fluid under Poiseuille flow

Accurate modelling of confined polymers is of paramount importance for the polymer processing industry [184]. One of the major problems in polymer fluid dynamics is the development of a constitutive equation for modelling the stress tensor τ [185]. In the current example hybrid PWC simulations are employed to study a polymeric fluid, with chain length $N = 30$, under Poiseuille flow. In the current problem molecular simulations are employed to calculate the constitutive equations of the polymeric fluid.

Specifically, NEMD simulations are performed for a constant bead density $\rho = 0.8\, m\sigma^{-3}$ and constant temperature $T = 1\ \epsilon k_B^{-1}$ in cubic boxes with the Parrinello-Rahman deformation box. The polymer chains are modelled as bead-spring chains; any two beads in the box interact through the 6-12 LJ potential with a cut-off distance $r_c = 2.2\,\sigma$. In order to model the spring an attractive nonlinear FENE potential is used

$$V^{FENE} = -\frac{H \cdot Q^2}{2} \ln\left[1 - \left(\frac{r}{Q}\right)^2\right], \tag{5.2.1}$$

where H is the spring constant and Q is the maximum extension of the spring. For the simulations presented here, the values of the spring co-efficients H and Q are $30\,\epsilon/\sigma^2$ and $1.5\,\sigma$ respectively. The chosen values for the spring co-efficients ensure that unphysical bond crossing is energetically unfeasible [186].

For the PWC hybrid simulations of the accelerated Poiseuille flow, a channel with height $H = 220\,\sigma$ and no-slip boundary condition is chosen. The time step for the continuum solver is 5τ and the flow is driven through an external force $f_0 = 0.0022\,\epsilon/\sigma$ applied in x direction. Two polymeric fluids have been simulated with chain lengths $N = 10$ and $N = 30$ respectively. The shear stresses needed for the continuum solver are estimated at every continuum time step through microscopic simulations around every grid point. The MD simulations are constrained by the shear rate obtained from the continuum solver. MD simulations are performed for $3 \cdot 10^4$ number of time steps with the time step of 0.005τ.

The flow is homogenous in the $x - direction$ and therefore the momentum equation reduces to:

$$\rho u_t = (\tau_{12})_y + f_0 \tag{5.2.2}$$

with no-slip boundary conditions. The equation is solved in continuum uniform grid with 22 points using finite difference discretisation.

In Figure 5.10, the non-newtonian viscosity $\eta = \frac{\sigma_{xy}}{\dot{\gamma}}$, as calculated by the molecular model during the PWC simulations, versus the shear rate for a chain with length $N = 30$ is presented. The shear viscosity is decreasing for increased shear rate due to the intermolecular bond stretching [187]. The viscosity, of a FENE polymeric chain in shear thinning, over shear rate approaches a power law curve: $\eta \propto \dot{\gamma}^{-a}$ [187]. Using curve fitting, the values of a in the performed simulations has been determined as $a = 0.291$ for the 10mer

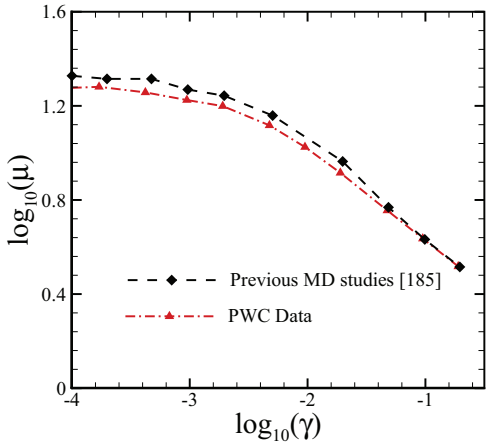

Figure 5.10: Non-Newtonian shear viscosity η for FENE model versus shear rate γ for chain length $N = 30$, the PWC data are compared with NEMD data by previous MD studies

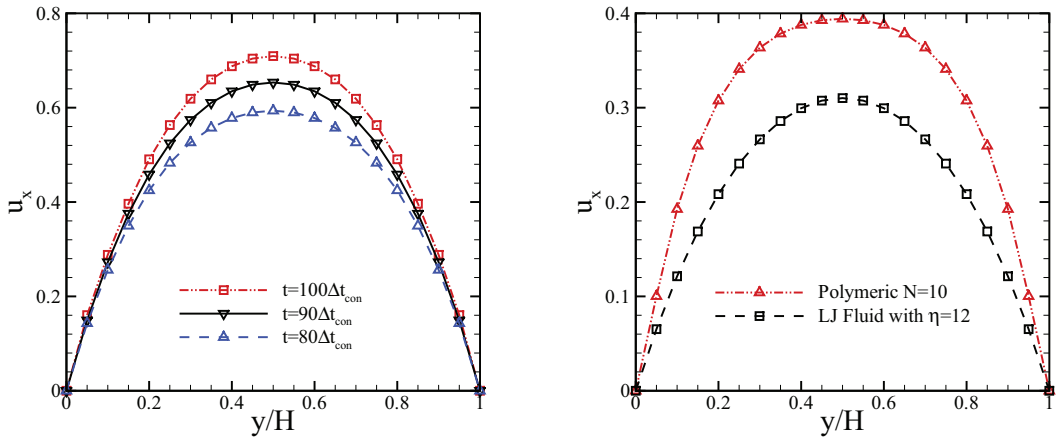

Figure 5.11: (a) Velocity profiles (in LJ units) in the Poiseuille flow of polymer with chain length N=10 obtained from PWC and (b) Velocity Profiles (in LJ units) in the Poiseuille flow of a 10mer polymeric fluid compared with a fluid with viscosity $\eta = 12\frac{(\epsilon \cdot m)^{1/2}}{\sigma^2}$, obtained from PWC

and $a = 0.3685$ for the 30mer. This is in agreement with previous studies of Kroger and Hess [186], who found that a varies from 0.3 to 0.7 for polymers with different number of beads.

The shear rate in the pressure driven Poiseuille flow varies linearly across the height of the channel with the maximum at the wall dropping to zero in the centre of the channel. The variation of the shear rate have a significant impact on the shear viscosity of the polymeric fluid. The shear viscosity increases as the shear rate decreases reaching the value at the centre of the channel, which for 10*mer* case is equal to $12\sqrt{\epsilon m}/\sigma^2$. In Figure 5.11(a), the velocity profiles (in LJ units) for the pressure driven Poiseuille flow of the 10*mer* polymer chain are presented at different times, as the flow develops.

The velocity profile from a continuum hydrodynamics perspective, is:

$$u_x(y) = 0.5\mu(\gamma)^{-1}\rho f_x\left[\left(L_y - y\right)y\right] \tag{5.2.3}$$

Figure 5.11(b) compares the velocity profiles of a 10*mer* polymeric fluid with a simple fluid with shear viscosity equal to the maximum zero shear viscosity of the 10*mer* polymeric fluid. The maximum velocity of the polymeric fluid is higher than that of the simple fluid at the same time due to a lower mean viscosity, as shown in Equation (5.2.3).

5.3 Slip Poisseuile flow

In micro and nanofluidic devices, where large surface to volume ratio is present, the fluid flow can be significantly affected by the existence of slip in the liquid-solid interface. The most commonly used model for the slip prediction is the Navier boundary condition [154] where the slip velocity is proportional to the local shear rate

$$u_{slip} = L_s \cdot \gamma, \tag{5.3.1}$$

where u_{slip} is the slip velocity, L_s is a constant slip length and γ the local shear rate. The application of this model delivers realistic results for a specific flow regime however fails to provide an overall description regarding the transfer of momentum at the solid liquid interface [154].

Generally, the slip length is not constant and there is a non linear relationship between the slip velocity and the local shear rate. A number of parameters such as the surface roughness, hydrophobicity and hydrophilicity and the shear rate have great impact on the slip generated. To circumvent the aforementioned issues and increase the modelling accuracy, hybrid PWC simulations were performed, where the slip was calculated from first principles. The chosen test case was a planar Poiseuille flow driven in by an external force f_x in the x direction.

Algorithm 5 PWC -Numerical and Molecular Operations

1. For every input velocity u_{con} find $m \in \mathbb{Z}$ where $u_{in} + m\delta u < u_{con} < u_{in} + (m+1)\delta u$
2. Search in the stored data if simulations with inputs either $u_{in} + m\delta u$ or $u_{in} + (m+1)\delta u$ have been performed
3. If one or more simulations have been previously performed, then run MD with the coresponding inputs
4. Store the slip velocities produced, u^m_{slip} and/or u^{m+1}_{slip}, in the simulation's data library
5. Based on the library data calculate the slip velocity needed from the continuum solver:

$$u_{slip} = u^m_{slip} + \frac{u^{m+1}_{slip} - u^m_{slip}}{\delta u}\left(u_{con} - (u_{in} + m\delta u)\right)$$

A Lennard-Jones fluid was used with density $\rho = 0.81\, m\sigma^{-3}$ and temperature $T = 1.1\, \epsilon k_B^{-1}$ which corresponds to viscosity $\mu = (2.0 \pm 0.2)\, \tau\sigma^{-3}$[188]. The channel height was $H = 2h = 220\sigma$ and the investigated range of force f_x was from 0.002 to $0.003\epsilon/\sigma$.

The analytical solution of the Navier-Stokes equation for the slip Poiseuille flow is

$$u(y) = \frac{\rho f_x}{2\mu}\left(h^2 - y^2\right) + u_{slip}. \tag{5.3.2}$$

Since the density and temperature were constant throughout the simulation domain, the only input parameter for the molecular simulations was the continuum velocity near the boundary solid wall. The MD simulations were performed with $u_{in} = 0.0\ \sigma/\epsilon$ and $\delta u = 0.5\ \sigma/\epsilon$, which means that molecular simulations were performed only for velocities multiple of 0.5 and the slip for all other input velocities was calculated through interpolation as it is shown in Algorithm 5. For the PWC scheme MD simulations were performed for the lower and upper walls and provided to the continuum solver the corresponding slip velocity. The size of the atomistic domain was 20σ, 28σ, 10σ in the x, y and z direction respectively, resulting in a total number of 5197 atoms. The continuum velocity was enforced onto the atoms in the region $26\sigma < y < 28\sigma$, whose velocity vectors were drawn every 100 time steps from a Maxwell-Boltzmann distribution according to the u_{con} and T_{con}. The molecular time step was 0.005τ and a total number of time steps were performed for each simulation. In the molecular simulation, the wall was modelled by two planes of a fcc lattice with an orientation that forms a (111) surface. The angle between the flow and the orientation of the surface was zero, which in combination with the (111) fcc plane minimises the roughness of the surface and consequently maximises the slip at the boundary. The interatomic interactions of the wall and fluid material were like the fluid modelled by the shifted LJ-potential. The wall density was $\rho = 4.0\, m\sigma^{-3}$ and temperature $T = 1.1\ \epsilon k_B^{-1}$. Wall-fluid interactions were also modelled by the LJ potential with energy ϵ_{wf} and length scale σ_{wf} and the parameters used were $\epsilon_{wf} = 0.4\epsilon$, $\sigma_{wf} = 0.75\sigma$ [154]. The heat exchange was controlled by a Langevin thermostat with a random uncorrelated force and a friction

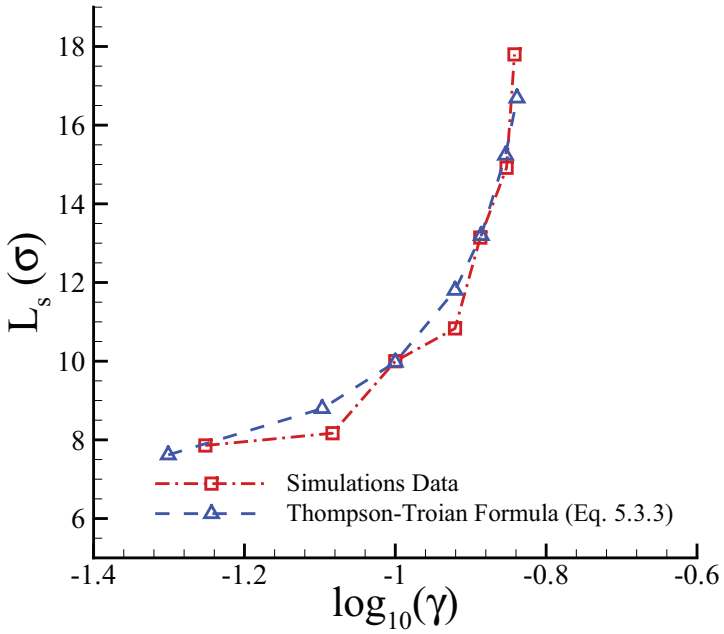

Figure 5.12: Variation of slip length with the shear rate

term $\Gamma = 1.0\tau^{-1}$, where τ is the characteristic time $\tau = \left(m\sigma^2/\epsilon\right)^{0.5}$ [23, 154]. The thermostat was only applied in the z-direction to avoid any undesirable influences in the flow direction.

Figure 5.12 shows the variation of the slip length Ls, as it is calculated from the MD simulations performed, as a function of the local shear rate. An interesting feature is that from lower shear rates the slip length presents small variations and it's equal to its minimum value . This is consistent with the Navier boundary conditions however when the shear rate is increasing the Navier condition breaks down and the slip length varies non linear with the shear rate. A form that has been suggested [154] to describe this non linear relationship is

$$L_s = L_{s_0}\left(1 - \frac{\gamma}{\gamma_c}\right)^{-0.5}, \tag{5.3.3}$$

where γ_c is a critical value where the L_s appears to diverge. Figure 5.12 shows good agreement between the data produced from the MD simulations performed in the hybrid framework and Equation 5.3.3 which is based in previous molecular studies. Figure 5.13(a) shows the velocity profile for a Poiseuille flow with driving force $f_x = 0.002 - 0.003\ \epsilon/\sigma$ as it is calculated from PWC simulations. From Figure 5.13(b) one can be identified that the slip velocities are increasing non-linearly as a function of the driving force and consequently the shear rate.

Equations (5.3.1), (5.3.2) and (5.3.3) can be utilised for calculating the slip velocities analytically. Using Equation 5.3.2, the shear rate can be determined and can be substituted

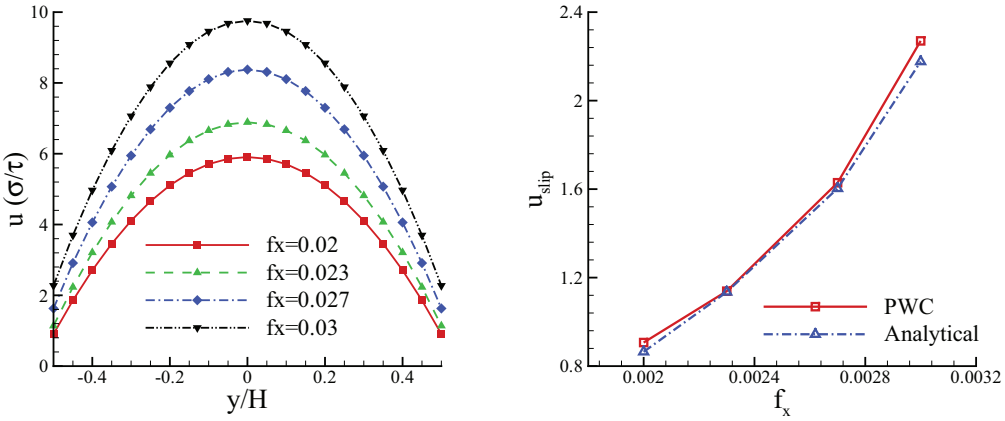

(a) Velocity profiles under different values of the driving force

(b) Analytical and computational data of slip velocity as a function of the driving force

Figure 5.13: Velocity profiles and slip length under different values of the driving force

in Equation 5.3.3 to obtain the slip length and consequently the slip velocities. Figure 5.13(b) shows the hybrid PWC values of the slip velocities as a function of the driving force towards the analytical values from Equations (5.3.1), (5.3.2) and (5.3.3). Both outcomes are in good agreement and small deviations that are observed for the minimum and maximum values of the driving force are due to the microscopic simulations of the hybrid scheme which are subject to statistical errors and due to empirical nature of Equation (5.3.3), which is derived from MD simulations.

5.3.1 Conclusions

In this study the Point Wise Coupling multiscale method is applied to nanoscale and mesoscale fluid flows with slip at the liquid solid interface. The PWC method effectively decouples the length and timescales. The proposed interpolation scheme utilises the data produced by previous MD simulations through a numerical optimisation procedure. Hence, PWC effectively avoids performing MD simulations for nearly identical continuum states realising an extreme reduction of the method's computational burden. By tuning the interval parameter of the interpolation scheme, for example δu or u_{in} , the number of the performed MD simulations can be regulated to balance between accuracy, stability and efficiency.

Despite the fact that the interpolation scheme minimises the number of molecular simulations, the microscopic solver is still the most computationally demanding task of the entire method. The applicability and commercialisation of these methods in the industrial environment requires the development of new versatile strategies to further advance the existing hybrid frameworks.

Case	ϵ_{wf}/ϵ	σ_{wf}/σ	ρ_w/ρ
(1)	0.6	1	1
(2)	0.6	0.75	4
(3)	0.2	0.75	4

Table 5.1: Couette slip flow simulation parameters

5.4 Slip Couette flow

The flow of a fluid inside a micro or nanochannel can be significantly influenced by liquid slip conditions at the solid boundary. As opposed to gas flows, liquid flows can be described by incompressible Navier-Stokes equations even at nanoscale [6]. However, whereas for gases, the breakdown of the continuum model can be predicted based on the kinetic theory, for liquids the situation is less clear [189]. There are fundamental open questions regarding the applicability of no-slip boundary conditions. The conditions under which the no-slip boundary assumption becomes inaccurate and the relationship of stress and strain rate non-linear are not known from first principles [189].

In the current example, the number of particles generated in the microscopic domain is defined from the continuum density and their velocities are initialised through a Maxwell-Boltzmann distribution based on the continuum temperature. The macroscopic velocity is imposed through the upper boundary of the molecular domain, in a reservoir region with height $h = 4\sigma$ and by utilising the velocity rescaling formula given in Equation (3.2.2). The simulations are assumed to be isothermal and therefore, since there is no need to exchange temperature information, the temperature in the entire molecular region is controlled through a thermostat. The molecular simulations are employed at the beginning of every continuum time step to calculate the slip velocity in the solid-liquid interface which is transferred to the continuum solver through the velocity boundary conditions.

The solid wall is modelled as two immobile planes of a (111) fcc lattice. The solid surface orientation along with the orientation of the flow have major influence on the total amount of slip [69] that is generated due to the nanoscale roughness arising from the arrangement of the wall atoms. For the current test case the (111) fcc plane is employed in order to minimise the atomic surface roughness and consequently maximise the slip at the boundary.

The shifted Lennard-Jones (LJ) 6-12 potential, with cut off distance $r_c = 2.2\,\sigma$, is employed to model the inter-atomic interactions of the wall and fluid particles. The fluid's density and temperature are $\rho = 0.81\,m\sigma^{-3}$ and $T = 1.1\,\epsilon\,k_B^{-1}$ respectively. The wall-fluid interactions are also modelled by the LJ potential with energy ϵ_{wf} and length scale σ_{wf}. Parameters used in the simulations are summarised in Table 5.1.

The first set of parameters is used for creating no-slip boundary conditions and the

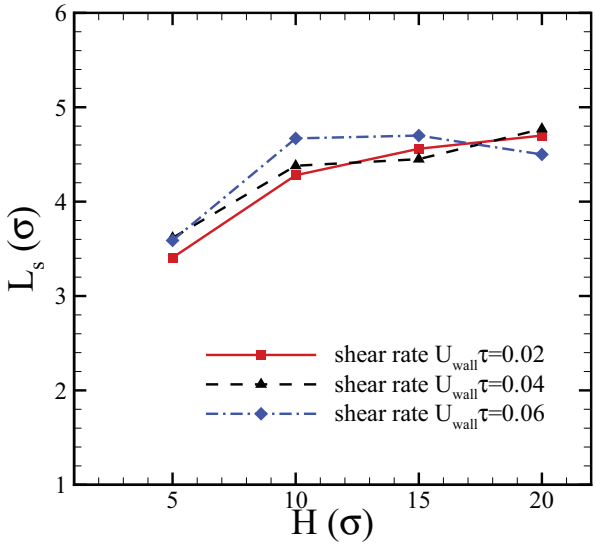

Figure 5.14: Slip lengths variations for different channel heights and $\epsilon_{wf} = 0.6\,\epsilon$, $\sigma_{wf} = 0.75\,\sigma$ and $\rho_w = 4\,\rho$

other two correspond to slip boundary conditions [154]. The heat exchange is controlled by a Langevin thermostat with a random uncorrelated force and a friction term $\Gamma = 1.0\,\tau^{-1}$, where τ is the characteristic time $\tau = (m\sigma^2/\epsilon)^{1/2}$ [23, 154]. The thermostat is only applied in the z direction to avoid any undesirable influences in the flow direction.

5.4.1 PWC Couette flow

An important parameter for the realistic behaviour of the PWC hybrid method is the size of the molecular domain which has to be sufficiently large to capture the physics of the problem. In order to explore the influence of the molecular domain size, a number of MD simulations have been performed with different domain sizes, with the slip length $L_s = \frac{u_s}{\left(\frac{\partial u}{\partial n}\right)_w}$ used as validation criterion. MD simulations were performed in four domains with different heights $H = 5,\ 10,\ 15$ and 20σ and dimensions in the $x-z$ plane $10\times 10\ \sigma^2$. The height H refers to the size of the molecular domain in the direction y normal to the wall. The height refers to the size of the molecular domain in the direction normal to the wall. The variation of the slip length, for various shear rates, with the height of the molecular domain is shown in Figure 5.14.

For heights less than $10\,\sigma$, the slip length is under estimated and for heights larger than $10\,\sigma$ the mean value of the slip length for different shear rates presents minor differences. The former are in good agreement with [23] where for channel heights larger than $10\,\sigma$ the results from MD were consistent with continuum assumptions. Therefore a height of 10σ

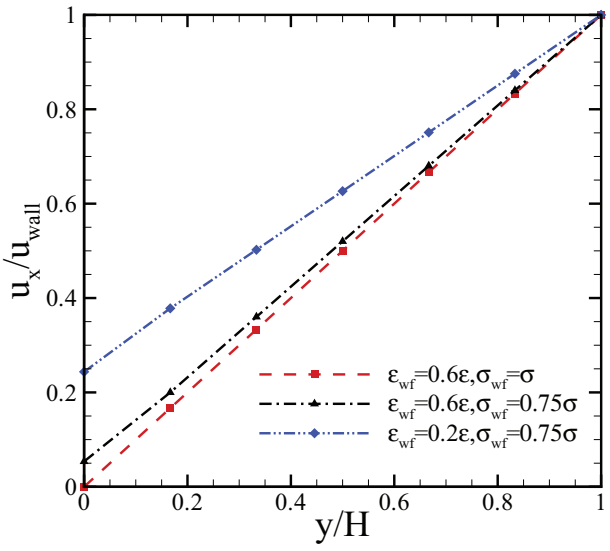

Figure 5.15: Velocity profiles for $H = 50\sigma$ under slip and no-slip boundary conditions

has been selected for the height of the atomistic region. The size of the molecular domain should be minimal aiming to reduce the impact of the of the computationally intensive molecular solver to the overall computational procedure.

For the continuum model, the flow is homogenous in the $x-direction$ and therefore the momentum equation reduces to:

$$\rho u_t = (\tau_{12})_y \tag{5.4.1}$$

with $u = U_w$ at the upper boundary and slip velocities calculated by MD at the lower wall. The equation is solved in continuum uniform grids with grid spacing $\delta y = 10\sigma$ using finite difference discretisation.

Previous MD studies [154] have identified that the degree of slip at the boundary depends on a number of parameters including the strength of the solid-liquid interaction, the thermal roughness of the interface and the ratio of wall and liquid density. To investigate the effects of the solid-fluid interaction strength, PWC hybrid simulations of Couette flows have been performed. In Figure 5.15 the velocity profiles for a channel with height $H = 50\,\sigma$ are presented for three different sets of parameters of the solid-liquid interaction. The time step for the continuum solver was equal to 10τ and the time step of 0.005τ was used in the microscopic solver.

The results obtained from the PWC are in good agreement with those obtained from other hybrid methods based on the domain decomposition [18] and those obtained from fully MD simulations [154] where the maximum deviation for the slip velocity ranges from 0% to 24% of the upper wall velocity u_{wall} for the no-slip and the slip boundary conditions

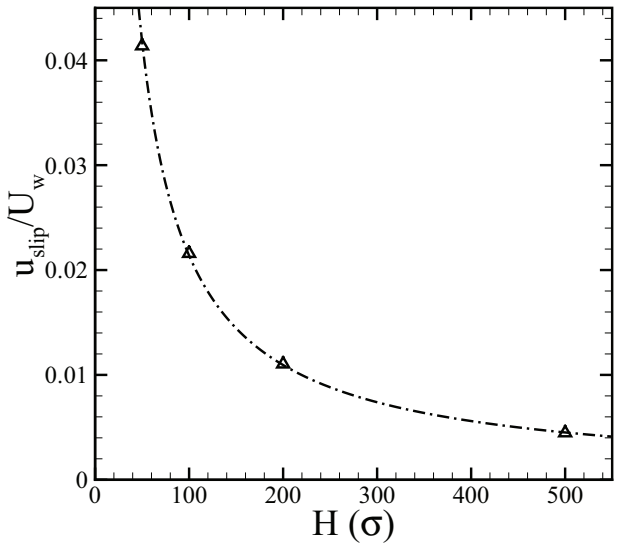

Figure 5.16: Velocity profiles near the bottom wall for Couette Flow in different channels under constant shear rate

respectively.

5.4.2 Channel's height effects

PWC hybrid simulations have also been performed to study the correlation between the channel height and the slip boundary velocity. In particular, Couette flow simulations under a constant shear rate $U_w\tau/H = 0.06$ for four channels with heights $50\,\sigma$, $100\,\sigma$, $200\,\sigma$ and $500\,\sigma$ have been performed. The wall-fluid parameters for all the different channel heights have been $\epsilon_{wf} = 0.6\,\epsilon$, $\sigma_{wf} = 0.75\,\sigma$ and $\rho_w = 4\,\rho$. The MD simulations are performed around the lower grid point for $5 \cdot 10^3$ number of time steps every continuum time step.

In Figure 5.16, the slip velocity, normalised over the upper wall velocity, is presented as a factor of the channel's height. The ratio of the slip velocity over the velocity of the moving wall is decreasing as the channel height becomes larger. Since the interactions between the wall and the fluid are identical for all channel heights, the slip length and slip velocity should essentially be the same in all cases. The flow in all channels has the same constant shear rate and a higher channel height results in higher velocities of the upper wall. Therefore, the ratio of the slip velocity over the upper wall velocity is decreasing, following a power law (see Figure 5.16) as the height of the channel increases. Comparing the results with continuum analytical solution for the no-slip flows $u_x/U_w = y/H$ it becomes clear that for the narrower channels, with a height of $50\,\sigma$ and $100\,\sigma$, the deviation in the velocity profile due to the slip is significant, whereas for the channels with height larger than $500\,\sigma$

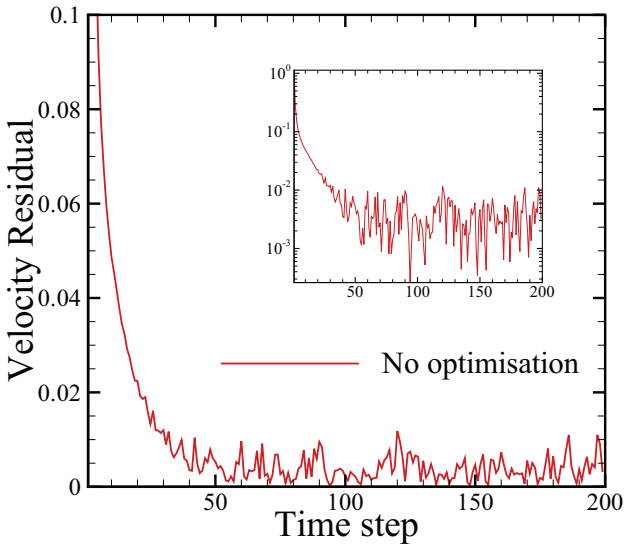

Figure 5.17: History of the RMS residual for velocity for simulations performed in channel with height $H = 50\sigma$

it can be assumed that the no-slip condition still holds.

5.4.3 PWC Linear Optimisation

In the Couette flow test case, presented previously, MD simulations were performed at the beginning of every continuum time step. As a consequence, molecular simulations have been carried out for almost identical continuum inputs resulting to an increased computational cost without any subsequent accuracy advantages. Apart from the additional computational burden, simulating nearly identical continuum states will contribute to the transfer of the intrinsic molecular fluctuations to the continuum solver and therefore will impact its stability and convergence. Figure 5.17 shows the history of the RMS velocity residual. The fluctuations of the velocity values reveal the presence of the molecular solver. These fluctuations occur due to the hybrid boundary condition applied at the lower wall, however the overall convergence trend in these cases is not greatly affected.

Aiming to minimise the computational cost of the PWC and reduce the residual oscillations a numerical optimisation procedure has been employed. The input data for the molecular solver, in the current test case, are essentially the continuum velocity of the first cell above the lower wall and the calculated data are the slip velocity at the solid-liquid interface. In the numerical optimisation procedure MD simulations were performed with $u_{in}^{con} = 0.0\ \sigma/\epsilon$ and $\delta u^{con} = 0.1\ \sigma/\epsilon$. The simulations have been carried out for channel height $H = 50\sigma$.

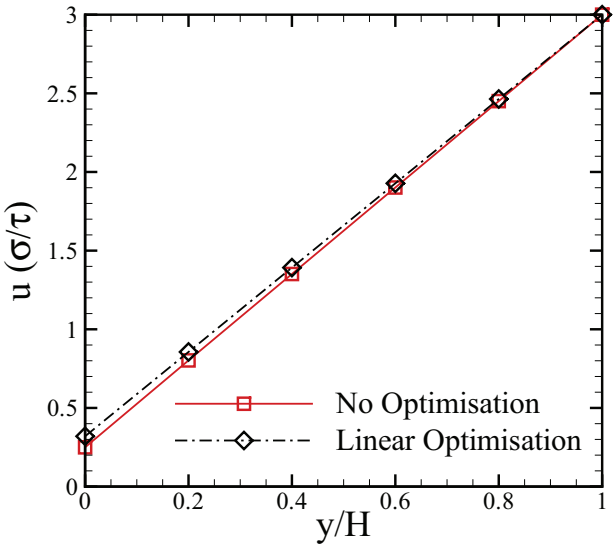

Figure 5.18: Velocity profiles as calculated by PWC without any optimisation and with Linear Optimisation $\delta u = 5 \cdot 10^{-3}$

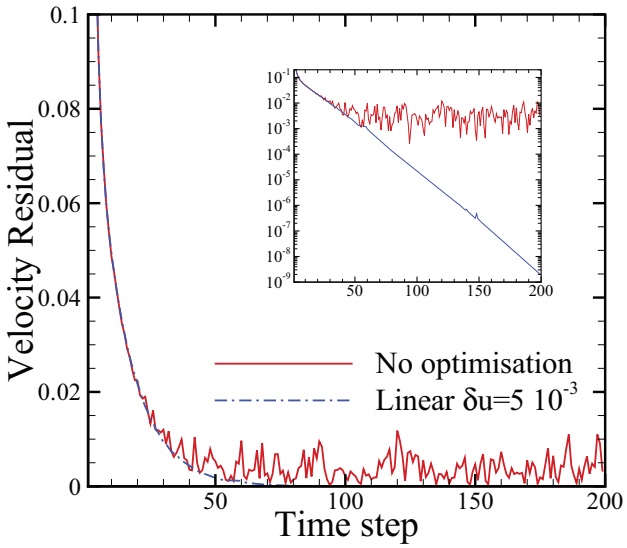

Figure 5.19: History of the RMS residual for velocity for simulations performed in channel with height $H = 50\sigma$

Figure 5.18 shows the velocity profiles as calculated by PWC with and without the presence of the optimisation procedure. The outcomes from both cases are in good agreement. Near the lower wall small deviations are observed mainly due to the inherent fluctuations of molecular's solver outcomes. One of the advantages that the numerical optimisation offers is the oscillations' reduction of the information transferred to the continuum description. This can be identified in Figure 5.19 where the fluctuations' magnitude and frequency have been suppressed. The linear optimisation offers a significant enhancement regarding the stability and convergence of the continuum solver however is still dependent of the values of δu. Specifically, in cases where δu is very small or $\delta u \to 0$ the advantages of the linear optimisation are eliminated. For instance, if $\delta u = 10^{-4}$ for the current example this will be translated to molecular simulations at every continuum time step. The Linear optimisation although it prohibits the propagation of any instabilities towards the continuum side does not take into account the oscillating nature of the atomistic outputs and provide statistically averaged data.

To circumvent these problems the selection of the discretisation parameters should be made cautiously and in case where small values of δu for example have to employed more sophisticated interpolation techniques with smoothing capabilities can be adopted.

5.4.4 PWC Neural Network optimisation

The neural network optimisation has been also employed to study the slip Couette flow case. In the current example one neural network has been used with one input, the continuum velocity, one output, the slip velocity and two hidden layers with 3 neurons each. The hybrid simulations have been performed for two confidence intervals $\delta u = 10^{-3},\ 5 \cdot 10^{-3}$. The confidence intervals to one extend determine the number of atomistic simulations that are performed. In the current case 75 and 50 MD simulations have been performed for $\delta u = 10^{-3}$ and $\delta u = 5 \cdot 10^{-3}$ respectively. The differences in the PWC outputs for the two confidence intervals are less than 1% showing the consistency of the method along with the predictive abilities of the neural networks that can produce consistent outputs even when trained with different amount of data. Table 5.2 shows the root mean square differences (RMSD) between velocity outputs, for various values of δu, as produced by PWC with neural network optimisation with $\delta u = 10^{-3}$ and outcomes produced with linear optimisation. The results are generally in good agreement however the outcomes produced from the linear optimisation tend to underestimate the slip velocity. The main reason for that behaviour is the lack of statistical smoothing and averaging of the atomistic outputs in the linear optimisation. Linear optimisation takes into account only the outputs for specific inputs and not the averaged output values for adjacent input data.

The main advantage of the neural network optimisation is that for obtaining the final output all the previously performed simulations contribute and only those that are in the proximity area of the input values. Therefore, the networks are trained to capture the physical phenomenon and only to perform a numerical interpolation. Additionally, after the

δu	RMSD
$5 \cdot 10^{-3}$	5.7%
10^{-2}	7.2%
$5 \cdot 10^{-2}$	7.1%

Table 5.2: Root mean square difference between PWC outcomes with NN optimisation with $\delta u = 10^{-3}$ and linear optimisation for various δu

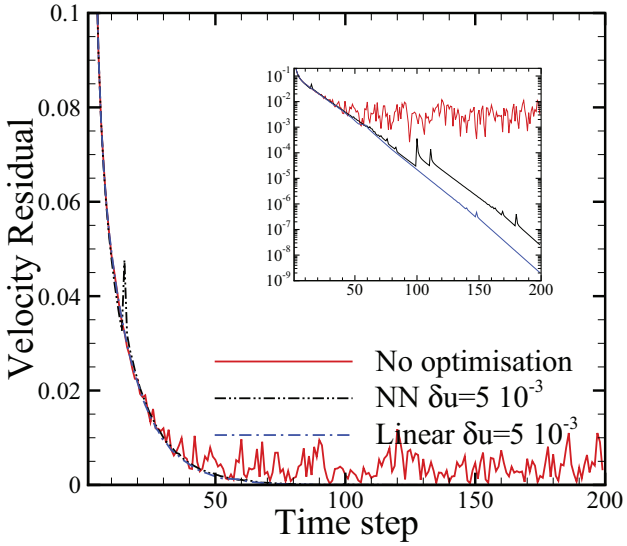

Figure 5.20: History of the RMS residual for velocity for PWC without any optimisation and for PWC with Linera and NN optimisation

completion of the hybrid simulations the neural networks generated can be further utilised, for example as slip models in the current case, for continuum simulations purposes.

5.5 Heat transfer in Couette flow

In the current case the heat transfer in Couette flow with slip boundary conditions is studied. PWC simulations are employed near the bottom wall to provide adequate information regarding the slip's magnitude. The existence of slip is not only dependent to the local shear rate and the interfacial interaction parameters between the solid and the fluid but also to the local temperature. Therefore, in the hybrid set-up the information transferred from the continuum to the molecular description includes the local velocity, density and temperature. Additionally, the PWC simulations will be able to model and capture the temperature jumps noticed near the thermal walls, as shown in Sec. 4.4.

In the continuum description the heat transfer is described through the following equation [99]

$$\frac{\partial T}{\partial t} + \boldsymbol{u} \cdot \nabla T = \frac{\lambda}{\rho c_u} \nabla^2 T + \frac{2\mu}{\rho c_u} \left[\left(\frac{\partial u_x}{\partial x} \right)^2 + \left(\frac{\partial u_y}{\partial y} \right)^2 + \frac{1}{2} \left(\frac{\partial u_x}{\partial y} + \frac{\partial u_y}{\partial x} \right)^2 \right] \tag{5.5.1}$$

where c_u is the specific heat, λ the thermal conductivity and μ the dynamic viscosity. The CFL number employed in the continuum solver is 0.25.

5.5.1 Hybrid simulations

For the current case the size of the molecular domain is 12σ in the x and y direction and 4σ in the z direction. The upper region with height 2σ and $10\sigma < y < 12\sigma$ is used as a reservoir for the application of the continuum conditions to the atomistic description. In this region the particles' velocities are rescaled every 100 molecular time steps to match the continuum temperature and velocity figures. A reflective plane is placed parallel to the solid in the upper position along the $x - axis$ to prevent any particles from moving away from the simulation box. The solid wall is modelled as two planes of (111) fcc lattice and its particles are allowed to oscillate around their lattice site with a harmonic potential with stiffness $\kappa = 400\ \epsilon\sigma^{-2}$. The particle velocities at each wall plane are rescaled independently through a velocity rescaling thermostat to temperature $T = 1.1\ \epsilon k_B^{-1}$. In the remaining molecular area we don't apply any other thermostat and the heat generated during the simulations is dissipated through the thermal wall and the buffer region.

The fluid's density is $\rho = 0.81\ m\sigma^{-3}$ resulting to a 1760 number of fluid particles including the ones in the buffer region. The density employed for the wall is $\rho = 4.0\ m\sigma^{-3}$ corresponding to 470 solid particles. The interaction parameters for the wall/fluid interface are $\epsilon_{wf} = 0.6\,\epsilon$, $\sigma_{wf} = 0.75\,\sigma$ that correspond (as described in Sec. 5.4) to apparent slip. The fluid's viscosity is $\mu = 2.08\ \epsilon\tau\sigma^{-3}$, the thermal conductivity is $\lambda = 7.7\ k_B(\sigma\tau)^{-1}$ and the specific heat is $c_u = 2.43\ k_B/m$ [99].

PWC hybrid simulations are carried out with molecular modelling being employed near the lower wall aiming to provide accurate boundary condition regarding the slip velocities and the temperature jumps. In particular, the size of the continuum domain is $H = 100\ \sigma$ with the upper wall moving with velocity $U_{wall} = 2.0\ \sigma/\tau$ at temperature $T_{wall} = 1.3\ \epsilon k_B^{-1}$. MD simulations are performed every continuum time step around the lower grid point for 10^6 number of time steps and the temperature jumps and slip velocities are mapped back to the continuum solver.

Figure 5.21 shows the velocity and temperature profiles across the channel. A linear velocity profile is noticed with apparent slip near the lower wall. The slip's magnitude, for the current shear rate, surface orientation, wall-fluid interactions and surface stiffness, is in perfect agreement with previous molecular studies [66]. A parabolic profile for the

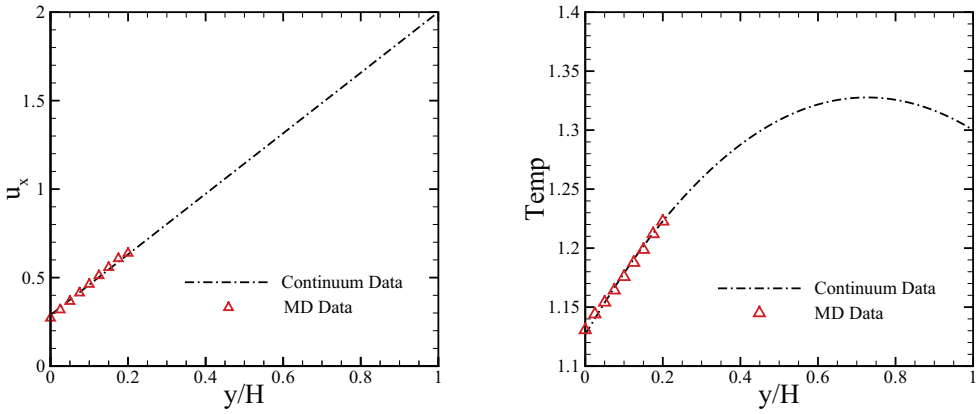

Figure 5.21: Velocity and temperature profiles are calculated by PWC without any numerical optimisation for the Couette heat transfer case

temperature is noticed due to the flow of heat generated due to viscous dissipation [99].

In the Figure 5.22 the velocity and temperature residuals of the continuum solver are shown. It is observed that as the simulation evolves the residuals fluctuate, between 10^{-2} and 10^{-3} for the velocity and around 10^{-3} for the temperature, due to the inherent fluctuations of the molecular information transferred. Small changes in the continuum inputs near certain values produce atomistic outputs that oscillate around a mean value. The fluctuating nature of the molecular results prohibits the continuum solver of achieving acceptable convergence. Therefore, a numerical optimisation procedure will be engaged to minimise the fluctuations of the data transferred from the atomistic solver to the continuum. The goal of this optimisation procedure is twofold, (i) to reduce the fluctuation's amplitude of the atomistic information transferred and (ii) to optimise the efficiency of the entire simulation procedure by minimising the number of molecular simulations performed.

In the current case the linear optimisation procedure, as described in Sec. 3.3.1 and applied in the previous test cases, cannot be applied directly since both the number of inputs and outputs has been increased. The aforementioned procedure can be extended for one additional input however is not straight forward to be generalised for accommodating multidimensional inputs and outputs. Furthermore, even if the number of input parameters is two, like the current case, the implementation's complexity, for the Linear optimisation procedure, increases significantly and the computational benefits are not apparent. For example, in the case studied here after the discretisation of the input variables u_{con}, T_{con} the following four input sets are generated $(u_{in} + m\delta u,\ T_{in} + n\delta T)$, $(u_{in} + (m+1)\,\delta u,\ T_{in} + n\delta T)$, $(u_{in} + m\delta u,\ T_{in} + (n+1)\,\delta T)$, and $(u_{in} + (m+1)\,\delta u,\ T_{in} + (n+1)\,\delta T)$, where $u_{in} + m\delta u < u_{con} < u_{in} + (m+1)\,\delta u$ and $T_{in} + n\delta T < T_{con} < \rho_{in} + (n+1)\,\delta\rho$ and $m, n \in \mathbb{Z}$. Through this procedure if none of the input sets has been previously calculated then 4 MD simulations have to be performed. Additionally, the four input sets lead to combination of 16

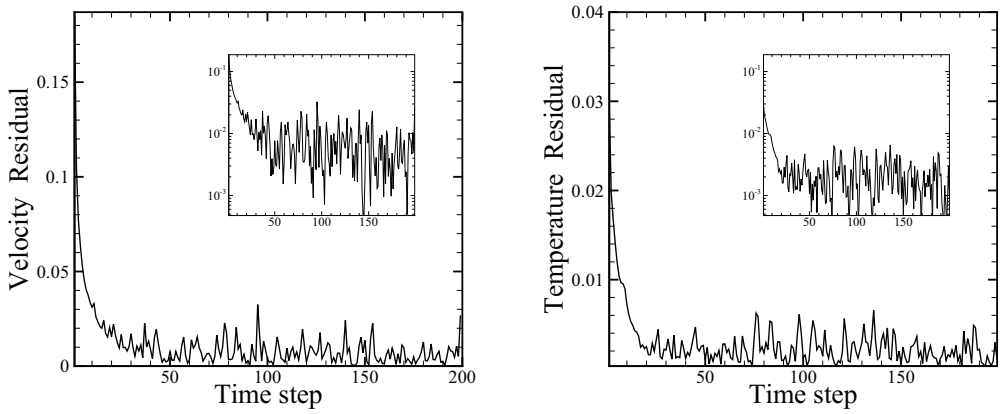

(a) (b)

Figure 5.22: History of the RMS residual for velocity and temperature for PWC without any numerical optimisation for the Couette heat transfer case

input states where either $0, 1, 2, 3$ or 4 atomistic simulations are required. This increases the computational cost and the complexity of the algorithm that searches the library data. Therefore, aiming to overcome these difficulties the Neural Network optimisation procedure is engaged.

5.5.2 Neural Network optimisation

In the neural network optimisation instead of predefining the input sets for the atomistic simulations through the parameters x_{in} and δx (where x is any continuum input), we define a confidence interval around every new input and if any library data are inside this confidence interval then the output is based on the library data otherwise atomistic simulations are performed for the exact continuum input set. For example, in this case a continuum input u_{in} and a parameter δu are defined. A search is performed in the library for data u_{lib} that belong to the interval $u_{in} - \delta u < u_{lib} < u_{in} + \delta u$. If any data fulfill the aforementioned requirements then the atomistic outputs are estimated based on neural networks trained with the library's information. In the event that none of the library data belong in the confidence interval of the continuum input then the following steps are performed: (i) for the exact continuum inputs an atomistic simulation is executed, (ii) the atomistic outputs are stored to the library, (iii) the neural nets are being re-trained and updated to accommodate the new data, and (iv) the neural nets are utilised to provide the microscopic outputs. The molecular outputs are always estimated through neural networks aiming to utilise the networks' smoothing abilities and provide data devoid of large fluctuations that may introduce instabilities in the continuum solver. Figure 5.23 shows the RMS values of the velocity and temperature residuals as have been calculated from PWC simulations (i) with the atomistic data fed back directly to the continuum solver and (ii) the atomistic data fed back through a neural

net.

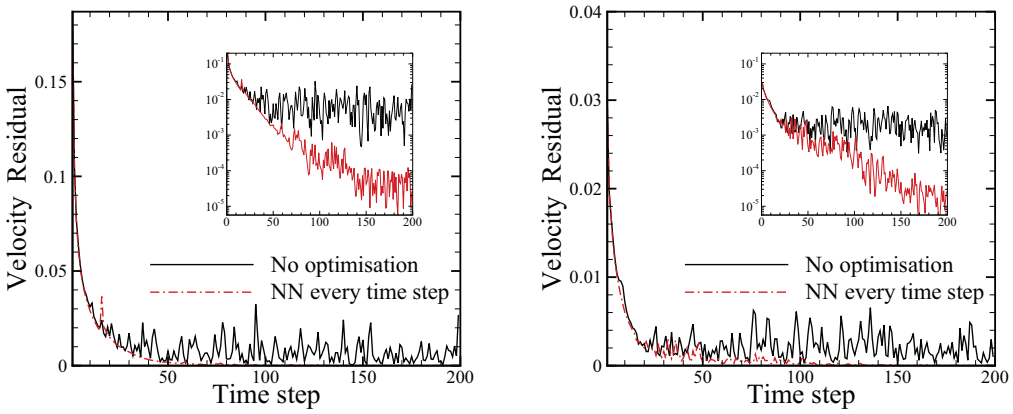

Figure 5.23: History of the RMS residual for velocity, temperature for PWC without any optimisation and for PWC with MD performed at every continuum time step and NN employed to smooth the atomistic outcomes

The velocity residual for the direct coupling case constantly fluctuates and its minimum value is of the order of $10^{-}3$. These fluctuations are originated from the molecular solver represent the fluctuating values of the slip velocity as it is calculated from similar continuum inputs and can be easier realised if a logarithmic scale is employed in the y axis (see inset in Figure 5.23). The application of neural networks compresses the strength of the fluctuations and permit the continuum solver to achieve residuals of the order of 10^{-5}. Specifically, the residual initially decreases smoothly and afterwards oscillations are noticed, primarily due to the continuous changes in the network's parameters every time that a molecular output is generated. The same behaviour is also noticed for the temperature residual.

Figure 5.24 shows slip velocity data transferred to the continuum solver as has been calculated by MD with and without the application of neural networks. This figure shows the smoothing of data achieved with the presence of neural nets, and provides a better insight why neural network optimisation contributes to elimination of any numerical instabilities and artifacts induced to the continuum solver. As the confidence limit increases the neural nets' outputs are based on fewer data and therefore small deviations are observed. Minimising the number of the molecular simulations, although it contributes to the reduction of the computational cost, implies that fewer data will be utilised for estimating the fluctuating average of the atomistic simulations.

Figure 5.25 shows the velocity and temperature residuals compared to those obtained from the neural network optimasation with $\delta u = 5 \cdot 10^{-3}$. In this case the convergence of the simulation is noticeable faster compared to the extreme case where $\delta u \to 0$ and the neural networks have been updated every time step.

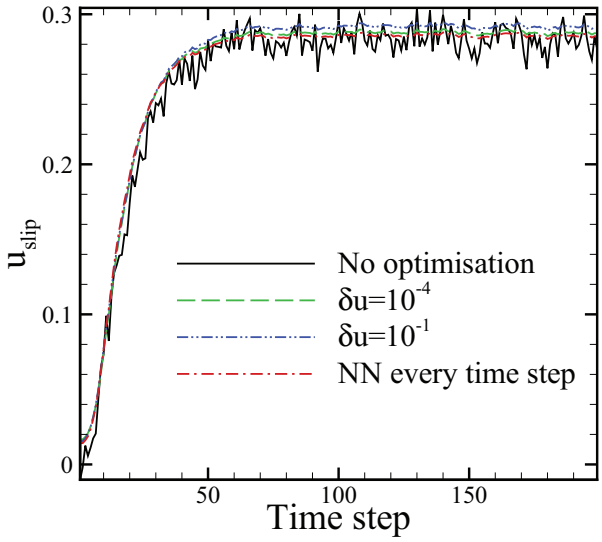

Figure 5.24: Slip velocity data transferred to the continuum solver as calculated by MD with and without the applications of neural networks

Hybrid PWC simulations have been performed for a number of different confidence intervals $(\delta u, \delta T)$ spanning from $\delta u = \delta T = 10^{-4}$ to $\delta u = \delta T = 0.1$. Smaller values of the confidence intervals implies that a larger number of MD simulations will be performed generating larger number of data for the training procedure. Therefore, the neural nets would be able to reduce any uncertainties associated with the oscillating nature of the atomistic outputs. The overall computational cost is dictated by the atomistic simulations and increasing their number unavoidably will add an additional computational burden.

Figure 5.26 shows the number of MD simulations as a factor of $\delta u = \delta T$. As the confidence limit increases the number of atomistic simulations decreases with a non-linear manner. For the example studied here, for $\delta u = \delta T = 10^{-4}$ a total number of 114 MD simulations are performed and for $\delta u = \delta T = 10^{-1}$ the number of molecular simulations is reduced to 8.

Figure 5.27 shows the root mean square deviation of the atomistic outputs compared to the one obtained with $\delta u = 10^{-4}$. The atomistic outcomes produced for different confidence limits are generally in good agreement and primarily for $\delta u \leq 10^{-2}$ the differences are less than 5%.

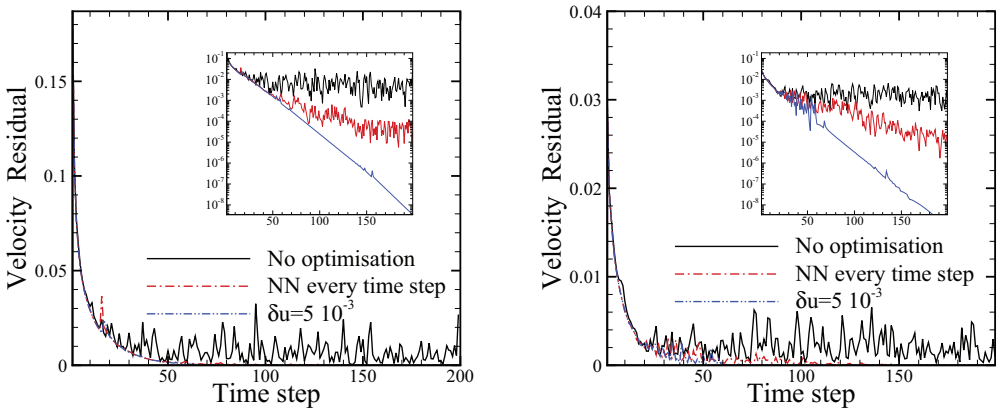

Figure 5.25: History of the RMS residual for velocity, temperature for PWC with NN optimisation procedure

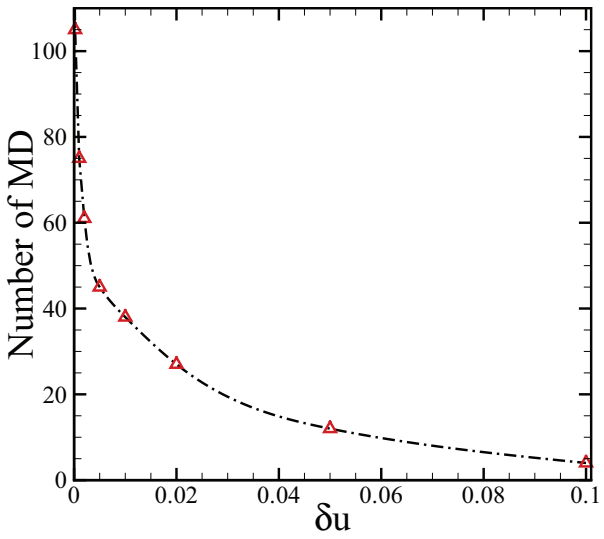

Figure 5.26: Number of MD simulations performed as a factor of the parameter δu

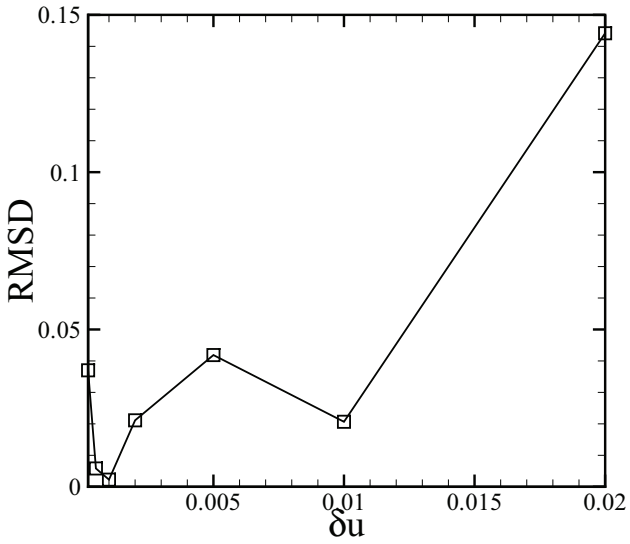

Figure 5.27: Shows the differences in the simulation's outcomes as a factor of δu, with $\delta u = 10^{-4}$ being the point of reference

5.5.3 Neural Network's architectures

In the current example for every case two neural networks have been used with two inputs, one output and two hidden layers. Both neural networks take as inputs the continuum velocity and temperature, the first one calculates the slip velocity and the second one the temperature jump. Potentially, instead of two separate networks we could have engaged one with two inputs and two outputs. However, here the choice of the two separate networks perform better in terms of accuracy and at the same time offers flexibility and minimises the risk of generating numerical artifacts due to inappropriate training of the network. For the optimisation of the networks' architectures the procedure described in Sec. 2.5.3 has been applied. For the training of the networks the 75% of the data produced from the atomistic solver have been used and the remaining 25% have been used for validation purposes.

To illustrate the efficiency benefits (at this point it has to be reminded that computational efficiency was one of the main objectives of the current project) the PWC method, as applied without any optimisation procedure, is compared to the domain decomposition method as implemented by Yen [23] in the slip Couette flow study. Considering the minimum size of the MD domain in both cases to be of order $(10 - 12)\sigma$ and taking into account the overlapping region of at least $(10 - 12)\sigma$ necessary for the convergence of the domain decomposition [23], it is possible to state that the costs associated with the PWC MD simulations are halved in comparison with the domain decomposition. Furthermore, due to the time decoupling of the PWC, the number of MD timesteps performed between one continuum time step is 5 times smaller leading to an overall $10x$ speedup factor. If the

δu	1^{st} Layer	2^{nd} Layer
10^{-4}	1	5
$2 \cdot 10^{-4}$	4	11
$5 \cdot 10^{-4}$	4	3
10^{-3}	5	5
$2 \cdot 10^{-3}$	5	3
$5 \cdot 10^{-3}$	3	6
10^{-2}	12	6
$2 \cdot 10^{-2}$	1	3
$5 \cdot 10^{-2}$	12	9
10^{-1}	3	11

Table 5.3: Optimal network architectures (in the table the number of neuron at each hidden layer are shown) for slip velocity estimation

δu	1^{st} Layer	2^{nd} Layer
10^{-4}	2	2
$2 \cdot 10^{-4}$	1	12
$5 \cdot 10^{-4}$	2	1
10^{-3}	1	10
$2 \cdot 10^{-3}$	6	2
$5 \cdot 10^{-3}$	4	5
10^{-2}	2	9
$2 \cdot 10^{-2}$	4	1
$5 \cdot 10^{-2}$	2	4
10^{-1}	5	10

Table 5.4: Optimal network architectures (in the table the number of neuron at each hidden layer are shown) for temperature jump estimation

NN optimisation procedure is taken into account then the computational cost can be even reduced an extra order of magnitude.

Tables 5.3 and 5.4 show the neural architectures that have been created in hybrid simulations under different values for the confidence intervals δu. Specifically, Table 5.3 summarises the neural networks used for estimating slip velocities and Table 5.4 those used for estimating temperature jumps. In the first column of both tables the various confidence intervals are shown, in the second one the number of neurons at the first hidden layer and in the third one the number of neurons at the second hidden layer. Although the potential maximum number of neurons at each hidden layer is 31, it is noticed that there none of the hidden layers of the neural networks has more than 12 neurons. This fact shows the ability of ANN with fairly simple architectures to model the relationships between the continuum and molecular outputs. The advantages of the ANN will be more apparent in multi-parametric cases, where the molecular outputs depend upon a larger of continuum

inputs.

5.5.4 Conclusions

The neural networks compared to linear optimisation have added an extra flexibility to the development of the framework that facilitates the exchange of information between the continuum and molecular region. Their main advantages are:

- Generic properties: The NN optimisation can be extended to accommodate any number of input and output parameters
- Consistency: As illustrated in the current example there is a small variability in the neural networks outcomes even in cases were very different confidence limits were employed
- Efficiency control: Through the NN optimisation the number of MD simulations can be controlled based on the values of the confidence intervals and can be optimised based on the problem's accuracy and efficiency requirements
- Smoothing properties: The neural networks act as a smoothing operator for reducing the fluctuations in the atomistic outputs.

CHAPTER 6

Conclusions and Future work

Over the last years increased interest has been observed in the scientific community towards multiscale modelling techniques due to their unique potential to simulate accurately and efficiently problems in micro and nanofluid dynamics. Several frameworks have been proposed for modelling flows in multiple scales. These frameworks specify the information that has to be exchanged, and facilitate the communication between the molecular and continuum description. However, their applicability to complex fluid flow scenarios experiences limitations due to the computational complexity of the proposed algorithms and primarily due to the computational cost of the microscale solver, which is still dominant.

The work of this thesis has made contributions towards closing the knowledge gaps in the development of efficient hybrid atomistic/continuum frameworks. Specifically, a new multiscale methodology, named as Point Wise Coupling, that aims to accommodate larger temporal and length scales and minimise the impact of the atomistic solver has been developed. Molecular studies have also been performed, as part of the current research, to provide a better insight regarding nanofluidic phenomena, such as the impact of surface roughness in the slip process. The main conclusions can be summarised as follows:

- An efficient utilisation of neural networks in conjunction with MD simulations has been presented. A neural networks model was implemented for a solid material with a void, subjected to shear. The neural networks predictions were found in very good agreement with the actual simulation results.

  This study (Sec. 4.1) shows that neural networks can be used as an efficient tool to circumvent computer resource issues associated with molecular simulations, as well as to obtain information for different sets of initial and boundary conditions. Research is under way to apply the proposed model to various applications, including design of nanofluidic sensors and dynamic friction at material interfaces

- The effects of rectangular surface roughness with variable height and surface attraction energy on the slip generated, have been investigated using molecular dynamics simulations. The numerical experiments were carried out for various corrugation am-

plitudes and attraction energies. As ϵ_{wf} or A increase, the density layering in the near the wall region is enhanced by higher values or secondary layering phenomena. In addition, the rectangular corrugation provides a mechanism for propagation of the fluid particles layering towards the center of the channel. The higher the corrugation amplitude is the closer to the center of the channel the density fluctuations are transferred. The simulation results indicate a non-linear variation of slip as a factor of roughness amplitude.

- The relationship between the wall stiffness and the slip produced has been investigated. For the first time we show that the slip length variations as a function of surface stiffness can be approximated and well described through a master curve. Quantifying the dependence of L_s on κ provides a mechanism for obtaining a better insight in the slip phenomena and reducing the variability regarding the values of surface stiffness employed in molecular simulations.

- An investigation of different mesoscale approaches for coupling macroscopic and microscopic simulations was presented. Two BCT methods of constraining the molecular domain to the continuum state have been examined, one based on rescaling the atoms' velocities and the other one is based on velocity sampling through a distribution function. Simulations performed with the rescaling BCT method show that it can be successfully applied to both liquid and gas flows. The size of the regions where the velocity constraints are applied has to be selected carefully in order to obtain consistent velocities with the continuum state.

  For the second BCT method, Maxwell-Boltzmann and Chapman-Enskog distribution functions were examined. The former has been used in liquid simulations and the results were found in good agreement with the rescaling BCT method. The size of the constrained domain, the way that the domain is terminated and the sampling frequency may have significant impact on the results when the Maxwell-Boltzmann distribution is used. Inadequate sampling frequency can lead to unrealistic effects, such as trapping of particles in the constrained region, or deviations between the macroscopic and microscopic velocities. The application of the Maxwell-Boltzmann distribution to gas flows leads to discrepancies between the desired and the actual applied velocity. This discrepancy can be corrected by applying the Chapman-Enskog distribution. The results obtained are then consistent with the rescaling-based BCT method and larger MD simulations. The selection of BCT method is not a trivial issue. It depends on the specific simulated problem and a number of other parameters such as the accuracy requirements and the available computational resource.

- The PWC method effectively decouples the timescales and employs smaller domains for the MD simulations, which lead to increased efficiency in comparison with the classic domain decomposition approach. A novelty that PWC possesses is the numerical optimisation procedures employed to handle the vast computational cost introduced by the microscopic simulations. The main idea of the numerical optimisation procedure is to utilise data produced by previous MD simulations and avoid atomistic simulations of nearly identical states.

- PWC under Linear optimisation effectively avoids performing MD simulations for nearly identical continuum states realising an extreme reduction of the method's computational burden. By tuning the interval parameter of the interpolation scheme, for example δu, the number of the performed MD simulations can be regulated to balance between accuracy, stability and efficiency.

  The Linear optimisation although it prohibits the propagation of any instabilities towards the continuum side does not take into account the oscillating nature of the atomistic outputs and provide statistically averaged data. Concurrently, it cannot be directly extended to accommodate multiple inputs and outputs.

- The neural networks compared to linear optimisation have added an extra flexibility to the development of the framework that facilitates the exchange of information between the continuum and molecular region. Their main advantages are:

  - Generic properties: The NN optimisation can be extended to accommodate any number of input and output parameters
  - Consistency: As illustrated in the example at Section 5.5 there is a small variability in the neural networks outcomes even in cases were very different confidence limits were employed
  - Efficiency control: Through the NN optimisation the number of MD simulations can be controlled based on the values of the confidence intervals and can be optimised based on the problem's accuracy and efficiency requirements
  - Smoothing properties: The neural networks act as a smoothing operator for reducing the fluctuations in the atomistic outputs.

The final objective of the hybrid methods is to provide an elegant framework, in terms of efficiency, that enhance the simulation capabilities of the traditional continuum approaches. In the current work a major step forward has be done towards that direction. However, there are still open questions that need to be addressed:

- The mechanism that generates the slip and the factors affecting the amount of the interfacial slip produced are not fully understood. Future work should be carried out to further investigate the contribution of parameters, such as generalised nanoscale roughness, wettability, rate dependency and interaction parameters to the slip behaviour.

- The PWC method has to be applied to more realistic problems, under interaction potentials that can model physical phenomena of interest. The impact of the neural networks in the convergence of the continuum solver has to be further examined.

- Further developments of the optimisation procedures to other coupling frameworks should be considered.

- Further development of the existing boundary condition imposing methods are required. A major challenge is to develop BCT able to accommodate macromolecules that can travel from the macroscopic description to the microscopic and vice versa.
- Other challenges that have to be addressed in the future involve parallelisation of hybrid codes [13].

Bibliography

[1] G. Whitesides. The origins and the future of microfluidics. *Nature*, 442:368–373, 2006.

[2] J. Hong, J. B. Edel, and A. J. deMello. Micro- and nanofluidic systems for high-throughput biological screening. *Drug discovery today*, 14(3-4):134–146, 2009.

[3] P. Abgrall and N. T. Nguyen. Nanofluidic devices and their applications. *An. Chem.*, 80(7):2326–2341, 2008.

[4] Z. Wu and N. Nguyen. Hydrodynamic focusing in microchannels under consideration of diffusive dispersion: Theories and experiments. *Sen. and Actuat. B*, 107(2): 965–974, 2005.

[5] A. E. Kamholz, B. H. Weigl, B. A. Finlayson, and P. Yager. Quantitative analysis of molecular interaction in a microfluidic channel: The t-sensor. *An. Chem.*, 71(23): 5340–5347, 1999.

[6] M. Gad-El-Hak. Gas and liquid transport at the microscale. *Heat Tran. Eng.*, 27(4): 13–29, 2006.

[7] X. Jin, S. Joseph, E. N. Gatimu, P. W. Bohn, and N. R. Aluru. Induced electrokinetic transport in micro-nanofluidic interconnect devices. *Langmuir*, 23(26):13209–13222, 2007.

[8] G. Hu and D. Li. Multiscale phenomena in microfluidics and nanofluidics. *Chem. Eng. Sc.*, 62(13):3443–3454, 2007.

[9] D. Drikakis and M. Kalweit. *First Handbook in Theoretical and Computational Nanotechnology*, chapter Computational Modelling of Flow and Mass Transport Processes in Nanotechnology. American Scientific Publishers, 2006.

[10] S. Yasuda and R. Yamamoto. A model for hybrid simulations of molecular dynamics and computational fluid dynamics. *Physics of Fluids*, 20(11), 2008.

[11] N. Asproulis, M. Benke, M. Lai, E. Shapiro, D. Drikakis, D. Brown, M. Dawson, G. Pollard, P. Ioannou, and V. Poulopoulos. Modelling approaches for micro- and nanoscale diffusion phenomena. In *Green Chemistry and Engineering, International Conference on Process Intensification and Nanotechnology*, pages 175–188, September 2008.

[12] D. Trebotich, G. H. Miller, P. Colella, D. T. Graves, D. F. Martin, and P. O. Schwartz. A tightly coupled particle-fluid model for dna-laden flows in complex microscale geometries. In *Computational Fluid and Solid Mechanics 2005*, pages 1018–1022, 2005.

[13] M. Kalweit and D. Drikakis. Multiscale methods for micro/nano flows and materials. *J. Comput. Theo. Nano Sci.*, 5(9):1923–1938, 2008.

[14] Thomas Werder, Jens Walther, and Petros Koumoutsakos. Hybrid atomistic-continuum method for the simulation of dense fluid flows. *J. Comput. Phys.*, 205: 373–390, 2005.

[15] Rafael Delgado-Buscalioni and Peter Coveney. Hybrid molecular-continuum fluid dynamics. *Phil. Trans. R. Soc. Lond. A*, 362:1639–1654, 2004.

[16] M Kalweit and D Drikakis. Coupling strategies for hybrid molecularcontinuum simulation methods. *Proceedings of the I MECH E Part C Journal of Mechanical Engineering Science*, 222:797–806(10), 2008.

[17] X. Nie, M. O. Robbins, and S. Chen. Resolving singular forces in cavity flow: Multiscale modeling from atomic to millimeter scales. *Phys. Rev. Lett.*, 96(13):1–4, 2006.

[18] Y Wang and G. He. A dynamic coupling model for hybrid atomistic-continuum computations. *Chem. Eng. Sc.*, 62(13):3574–3579, 2007.

[19] R. Delgado-Buscalioni, K. Kremer, and M. Praprotnik. Concurrent triple-scale simulation of molecular liquids. *J. Chem. Phys.*, 128(11), 2008.

[20] D. A. Fedosov and G. E. Karniadakis. Triple-decker: Interfacing atomistic-mesoscopic-continuum flow regimes. *J. Comput. Phys.*, 228(4):1157–1171, 2009.

[21] T. E. Schwartzentruber, L. C. Scalabrin, and I. D. Boyd. A modular particle-continuum numerical method for hypersonic non-equilibrium gas flows. *J. Comput. Phys.*, 225(1):1159–1174, 2007.

[22] Z. Li and H. Zhang. Gas-kinetic numerical studies of three-dimensional complex flows on spacecraft re-entry. *J. Comput. Phys.*, 228(4):1116–1138, 2009.

[23] T. H. Yen, C. Y. Soong, and P. Y. Tzeng. Hybrid molecular dynamics-continuum simulation for nano/mesoscale channel flows. *Microfluidics and Nanofluidics*, 3(6): 665–675, 2007.

[24] H. S. Wijesinghe, R. D. Hornung, A. L. Garcia, and N. G. Hadjiconstantinou. Three-dimensional hybrid continuum-atomistic simulations for multiscale hydrodynamics. *J. Fl. Eng.*, 126(5):768–777, 2004.

[25] W. Ren and E. Weinan. Heterogeneous multiscale method for the modeling of complex fluids and micro-fluidics. *J. Comput. Phys.*, 204(1):1–26, 2005.

[26] C. J. Garcia-Cervera, W. Ren, J. Lu, and E. Weinan. Sequential multiscale modeling using sparse representation. *Comm. Comp. Ph.*, 4(5):1025–1033, 2008.

[27] E. Weinan, B. Engquist, X. Li, W. Ren, and E. Vanden-Eijnden. Heterogeneous multiscale methods: A review. *Comm. Comp. Ph.*, 2(3):367–450, 2007.

[28] W. Ren. Analytical and numerical study of coupled atomistic-continuum methods for fluids. *J. Comput. Phys.*, 227(2):1353–1371, 2007.

[29] W. Ren. Seamless multiscale modeling of complex fluids using fiber bundle dynamics. *Communications in Mathematical Sciences*, 5(4):1027–1037, 2007.

[30] N. Asproulis, M. Kalweit, and D. Drikakis. A hybrid molecular continuum method using point wise coupling. In B. Topping and M. Papadrakakis, editors, *Sixth International Conference on Engineering Computational Technology*. Civil-Comp Press, September 2008.

[31] N. Asproulis, E. Shapiro, M. Kalweit, and D. Drikakis. Multiscale modelling for flows and materials. In *Cranfield Multi-Strand Conference*. Cranfield Press, May 2008.

[32] M. Kalweit, N. Asproulis, and D. Drikakis. Nanofluidic applications of hybrid molecular continuum methods. In *Green Chemistry and Engineering, International Conference on Process Intensification and Nanotechnology*, pages 189–199, September 2008.

[33] S. Prakash, A. Piruska, E. N. Gatimu, P. W. Bohn, J. V. Sweedler, and M. A. Shannon. Nanofluidics: Systems and applications. *IEEE Sen. J.*, 8(5):441–450, 2008.

[34] V. Linder. Microfluidics at the crossroad with point-of-care diagnostics. *Analyst*, 132(12):1186–1192, 2007.

[35] N. G. Hadjiconstantinou. The limits of navier-stokes theory and kinetic extensions for describing small-scale gaseous hydrodynamics. *Physics of Fluids*, 18(11), 2006.

[36] N. G. Hadjiconstantinou. Validation of a second-order slip model for dilute gas flows. *Micr. Therm. Eng.*, 9(2):137–153, 2005.

[37] D. Drikakis and W. Rider. *High-Resolution Methods for Incompressible and Low-Speed Flows*. Springer, 2004.

[38] D. Kwak and C. Kiris. CFD for incompressible flows at NASA Ames. *Computers and Fluids*, 38(3):504–510, 2009.

[39] G. Karniadakis, A. Beskok, and N. Aluru. *Microflows and Nanoflows: Fundamentals and Simulation*. Springer, New York, 2005.

[40] E. F. Toro. *Riemann Solvers and Numerical Methods for Fluid Dynamics*. Springer-Verlag, 1997.

[41] C. Siegel. Review of computational heat and mass transfer modeling in polymer-electrolyte-membrane (pem) fuel cells. *Energy*, 33(9):1331–1352, 2008.

[42] N.I. Kolev. *Multiphase Flow Dynamics: v. 1: Fundamentals, 3rd ed.* Springer-Verlag, 2007.

[43] N.I. Kolev. *Multiphase Flow Dynamics: v. 2: Thermal and Mechanical Interactions, 3rd ed.* Springer-Verlag, 2007.

[44] R.G. Owens and T.N. Phillips. *Computational Rheology*. Imperial College Press, 2002.

[45] S.G. Kandlikar, S. Garimella, D. Li, S. Colin, and M. R. King. *Heat Transfer and Fluid Flow in Minichannels and Microchannels*. Elsevier, 2006.

[46] E. Y. Gatapova and O. A. Kabov. Shear-driven flows of locally heated liquid films. *Int. J. Heat Mass Transfer*, 51:4797–4810, 2008.

[47] M. W. Weber and R. Shandas. Computational fluid dynamics analysis of microbubble formation in microfluidic flow-focusing devices. *Microfluidics and Nanofluidics*, 3(2):195–206, 2007.

[48] C-C Chang and R-J Yang. Computational analysis of electrokinetically driven flow mixing in microchannels with patterned blocks. *J. Micromech. Microeng.*, 14:550, 2004.

[49] K.-D. Huang and R.-J. Yang. Formation of ionic depletion/enrichment zones in a hybrid micro-/nano-channel. *Microfluidics and Nanofluidics*, 5(5):631–638, 2008.

[50] M. Gad el Hak, editor. *MEMS Handbook*. CRC Press, 2001.

[51] T.G. Elizarova, I.A. Graur, J.C. Lengrand, and A. Chpoun. Rarefied gas flow simulation based on quasi gas dynamic equations. *AIAA Journal*, 33(12):2316–2324, 1995.

[52] S. V. Patankar. *Numerical Heat Transfer and Fluid Flow*. Hemisphere, 1980.

[53] J. B. Bell and D. L. Marcus. A second-order projection method for variable-density flows. *J. Comput. Phys.*, 101:334, 1992.

[54] A. S. Almgren, J. B. Bell, and W. G. Szymczak. A numerical method for the incompressible Navier-Stokes equations based on an approximate projection. *SIAM J. Sci. Comput*, 17(2):358, 1996.

[55] A. S. Almgren, J. B. Bell, P. Colella, L. H. Howell, and M. L. Welcome. A conservative projection method for the variable-density incompressible navier-stokes equations. *J. Comput. Phys.*, 142:1, 1998.

[56] W. J. Rider, D. B. Kothe, E. G. Puckett, and I. D. Aleinov. *Barriers and Challenges in Computational Fluid Dynamics*, chapter Accurate and Robust Methods For Variable Density Incompressible Flows With Discontinuities, pages 213–330. Kluwer Academic Publishers, Boston, MA, 1998.

[57] T. Utnes. A segregated implicit pressure projection method for incompressible flows. *J. Comput. Phys.*, 227(4):2198–2211, 2008.

[58] Y. Fraigneau, J.L. Guermond, and L. Quartapelle. Approximation of variable density incompressible flows by means of finite elements and finite volumes. *Com. Num. Meth. Eng.*, 17:893, 2001.

[59] A.J. Chorin. A numerical method for solving incompressible viscous flow problems. *J. Comput. Phys.*, 2:12–26, 1967.

[60] D. Choi and C.L. Merkle. Application of time-iterative schemes to incompressible flow. *AIAA Journal*, 23(10):1518–1524, 1985.

[61] E. Shapiro and D. Drikakis. Artificial compressibility, characteristics-based schemes for variable density, incompressible, multi-species flows. Part I. derivation of different formulations and constant density limit. *J. Comput. Phys.*, 210(2):584–607, 2005.

[62] E. Shapiro and D. Drikakis. Artificial compressibility, characteristics-based schemes for variable density, incompressible, multi-species flows. Part II. multigrid implementation and numerical tests. *J. Comput. Phys.*, 210:608–631, 2005.

[63] M. Benke, E. Shapiro, and D. Drikakis. An efficient multi-scale modelling approach for ssdna motion in fluid flow. *J. Bio. Eng.*, 5(4):299–307, 2008.

[64] E. Shapiro, D. Drikakis, J. Gargiuli, and P. Vadgama. Interface capturing in dual-flow microfluidics. *J. Comput. Theo. Nano Sci.*, 4:802–806, 2007.

[65] A. Niavarani and N. V. Priezjev. Slip boundary conditions for shear flow of polymer melts past atomically flat surfaces. *Phys. Rev. E*, 77(4), 2008.

[66] N. V. Priezjev. Effect of surface roughness on rate-dependent slip in simple fluids. *J. Chem. Phys.*, 127(14):144708, 2007.

[67] F. D. Sofos, T. E. Karakasidis, and A. Liakopoulos. Effects of wall roughness on flow in nanochannels. *Phys. Rev. E*, 79(2), 2009.

[68] A. S. Ziarani and A. A. Mohamad. Molecular dynamics study of velocity slip in microchannels. In *Proceedings of the 17th IASTED international conference on Modelling and simulation*, pages 585–590. ACTA Press, 2006.

[69] C. Y. Soong, T. H. Yen, and P. Y. Tzeng. Molecular dynamics simulation of nanochannel flows with effects of wall lattice-fluid interactions. *Phys. Rev. E*, 76 (3):036303, 2007.

[70] B. Y. Cao. Non-maxwell slippage induced by surface roughness for microscale gas flow: A molecular dynamics simulation. *Mol. Phys.*, 105(10):1403–1410, 2007.

[71] T. M. Galea and P. Attard. Molecular dynamics study of the effect of atomic roughness on the slip length at the fluid-solid boundary during shear flow. *Langmuir*, 20 (8):3477–3482, 2004.

[72] F. Chen, W. Ge, L. Wang, and J. Li. Numerical study on gas-liquid nano-flows with pseudo-particle modeling and soft-particle molecular dynamics simulation. *Microfluidics and Nanofluidics*, 5(5):639–653, 2008.

[73] J. Lechuga, D. Drikakis, and S. Pal. Molecular dynamics study of the interaction of a shock wave with a biological membrane. *Int. J. Num. Meth. Fl.*, 57(5):677–692, 2008.

[74] G. Ayton, S. Izvekov, W.G. Noid, and G. A. Voth. Chapter 7 multiscale simulation of membranes and membrane proteins: Connecting molecular interactions to mesoscopic behavior. In S. E. Feller, editor, *Computational Modeling of Membrane Bilayers*, volume 60 of *Current Topics in Membranes*, pages 181 – 225. Academic Press, 2008.

[75] S. Melchionna, M. G. Fyta, E. Kaxiras, and S. Succi. Exploring dna translocation through a nanopore via a multiscale lattice-boltzmann molecular-dynamics methodology. *Int. J. Mod. Phys. C*, 18(4):685–692, 2007.

[76] B. C. Stephenson and K. J. Beers. Determination of the interfacial characteristics of a series of bolaamphiphilic poly(fluorooxetane) surfactants through molecular dynamics simulation. *J. Phys. Chem. B*, 110(39):19393–19405, 2006.

[77] R. B. Schoch, J. Han, and P. Renaud. Transport phenomena in nanofluidics. *Rev. Mod. Phys.*, 80(3):839–883, 2008.

[78] C. S. Kim. Nonequilibrium molecular dynamics approach for nanoelectromechanical systems: Nanofluidics and its applications. *J. Fl. Eng.*, 129(9):1140–1146, 2007.

[79] J. M. Di Leo and J. Maranon. Water flow through nanopore. *Int. Quant. Chem.*, 108 (10):1623–1628, 2008.

[80] A. Noy, H. G. Park, F. Fornasiero, J. K. Holt, C. P. Grigoropoulos, and O. Bakajin. Nanofluidics in carbon nanotubes. *Nano Today*, 2(6):22–29, 2007.

[81] M. Muller, C. Pastorino, and J. Servantie. Flow, slippage and a hydrodynamic boundary condition of polymers at surfaces. *J. Phys. Cond.*, 20(49), 2008.

[82] C. D. F. Honig and W. A. Ducker. Thin film lubrication for large colloidal particles: Experimental test of the no-slip boundary condition. *J. Phys. Chem. C*, 111(44): 16300–16312, 2007.

[83] R. Buzio, C. Boragno, and U. Valbusa. Friction laws for lubricated nanocontacts. *J. Chem. Phys.*, 125(9), 2006.

[84] Y. Zhang. Contact-fluid interfacial slippage in hydrodynamic lubricated contacts. *J. Mol. Liq.*, 128(1-3):99–104, 2006.

[85] M. T. Matthews and J. M. Hill. Lubrication analysis of the viscous micro/nano pump with slip. *Microfluidics and Nanofluidics*, 4(5):439–449, 2008.

[86] Q. Guo, P. S. Chung, H. Chen, and M. S. Jhon. Molecular rheology of perfluoropolyether lubricant via nonequilibrium molecular dynamics simulation. *J. Appl. Ph.*, 99(8), 2006.

[87] F. Ercolessi. A molecular dynamics primer, 1997. URL `http://www.fisica.uniud.it/~ercolessi/md/md/`. Available at http://www.fisica.uniud.it/ ercolessi/md/md/. Accessed on 14 August 2007.

[88] N. Asproulis and D. Drikakis. Nanoscale materials modelling using neural networks. *J. Comput. Theo. Nano Sci.*, 6(3):514–518, 2009.

[89] L. Verlet. Computer 'experiments' on classical fluids. I. Thermodynamical properties of Lennard-Jones molecules. *Phys. Rev.*, 159:98–103, 1967.

[90] M. P. Allen and D. J. Tildesley. *Computer simulation of liquids*. Oxford University Press, Oxford, 1987.

[91] G. Sutmann. *Quantum Simulations of complex many-body systems: From theory to algorithms, lecture notes*, volume 10, chapter Classical molecular dynamics, pages 211–254. John von Neumann Institute for Computing, Juelich, NIC Series, 2002.

[92] M. Kalweit. *Molecular Modelling for Meso- and Nanoscale Dynamics*. PhD thesis, Dept. Aerosp. Scienc., University of Cranfield, 2008.

[93] N. G. Hadjiconstantinou. Discussion of recent developments in hybrid atomistic-continuum methods for multiscale hydrodynamics. *Bulletin of the Polish Academy of Sciences: Technical Sciences*, 53(4):335–342, 2005.

[94] E. G. Flekkoy, G. Wagner, and J. Feder. Hybrid model for combined particle and continuum dynamics. *Europhys. Lett.*, 52(3):271–276, 2000.

[95] R. Delgado-Buscalioni and P. V. Coveney. Continuum-particle hybrid coupling for mass, momentum, and energy transfers in unsteady fluid flow. *Phys. Rev. E*, 67(4 Pt 2):046704, Apr 2003.

[96] R. Delgado-Buscalioni and P.V. Coveney. Usher: An algorithm for particle insertion in dense fluids. *J. Chem. Phys.*, 119:978–987, 2003.

[97] G. D. Fabritiis, R. Delgado-Buscalioni, and P. V. Coveney. Energy controlled insertion of polar molecules in dense fluids. *J. Chem. Phys.*, 121(24):12139–12142, 2004.

[98] J. Liu, S. Chen, X. Nie, and M. O. Robbins. A continuum-atomistic multi-timescale algorithm for micro/nano flows. *Comm. Comp. Ph.*, 4(5):1279–1291, 2008.

[99] J. Liu, S. Chen, X. Nie, and M. O. Robbins. A continuum-atomistic simulation of heat transfer in micro- and nano-flows. *J. Comput. Phys.*, 227(1):279–291, 2007.

[100] E. M. Kotsalis, J. H. Walther, and P. Koumoutsakos. Control of density fluctuations in atomistic-continuum simulations of dense liquids. *Phys. Rev. E*, 76(1), 2007.

[101] X. B. Nie, S. Y. Chen, W. N. E, and M. O. Robbins. A continuum and molecular dynamics hybrid method for micro- and nano-fluid flow. *J. Fluid Mech.*, (500):55–64, 2004.

[102] S.T. O'connell and P.A. Thompson. Molecular dynamics-continuum hybrid computations: A tool for studying complex fluid flows. *Phys. Rev. E*, 52(6):R5792–R5795, 1995.

[103] W. S. McCulloch and W. Pitts. A logical calculus of the ideas immanent in nervous activity. *Bulletin of Mathematical Biology*, 52(1-2):99–115, 1990.

[104] Ben Krose and Patrik van de Smagt. *An Introduction to Artificial Neural Networks*. The University of Amsterdam, Amsterdam, 1996.

[105] Laurene V. Fausett. *Fundamentals of Neural Networks*. Prentice Hall, New York, 1994.

[106] James Freeman and David Skapura. *Neural Networks: Algorithm, Applications and Programming techniques*. Addison-Wesley, California, 1991.

[107] D.E. Goldberg. *Genetic Algorithms in Search, Optimization and Machine learing*. Addison-Wesley, New York, 1989.

[108] John H. Holland. *Adaptation in natural and artificial systems*. MIT Press, Cambridge, MA, USA, 1975.

[109] P. G. Benardos and G. Vosniakos. Optimizing feedforward artificial neural network architecture. *Engineering Applications of Artificial Intelligence*, 20(3):365–382, 2007.

[110] J. F. C. Khaw, B. S. Lim, and L. E. N. Lim. Optimal design of neural networks using the taguchi method. *Neurocomputing*, 7(3):225–245, 1995.

[111] H. R. Maier and G. C. Dandy. The effect of internal parameters and geometry on the performance of back-propagation neural networks: An empirical study. *Environmental Modelling and Software*, 13(2):193–209, 1998.

[112] J. Leski and E. Czogala. A new artificial neural network based fuzzy inference system with moving consequents in if-then rules and selected applications. *Fuzzy Sets and Systems*, 108(3):289–297, 1999.

[113] T. F. Rathbun, S. K. Rogers, M. P. DeSimio, and M. E. Oxley. Mlp iterative construction algorithm. *Neurocomputing*, 17(3-4):195–216, 1997.

[114] L. Ma and K. Khorasani. A new strategy for adaptively constructing multilayer feedforward neural networks. *Neurocomputing*, 51:361–385, 2003.

[115] G. Bebis, M. Georgiopoulos, and T. Kasparis. Coupling weight elimination with genetic algorithms to reduce network size and preserve generalization. *Neurocomputing*, 17(3-4):167–194, 1997.

[116] P. A. Castillo, J. J. Merelo, A. Prieto, V. Rivas, and G. Romero. G-prop: Global optimization of multilayer perceptrons using gas. *Neurocomputing*, 35:149–163, 2000.

[117] X. Yao and Y. Liu. A new evolutionary system for evolving artificial neural networks. *IEEE Transactions on Neural Networks*, 8(3):694–713, 1997.

[118] R. Delgado-Buscalioni and P.V. Coveney. Continuum-particle hybrid coupling for mass, momentum and energy transfers. *Phys. Rev. E*, 67:046704, 2003.

[119] G. De Fabritiis, R. Delgado-Buscalioni, and P. V. Coveney. Modelling the mesoscale with molecular specificity. *Phys. Rev. Lett.*, 97:134501, 2006.

[120] N. G. Hadjiconstantinou. Combining atomistic and continuum simulations of contact-line motion. *Phys. Rev. E*, 59:2475, 1999.

[121] N. G. Hadjiconstantinou and A. T. Patera. Heterogeneous atomistic-continuum representations for dense fluid systems. *Int. J. Mod. Phys. C*, 8(4):967–976, 1997.

[122] A. L. Garcia and B. J. Alder. Generation of the chapman-enskog distribution. *J. Comput. Phys.*, 140(1):66–70, 1998.

[123] T. E. Schwartzentruber, L. C. Scalabrin, and I. D. Boyd. Hybrid particle-continuum simulations of hypersonic flow over a hollow-cylinder-flare geometry. *AIAA Journal*, 46(8), 2008.

[124] T. E. Schwartzentruber, L. C. Scalabrin, and I. D. Boyd. Hybrid particle-continuum simulations of nonequilibrium hypersonic blunt-body flowfields. *J. Therm. and Heat Tran.*, 22(1):29–37, 2008.

[125] H. S. Wijesinghe and N. G. Hadjiconstantinou. A hybrid atomistic-continuum formulation for unsteady, viscous, incompressible flows. *CMES*, 5(6):515–526, 2004.

[126] N.R. Bimalendu. *Fundamentals of Classical and Statistical Thermodynamics*. John Wiley, West Sussex, England, 2002.

[127] B. D. Todd and P. J. Daivis. Homogeneous non-equilibrium molecular dynamics simulations of viscous flow: Techniques and applications. *Mol. Simulat.*, 33(3): 189–229, 2007.

[128] W. L. Cavalcanti, X. Chen, and F. Muller-Plathe. Shear viscosity calculations through a reverse nonequilibrium method. *Ph. Status Solidi A*, 204(4):935–939, 2007.

[129] M. Kelkar, J. Rafferty, E. Maginn, and J. Siepmann. Prediction of viscosities and vapor-liquid equilibria for five polyhydric alcohols by molecular simulation. *Fl. Phas. Eq.*, 260(2):218 – 231, 2007.

[130] F. Muller-Plathe. Reversing the perturbation in nonequilibrium molecular dynamics: An easy way to calculate the shear viscosity of fluids. *Phys. Rev. E*, 59(5 B):4894–4898, 1999.

[131] S. Plimpton. Fast parallel algorithms for short-range molecular dynamics. *J. Comput. Phys.*, 117:1–19, 1995.

[132] S. S. Mao and X. Chen. Selected nanotechnologies for renewable energy applications. *Int. J. En. Reas.*, 31(6-7):619–636, 2007.

[133] D. A. R. S. Latino, F. F. M. Freitas, J. Aires-De-Sousa, and F. M. S. S. Fernandes. Neural networks to approach potential energy surfaces: Application to a molecular dynamics simulation. *Int. J. Quant. Chem.*, 107(11):2120–2132, 2007.

[134] I. A. Basheer and M. Hajmeer. Artificial neural networks: Fundamentals, computing, design, and application. *J. Microb. Meth.*, 43(1):3–31, 2000.

[135] M. Benedict and J. F. Maguire. Molecular dynamics simulation of nanomaterials using an artificial neural net. *Phys. Rev. B*, 70(17):1–8, 2004.

[136] B. K. Bose. Neural network applications in power electronics and motor drives - an introduction and perspective. *IEEE Tran. Industr. Electr.*, 54(1):14–33, 2007.

[137] T. V. Santosh, G. Vinod, R. K. Saraf, A. K. Ghosh, and H. S. Kushwaha. Application of artificial neural networks to nuclear power plant transient diagnosis. *Rel. En. Syst. Saf.*, 92(10):1468–1472, 2007.

[138] H. R. Maier and G. C. Dandy. Neural networks for the prediction and forecasting of water resources variables: A review of modelling issues and applications. *Env. Model. Soft.*, 15(1):101–124, 2000.

[139] L. O. Chua and L. Yang. Cellular neural networks: Applications. *IEEE Tran. Cir. Syst.*, 35(10):1273–1290, 1988.

[140] W. G. Baxt. Application of artificial neural networks to clinical medicine. *Lancet*, 346(8983):1135–1138, 1995.

[141] G. Schneider and P. Wrede. Artificial neural networks for computer-based molecular design. *Progr. Bioph. Mol. Biol.*, 70(3):175–222, 1998.

[142] L. Terfloth and J. Gasteiger. Neural networks and genetic algorithms in drug design. *Drug Discovery Today*, 6(SUPPL.2):S102–S108, 2001.

[143] E. Buyukbingol, A. Sisman, M. Akyildiz, F. N. Alparslan, and A. Adejare. Adaptive neuro-fuzzy inference system (anfis): A new approach to predictive modeling in qsar applications: A study of neuro-fuzzy modeling of pcp-based nmda receptor antagonists. *Bioorg. Med. Chem.*, 15(12):4265–4282, 2007.

[144] I. G. Kevrekidis, C. W. Gear, and G. Hummer. Equation-free: The computer-aided analysis of complex multiscale systems. *AIChE J.*, 50(7):1346–1355, 2004.

[145] C. Kunert and J. Harting. Roughness induced boundary slip in microchannel flows. *Phys. Rev. Lett.*, 99(17):176001, 2007.

[146] C. Choi, K. Westin, and K. Breuer. Apparent slip flows in hydrophilic and hydrophobic microchannels. *Physics of Fluids*, 15(10):2897–2902, 2003.

[147] D. Byun, J. Kim, H. S. Ko, and H. C. Park. Direct measurement of slip flows in superhydrophobic microchannels with transverse grooves. *Physics of Fluids*, 20 (11), 2008.

[148] N. V. Priezjev, A. A. Darhuber, and S. M. Troian. Slip behavior in liquid films on surfaces of patterned wettability: Comparison between continuum and molecular dynamics simulations. *Phys. Rev. E*, 71(4), 2005.

[149] S. C. Yang. Effects of surface roughness and interface wettability on nanoscale flow in a nanochannel. *Microfluidics and Nanofluidics*, 2(6):501–511, 2006.

[150] D.C. Rapaport. *The Art of Molecular Dynamics*. Cambridge University Press, Cambridge, 1995.

[151] P. Deuflhard and J. Hermans. *Computational Molecular Dynamics: Methods, Challenges, Ideas*. Springer Verlag, Berlin Heidelberg, 1999.

[152] N. V. Priezjev and S. M. Troian. Influence of periodic wall roughness on the slip behaviour at liquid/ solid interfaces: Molecular-scale simulations versus continuum predictions. *J. Fluid Mech.*, 554:25–46, 2006.

[153] S. T. O'Connel and P. A. Thompson. Origin of stick-slip motion in boundary lubrication. *Science*, 250:792–794, 1990.

[154] P. A. Thompson and S. M. Troian. A general boundary condition for liquid flow at solid surfaces. *Nature*, 389(6649):360–362, 1997.

[155] C. Cottin-Bizonne, J. Barrat, L. Bocquet, and E. Charlaix. Low-friction flows of liquid at nanopatterned interfaces. *Nature Mater.*, 2(4):237–240, 2003.

[156] Elmar Bonaccurso, Hans-Jürgen Butt, and Vincent S. J. Craig. Surface roughness and hydrodynamic boundary slip of a newtonian fluid in a completely wetting system. *Phys. Rev. Lett.*, 90(14):144501, 2003.

[157] Y. Zhu and S. Granick. Limits of the hydrodynamic no-slip boundary condition. *Phys. Rev. Lett.*, 88(10):1061021, 2002.

[158] J. L. Barrat and J. P. Hansen. *Basic concepts for simple and complex liquids*. Oxford University Press, Oxford, 2003.

[159] C. Y. Soong, S. H. Wang, and P. Y. Tzeng. Molecular dynamics simulation of rotating fluids in a cylindrical container. *Physics of Fluids*, 16(8):2814–2827, 2004.

[160] D. C. Tretheway and C. D. Meinhart. Apparent fluid slip at hydrophobic microchannel walls. *Physics of Fluids*, 14(3):L9–L12, 2002.

[161] M. Sbragaglia, R. Benzi, L. Biferale, S. Succi, and F. Toschi. Surface roughness-hydrophobicity coupling in microchannel and nanochannel flows. *Phys. Rev. Lett.*, 97(20):204503, 2006.

[162] J. Barrat and L. Bocquet. Large slip effect at a nonwetting fluid-solid interface. *Phys. Rev. Lett.*, 82(23):4671–4674, 1999.

[163] C. Cottin-Bizonne, C. Barentin, E Charlaix, L. Bocquet, and J. Barrat. Dynamics of simple liquids at heterogeneous surfaces: Molecular-dynamics simulations and hydrodynamic description. *Eur. Phys. J. C*, 15(4):427–438, 2004.

[164] Y. Zhu and S. Granick. Rate-dependent slip of newtonian liquid at smooth surfaces. *Phys. Rev. Lett.*, 87(9):961051, 2001.

[165] K. Binder, J. Horbach, W. Kob, P. Wolfgang, and V. Fathollah. Molecular dynamics simulations. *J. Phys. Cond.*, 16(5):S429–S453, 2004.

[166] Gary S. Grest and Kurt Kremer. Molecular dynamics simulation for polymers in the presence of a heat bath. *Phys. Rev. A*, 33(5):3628–3631, 1986.

[167] A. Jabbarzadeh, J. D. Atkinson, and R. I. Tanner. Wall slip in the molecular dynamics simulation of thin films of hexadecane. *J. Chem. Phys.*, 110(5):2612–2620, 1999.

[168] M. Cieplak, J. Koplik, and J. R. Banavar. Boundary conditions at a fluid-solid interface. *Phys. Rev. Lett.*, 86(5):803–806, 2001.

[169] K.E. Petersen. Dynamic micromechanics on silicon: Techniques and devices. *IEEE Tran. Elec. Dev.*, 25(10):1241–1250, 1978.

[170] B. H. Kim, A. Beskok, and T. Cagin. Thermal interactions in nanoscale fluid flow: Molecular dynamics simulations with solid-liquid interfaces. *Microfluidics and Nanofluidics*, 5(4):551–559, 2008.

[171] J. Koplik, J. R. Banavar, and J. F. Willemsen. Molecular dynamics of fluid flow at solid surfaces. *Physics of Fluids*, 1(5):781–794, 1989.

[172] B. Cao, M. Chen, and Z. Guo. Temperature dependence of the tangential momentum accommodation coefficient for gases. *Appl. Phys. Let.*, 86(9):1–3, 2005.

[173] B. Cao, M. Chen, and Z. Guo. Effect of surface roughness on gas flow in microchannels by molecular dynamics simulation. *In. J. En. Sc.*, 44(13-14):927–937, 2006.

[174] B. Cao. Non-maxwell slippage induced by surface roughness for microscale gas flow: A molecular dynamics simulation. *Mol. Phys.*, 105(10):1403–1410, 2007.

[175] M. Cieplak, J. Koplik, and J. R. Bavanar. Molecular dynamics of flows in the knudsen regime. *Physica A*, 287(1-2):153–160, 2000.

[176] G. W. Finger, J. Kapat, and A. Bhattacharya. Analysis of tangential momentum accommodation coefficient using molecular dynamics simulation. In *44th AIAA Aerospace Sciences Meeting and Exhibit, Reno, Nevada*, volume 22, pages 17136–17159, January 2006.

[177] G. W. Finger, J. S. Kapat, and A. Bhattacharya. Molecular dynamics simulation of adsorbent layer effect on tangential momentum accommodation coefficient. *J. Fl. Eng.*, 129(1):31–39, 2007.

[178] L. O'Hare, T. J. Scanlon, D. R. Emerson, and J. M. Reese. Evaluating constitutive scaling models for application to compressible microflows. *Int. J. Heat Mass Transfer*, 51(5-6):1281–1292, 2008.

[179] A. Martini, A. Roxin, R. Q. Snurr, Q. Wang, and S. Lichter. Molecular mechanisms of liquid slip. *J. Fluid Mech.*, 600:257–269, 2008.

[180] A. Tenenbaum. Local equilibrium in stationary states by molecular dynamics. *Phys. Rev. A*, 28(5):3132–3133, 1983.

[181] R. Tehver, F. Toigo, J. Koplik, and J. R. Banavar. Thermal walls in computer simulations. *Phys. Rev. E*, 57(1), 1998.

[182] D. K. Bhattacharya and G. C. Lie. Nonequilibrium gas flow in the transition regime: A molecular-dynamics study. *Phys. Rev. A*, 43(2):761–767, 1991.

[183] J. L. Xu and Z. Q. Zhou. Molecular dynamics simulation of liquid argon flow at platinum surfaces. *Heat and Mass Tran.*, 40(11):859–869, 2004.

[184] B. Z. Dlugogorski, M. Grmela, and P. J. Carreau. Viscometric functions for fene and generalized lennard-jones dumbbell liquids in couette flow: Molecular dynamics study. *Journal of Non-Newtonian Fluid Mechanics*, 48(3):303–335, 1993.

[185] L. E. Wedgewood and R. B. Bird. From molecular models to the solution of flow problems. *Industrial and Engineering Chemistry Research*, 27(7):1313–1320, 1988.

[186] M. Kroger and S. Hess. Rheological evidence for a dynamical crossover in polymer melts via nonequilibrium molecular dynamics. *Phys. Rev. Lett.*, 85(5):1128–1131, 2000.

[187] M. Kroger. *Models for polymeric and anisotropic liquids*. Springer-Verlag, New York, 2005.

[188] N. V. Priezjev. Rate-dependent slip boundary conditions for simple fluids. *Physical Review E - Statistical, Nonlinear, and Soft Matter Physics*, 75(5), 2007.

[189] M. Gad-El-Hak. Liquids: The holy grail of microfluidic modeling. *Physics of Fluids*, 17:100612, 2005.